

POLARIZATIONS AND ANGULAR DISTRIBUTIONS IN THE
ELASTIC SCATTERING OF PIONS AND PROTONS FROM
POLARIZED PROTONS AT FERMILAB ENERGIES

A Dissertation
Presented to the Faculty of the Graduate School
of
Yale University
in Candidacy for the Degree of
Doctor of Philosophy

by
James H. Snyder

May, 1978

ABSTRACT

We report herein measurements of polarizations and angular distributions in the elastic scattering of pions and protons from polarized protons. The data cover the kinematic range $0.2 \leq -t \leq 1.6 \text{ GeV}^2$ at incident momenta of 100 GeV for pions and 100 and 300 GeV for protons. The detector was a double-arm spectrometer whose components were multi-wire proportional chambers and analysis magnets.

These measurements represent the first polarization measurements at Fermilab-SPS energies, and as such provide new constraints on strong interaction phenomenology. Eikonal models are discussed, with particular reference to the absorption model of the Michigan school, and the data presented with model fits. The pi polarization data are found to be consistent with the predictions of both this model and of a pure pole Regge model. The pi angular distributions are found to be consistent with existing differential cross-section data, and are more precise for $-t > 0.8 \text{ GeV}^2$. The pp polarization data confirm trends suggested by the Serpukhov data, with the low t polarization decreasing more rapidly than would be expected in an exchange degenerate pure pole model, and with the polarization becoming negative and increasing in magnitude with increasing $-t$. The data are consistent with the model predictions at small and intermediate t , and are suggestive of the structure predicted by this and other models in the region of the dip in the 300 GeV differential cross-section. The pp angular distributions are again consistent with existing differential cross-section data, with the dip observed in the present data at $t \approx -1.5 \text{ GeV}^2$.

Acknowledgements

The success of any experiment of this size depends on the cooperative and individual efforts of many persons. My deep thanks go to all of my collaborators: Paul Auer, Dan Hill, Bernie Sandler, Dave Underwood, and Aki Yokosawa of Argonne; Walter Brückner, Owen Chamberlain, Gil Shapiro, and Herb Steiner of Berkeley; Peter Koehler and Alan Jonckheere of Fermilab; Bob Kline, Margaret Law, and Frank Piplin of Harvard; Walter Johnson of Suffolk University; and Michael Zeller of Yale.

While listing the contributions to the experiment of each of my collaborators would take pages, I especially wish to thank Bob Kline for his assistance with the data analysis, and Dan Hill, who developed the polarized proton target, for the many sleepless hours spent tending the target cryogenics. I would also like to recognize here the many hours Bob Kline and Peter Koehler contributed to the experiment.

Among those persons not formally listed as collaborators, Ray Fuzesy of Berkeley must be singled out for his invaluable work. Without slighting his other contributions, I mention his construction of seventeen planes of proportional wire chambers, comprised of some 3500 wires. My gratitude also goes to Ed Sadowski of Harvard for his design and construction of the Cherenkov counters, Orris Fletcher of Argonne for his work with the polarized target,

Cordon Kerns of Fermilab for assistance with the polarized target readout system, Satish Dhawan for the design of the proportional chamber readout system, Marcel Urban and Tom Droege for their contributions to the online data acquisition system. I also wish to thank Leo Ray of Fermilab for his considerable work on the mechanical structures of the experiment, the Cryogenics Group at Fermilab for providing and maintaining the two superconducting magnets, and the crew of the Meson Lab for maintaining the beam line.

I also wish to acknowledge numerous conversations with, and generous assistance from Andy Seidl of the University of Michigan during the period when I was implementing the Michigan absorption model. I am also very grateful to Dick Patton, a fellow graduate student during my first three years at Yale, for his help and advice.

My deepest thanks go to Michael Zeller, my advisor at Yale, both for his guidance through five years of graduate study, and for the example he has provided as a working experimental physicist; and to my family for their unflagging encouragement and support.

Finally I wish to thank Laurie Liptak and Pat Fleming and Judy Fisher for suffering through several revisions in the course of typing this thesis; and Jim Brosius for the elegant drawings reproduced here.

Table of Contents

Acknowledgements	ii
List of Tables	vi
List of Illustrations	vii
Introduction	1
Chapter I - A Quick Look at Regge Phenomenology	8
I. Introduction	8
II. Pion-Nucleon Scattering	8
A. Definitions and Kinematics	8
B. Regge Predictions for π^p Scattering	15
III. Proton-Proton Polarizations	30
A. Definitions	30
B. Regge Predictions of PP Polarizations	32
IV. Cuts	
A. The Existence of Cuts	39
B. Models for Cuts	42
C. The Eikonal/Absorption Model	46
References for Chapter I	65
Chapter II - The Experimental Apparatus	67
I. Introduction	67
II. The Detector	70
III. Logic	82
IV. Beam	92
V. Cerenkov Counters	99
VI. Polarized Proton Target	104
VII. Monitors	105
VIII. CAMAC and the On-Line Program	108
IX. The On-Line Program	110
References for Chapter II	114

Chapter III - Data Analysis	115
I. Introduction	115
II. The Condensed Tape Program	116
III. The Analysis Program	119
IV. The Summary Program	130
V. The Display Program	133
VI. The Polarization Program	143
Chapter IV - Results and Conclusions	145
I. πp Scattering	145
II. pp Scattering	162
III. Summary	195
References for Chapter IV	198
Appendix I - Summary of the Michigan Absorption Model	199
Appendix II - Transport for the M1 Beam	204

List of Tables

II-1	Details of PWC Resolution and Positioning	76
II-2	Acceptances for Background Events	79
III-1	Error Table for Polarization Data	144
IV-1	π^+p Angular Distribution Data	151
IV-2	π^+p Polarization Data	152
IV-3	π^-p Angular Distribution Data	153
IV-4	π^-p Polarization Data	154
IV-5	pp Angular Distribution Data	176
IV-6	pp Polarization Data	178
AII-1	M1 Beam Line Properties	205

List of Illustrations

I-1	Channels and Momenta for πp Scattering	11
I-2	s-t-u Diagram for πp Scattering	14
I-3	Chew-Frautschi Plot for Mesons	17
I-4	πp Charge Exchange Differential Cross-Sections	21
I-5	The rho Trajectory	24
I-6	πp Polarization data at various energies	27
I-7	s-t-u Diagram for pp scattering	34
I-8	pp Polarization Data at 10 and 12.3 GeV	38
I-9	Regge Exchange Diagrams	45
I-10	Fit to the pp Differential Cross-Section	51
I-11	Regge Exchange Diagrams	54
I-12	Amplitudes Before and After Absorption	61
I-13	Fits to Polarization Data	64
II-1	The Detector	72
II-2	Acceptance Curve for Elastic Events	74
II-3	Use of Matrix Coincidence Units	86
II-4	Fast Logic Schematic	88
II-5	Placement of Counters Around Target	90
II-6	Schematic of Beam Line	94
II-7	Spin Precession Magnet Placement	98
II-8	Cerenkov Counter ADC Spectra	102
II-9	Data Flow Schematic	112
III-1	Coordinate System Used in the Analysis	122
III-2	Chi-Square Plot	124
III-3	Coplanarity Plot	126
III-4	Various Analysis Plots	129

III-5	Signal and Background Regions	132
III-6	Monitor Plots	135
III-7	Background Asymmetries	140
IV-1	πp Angular Distribution Data	147
IV-2	πp Polarization Data	150
IV-3	πp Differential Cross-Section Data with Model Fits	159
IV-4	πp Polarization Data with Model Fits	165
IV-5	pp Angular Distribution Data	171
IV-6	pp Polarization Data	174
IV-7	pp Polarization Data with Model Fits	183
IV-8	pp Differential Cross-Section Data with Model Fits	186
IV-9	pp Polarization Data at 24 GeV	190
IV-10	pp Polarization Data with Spin Precision Magnets Absent	193

INTRODUCTION

We present here the results of the first polarization measurements in the Fermilab-SPS energy region. We have measured the polarization parameter in pion-nucleon scattering at 100 GeV and in proton-proton scattering at 100 and 300 GeV. By detecting both recoil and forward scattered particles we have been able to reject inelastic and quasi-elastic events and to maintain signal to background ratios ranging from 15:1 to 5:1 over most of the acceptance of the apparatus, $0.20 < -t < 1.8 \text{ GeV}^2$. We expect our data, when combined with lower energy polarization data, to provide strong constraints on present models of the strong interaction.

As is well known, there exists no complete fundamental theory of strong interactions today. The techniques of the most successful physical theory, quantum electrodynamics, are not immediately relevant, since in that theory physical quantities are calculated in a series expansion in powers of the coupling constant, $\alpha = e^2/hc \sim 1/137$, while in strong interactions the coupling constants are so large that the expansion diverges. While recent theoretical advances, particularly in the understanding of non-abelian gauge theories, hold promise for a theory of strong interactions as fundamental

as quantum electrodynamics, at present this theory has not been worked out in detail.¹ In the absence of a complete theory a phenomenology of the strong interactions has been developed, based on a few very general principles, such as Lorentz invariance and analyticity of the S-matrix, and guided by experimental data. It has been hoped that the data, by restricting the phenomenology, would eventually guide the way to a unique theory which alone would be capable of explaining all of the data. Put another way, measuring new physical quantities or extending the measurements of physical quantities into new physical regions, and by doing so requiring the theory to explain phenomena outside the region in which it is known to be valid, is likely to improve understanding of the theory and to reveal its weaknesses.

We will be interested in the branch of strong interaction phenomenology, the Regge theory, which relates the behavior of scattering amplitudes to singularities in the complex angular momentum plane. Regge poles were first shown to exist in non-relativistic potential scattering,² but have been most useful in high energy Physics: the observed particle spectrum is organized naturally into families of particles, called trajec-

tories, in which all particles have all quantum numbers the same except for spin, the spin being related to the mass of a particle within the family by

$$M_J^2 = \mu^2(J-k)$$

where the constants μ^2 and k are the same within a family.³ The theory represents an improvement over the earlier one-particle exchange⁴ and other models in that higher spin particles, the Regge recurrences, are quite natural. (Recall that in quantum electrodynamics, amplitudes increase with energy as s^J , where J is the spin of the exchange particle,⁵ and so eventually violate the unitarity bound if J is greater than or equal to 1.) In fact the contribution of a Regge trajectory to an amplitude can be obtained as the (formal) sum of one particle exchange Feynman diagrams.³

Simple Regge pole models had a number of notable successes, e.g. in predictions of shrinkage in amplitudes dominated by a single exchanged trajectory, in the correct energy dependence of amplitudes dominated by t channel exchanges, and in the overall usefulness of the Regge scheme as a general framework for organizing experimental data.⁶ Of particular interest to us is the natural explanation of the mirror symmetry between π^+p and π^-p elastic polarizations.⁷ Nor does this list exhaust the successes of the theory.

On the other hand, there have been several indications,

both theoretical and experimental, that J plane singularities other than poles are necessary.⁸ Theoretically, it seems that fixed poles must exist, and the presence of these implies the presence of cuts.⁹ Experimentally, there have been many indications of non-pole behavior, among them the many failures of factorization, the presence of peaks in differential cross-sections where dips were expected, and the substantial polarization observed in πp charge exchange scattering. It has also been clear for some time that initial and final state interactions must be present, and these are usually assumed to lead to cuts.³ Thus there have been attempts to make (model dependent) rescattering corrections to pure pole theories; the resulting absorption models have had considerable success in fitting the data, and we will consider them at some length in the next chapter.

Regardless of the state of the phenomenology, there are several reasons to measure the polarization in elastic hadron scattering at Fermilab energies. While differential cross section measurements have confirmed the Regge behavior of the dominant (generally diffractive) amplitude,¹⁰ the differential cross section, being the sum of squares of amplitudes, is not particularly sensitive to variations of the smaller amplitudes. Interference phenomena such as the polarization or the R and A parameters are thus the only practical means of determining the behavior of the other amplitudes. This is especially true at high energies, since the pole amplitudes fall off relatively faster than the diffractive amplitude with

increasing energy. Thus measurements of the observables which are sensitive to the nondiffractive amplitudes are important in understanding the spin dependence of the strong interactions and as constraints on models.

The discovery of the dip in elastic pp scattering¹¹ at laboratory energies above 100 GeV, evidence that even at these energies the amplitudes have structure, is added motivation for a measurement of the pp elastic polarization. Experimental data on observables in the dip region are inevitably interesting as a test of ideas of diffractive scattering.¹² Another, somewhat less expected observation, of significant polarization in inclusive lambda production¹³ is evidence that even at high energies the polarization may not go to zero at small (but non-zero) t . Finally, as mentioned earlier, one of the most valuable ways of generating new insights into a theory is to apply it in regions outside those in which it has been shown valid. One might wonder if the energy dependence predicted by pole theories is valid all the way from Brookhaven to Fermilab energies, for example.

The plan of the dissertation is as follows: in Chapter I we give a very brief discussion of Regge phenomenology as it pertains to πp and pp elastic scattering. Chapter II is devoted to a description of the apparatus, Chapter III to the method of data reduction, and finally in Chapter IV the data from the experiment are presented and compared with the predictions of the absorption model of the Michigan school.¹⁴

References for the Introduction

1. See, for a recent review, J. Bernstein, Spontaneous symmetry breaking, gauge theories, the Higgs mechanism, and all that, Rev. Mod. Phys. 46, 7 (1974).
2. Regge, T., Nuovo Cimento, 14, 951 (1959).
Regge, T., Nuovo Cimento, 18, 947 (1960).
3. See, e.g. Barger, V., and D. Cline, Phenomenological Theories of High Energy Scattering, Benjamin, 1969.
4. See Gottfried, K., and J.D. Jackson, Nuovo Cimento 34, 735 (1964), and references therein.
5. See e.g., Bjorken, J., and S. Drell, Relativistic Quantum Fields, McGraw-Hill 1964.
6. Chiu, S., Rev. Nucl. Sci., (1972), reviews the successes of the theory.
7. We discuss πp polarizations in Chapter I.
8. Collins, P.D.B., in Regge Theory and High Energy Physics, Cambridge 1977, summarizes the evidence for cuts.
9. This point is discussed by Collins, P.D.B. Phys. Rept. 1, 103 (1971).
10. Antipov, Yu. M., et al., Nucl. Phys. B57, 333 (1973).
Allaby, J.V., et al., Nucl. Phys. B52, 316 (1973).
Fermilab Single Arm Spectrometer Group, Phys. Rev. Lett. 35, 1195 (1975).
Akerlof, C.W., et al., Phys. Rev. D14, 2864 (1976).
11. Bohm, A., et al., Phys. Lett. 49B, 491 (1974).
Kwak, N., et al., Phys. Lett. 58B, 233 (1975).

12. Chou, T.T., and C.N. Yang, Phys. Rev. 170, 1591 (1968).
Chou, T.T., and C.N. Yang, Phys. Rev. Lett. 20, 1213 (1968).
Byers, N., Oxford preprint (unpublished) (1973).
Chu, S., and A.W. Hendry, Phys. Rev. D6, 190 (1972).
13. Bunce, G., et al., Phys. Rev. Lett. 36, 1113 (1976).
14. Kane, G., and A. Seidl, Rev. Mod. Phys. 48, 309 (1976).

A QUICK LOOK AT REGGE PHENOMENOLOGY

I. Introduction

In this chapter we briefly discuss current theoretical understanding of strong interaction phenomenology as it pertains to pion-nucleon and nucleon-nucleon polarizations. We divide the chapter into three sections. In the first we discuss pion-nucleon scattering, which is fairly well understood in terms of the pure pole Regge models.¹ In fact, the explanations of the πp charge exchange differential cross-sections and of the elastic polarizations are considered two of the major successes of the theory. In the middle section we consider pp polarizations and show that this same theory leads to the prediction of structureless polarization for $-t < 1.5 \text{ GeV}^2$. This discrepancy leads us to consider cuts in the final section: after reviewing some of the evidence for cut singularities (or more precisely, the failures of the pure pole models) we consider two popular cut models, and close by noting a few of the successes of pole models with cuts.

II. Pion-Nucleon Scattering

A. Definitions and Kinematics. Before considering the predictions of Regge models, we introduce the definitions and kinematics appropriate to pion-nucleon scattering, both for general orientation and to specify our normalizations so that our equations can be compared with those of other authors.²

For scattering in the s-channel, let the 4-momenta be defined as in Figure I-1, with $p_1(p_3)$ and $p_2(p_4)$ the incident (scattered) momenta of the pion and nucleon. The transition or T matrix is defined in the usual fashion:

$$T(s,t) = \frac{1}{2M} \{A(s,t,u) + \frac{(p_1 + p_3)}{2M} B(s,t,u)\} \quad (1)$$

with s , t , and u the Mandelstam variables

$$s = (p_1 + p_2)^2 \quad (2a)$$

$$t = (p_1 - p_3)^2 \quad (2b)$$

$$u = (p_1 - p_4)^2 \quad (2c)$$

M the mass of the target nucleon. We will deal exclusively with helicity amplitudes $T_{\lambda',\lambda}$, defined by

$$T_{\lambda',\lambda} = \langle \lambda' | T | \lambda \rangle = \bar{u}^{\lambda'}(p_4) T u^{\lambda}(p_2)$$

with λ' and λ final and initial helicities. Explicitly,

$$T_{++} = \cos \frac{1}{2}\theta \left\{ A + \frac{s - M^2 - \mu^2}{2M^2} B \right\} \quad (4a)$$

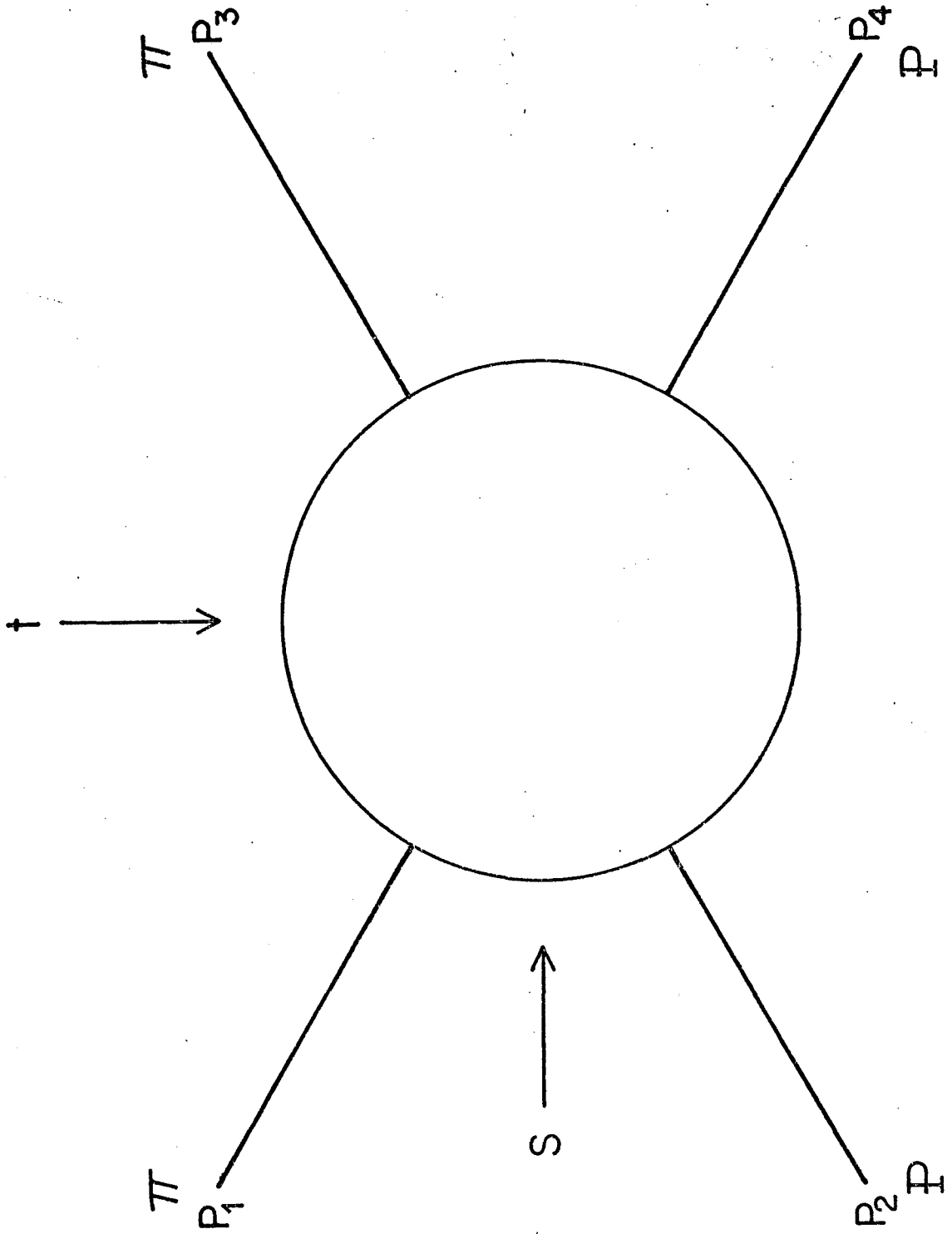
$$T_{-+} = \frac{-\sin \frac{1}{2}\theta}{2M\sqrt{s}} \left\{ (s + M^2 - \mu^2)A + (s - M^2 + \mu^2)B \right\} \quad (4b)$$

with μ the pion mass, and θ the CM scattering angle, and Dirac spinors u normalized by

$$\bar{u}^{\lambda'}(P) u^{\lambda}(P) = 2M\delta_{\lambda',\lambda} \quad (5)$$

We can relate helicity amplitudes to spin-orbit amplitudes by defining

Figure I-1. Definition of channels and momenta for πp scattering.



$$f_{\lambda',\lambda} = \frac{1}{8\pi\sqrt{s}} T_{\lambda',\lambda} \quad (6)$$

Then in terms of the non-flip spin-orbit amplitude f and the flip amplitude g we have

$$f_{++} = f \cos \frac{1}{2}\theta + g \sin \frac{1}{2}\theta \quad (7a)$$

$$f_{-+} = -f \sin \frac{1}{2}\theta + g \cos \frac{1}{2}\theta \quad (7b)$$

Our total and differential cross-sections are then

$$\sigma_{TOT} = -(2q\sqrt{s})^{-1} \sum \text{Im } T_{\lambda\lambda} \quad (8)$$

$$d\sigma/dt = (128q^2s)^{-1} \sum |T_{\lambda',\lambda}|^2 \quad (9)$$

with q the CM momentum, while the polarization is given by

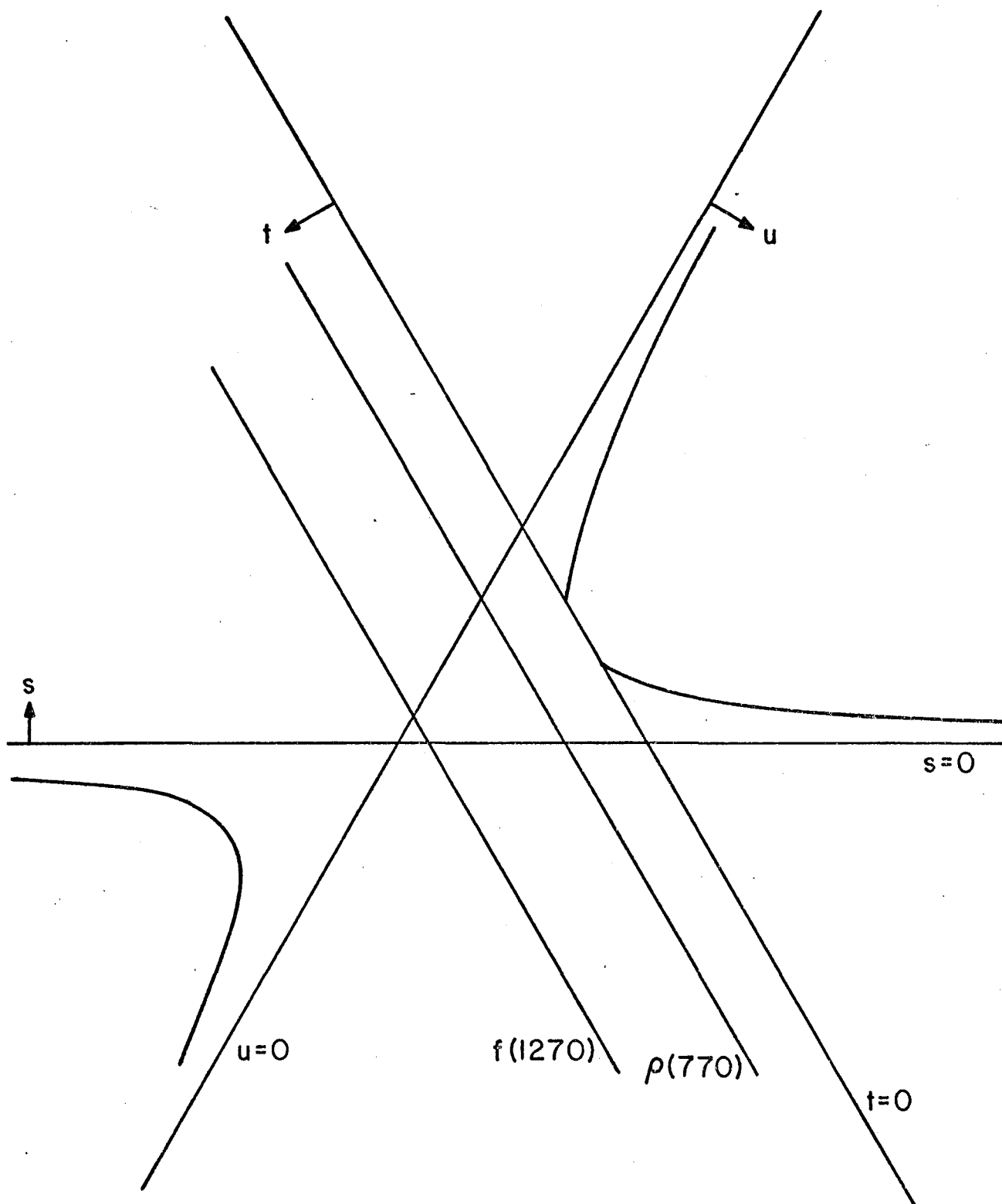
$$\underline{P} = \frac{-2\text{Im}(T_{++}T_{-+}^*)}{|T_{++}|^2 + |T_{-+}|^2} \quad (10)$$

The amplitudes A and B , which have no kinematic singularities, satisfy the Mandelstam relation, and hence are the proper amplitudes to continue between channels. For the π^+p system there are three channels described by the same A and B :

- (i) s channel: $\pi^+p \rightarrow \pi^+p$
- (ii) t channel: $\pi^+\pi^- \rightarrow \bar{p}p$
- (iii) u channel: $\pi^-p \rightarrow \pi^-p$

Figure I-2 shows the physical regions for each reaction, plotted in a triangular coordinate system, together with the poles of the A and B amplitudes.

Figure I-2, s-t-u diagram showing the physical regions of the πp system and the t channel poles.



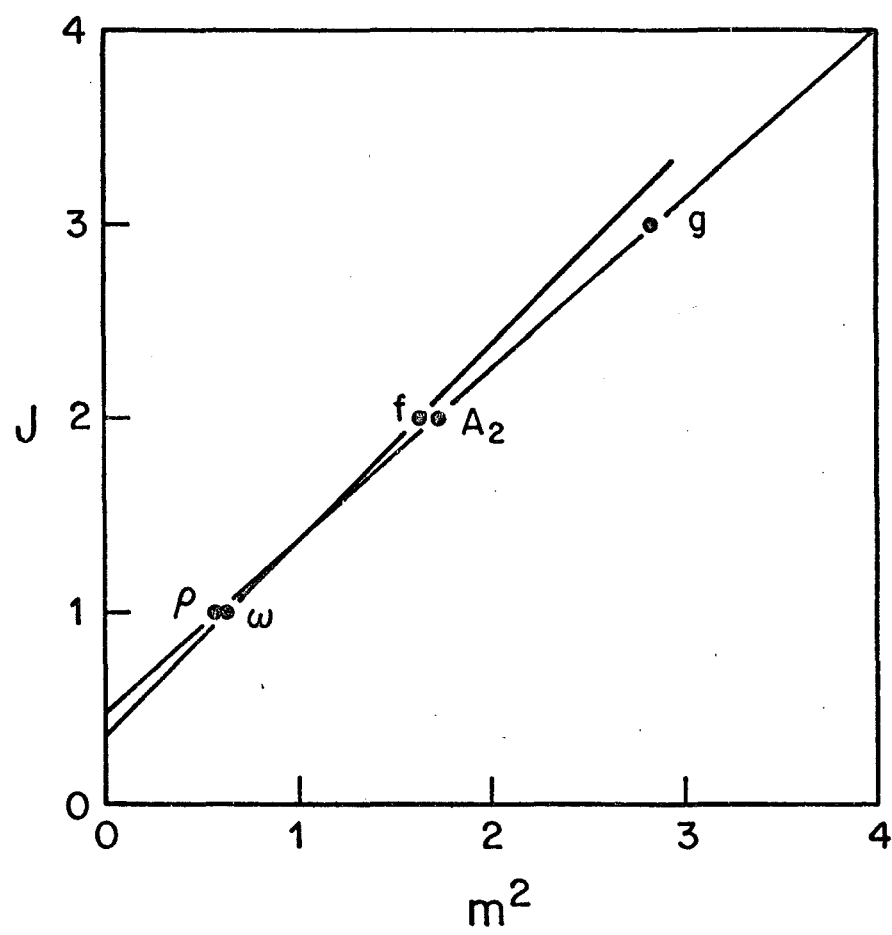
B. Regge Predictions for πP Scattering. As we mentioned in the Introduction, forward pion nucleon scattering is well described by Regge pole models, in which s channel phenomena arise from the exchange of families of particles in the crossed t channel. These families, called trajectories, are identified with a common function $\alpha(t)$, and have definite quantum numbers in the t channel. Particles within a family are related by the trajectory relation

$$\text{Re } \{\alpha(t=m^2)\} = J$$

with m the mass of a particle on the trajectory, and J its intrinsic spin, other quantum numbers being the same. Analyticity and crossing require that even and odd spins, characterized by the signature $\xi = (-)^J$, be considered separately; in effect the signature is another quantum number describing the trajectory. The t channel for $\pi^+ p \rightarrow \pi^+ p$ is $\pi^+ \pi^- \rightarrow \bar{p} p$; the trajectories with the quantum numbers of $\pi^+ \pi^-$ are the $f(I=0)$ and the $\rho(I=1)$. We display these trajectories, along with the exchange degenerate ω and A_2 trajectories in Figure I-3. In addition the Pomeron, associated with diffraction scattering, couples to $\pi^+ \pi^-$, but is not known to be associated with any physical particles.

The specific forms of the Regge amplitudes, which will be important when we compare the existing data with Regge predictions, have been derived in many places using the Sommerfeld-Watson transformation, hence we simply note the forms of the helicity amplitudes in the t channel:³

Figure I-3. Chew-Frautschi plot for the natural parity mesons.



$$T_{++} = \frac{\gamma_{++}(t)}{\sqrt{t-4M^2}} F(\alpha) \left(\frac{s}{s_0}\right)^\alpha \quad (11a)$$

$$T_{-+} = \gamma_{-+}(t) \sqrt{t(t-4\mu^2)} \sin\theta \alpha F(\alpha) \left(\frac{s}{s_0}\right)^{\alpha-1} \quad (11b)$$

with

$$F(\alpha) = \frac{(\alpha + \frac{1}{2})!}{\alpha!} \frac{\xi + e^{-i\pi\alpha}}{\sin \pi\alpha} \quad (12)$$

where ξ is the signature of the trajectory, the γ 's are residue functions, and $\alpha = \alpha(t)$. The amplitudes have been written with residues free of kinematic singularities. We first consider the energy behavior of the amplitudes, and note immediately that if α_1 and α_2 are the two highest trajectories then from eqns (8)-(10)

$$\sigma_{TOT} \rightarrow C(s/s_0)^{\alpha_1(0)-1} \quad (13)$$

$$\frac{d\sigma}{dt} \rightarrow D(t) \left(\frac{s}{s_0}\right)^{2\alpha_1(t)-2} \quad (14)$$

$$P(t) \rightarrow G(t) \left(\frac{s}{s_0}\right)^{\alpha_2(t)-\alpha_1(t)} \quad (15)$$

as $s \rightarrow \infty$. Since the phase of a Regge pole term is given entirely by the signature factor,

$$\frac{\xi + e^{i\pi\alpha}}{\sin \pi\alpha}$$

which contributes to both helicity amplitudes in the same way, we see that if only one trajectory contributes, the

polarization will be zero.

The three reactions

$$\pi^- p \rightarrow \pi^- p \quad (16a)$$

$$\pi^+ p \rightarrow \pi^+ p \quad (16b)$$

$$\pi^- p \rightarrow \pi^0 n \quad (16c)$$

are related by isospin invariance. Choosing the signs conventionally, we have

$$T(\pi^- p \rightarrow \pi^- p) = T(I=0) + T(I=1) \quad (17a)$$

$$T(\pi^+ p \rightarrow \pi^+ p) = T(I=0) - T(I=1) \quad (17b)$$

$$T(\pi^- p \rightarrow \pi^0 n) = 2 T(I=1) \quad (17c)$$

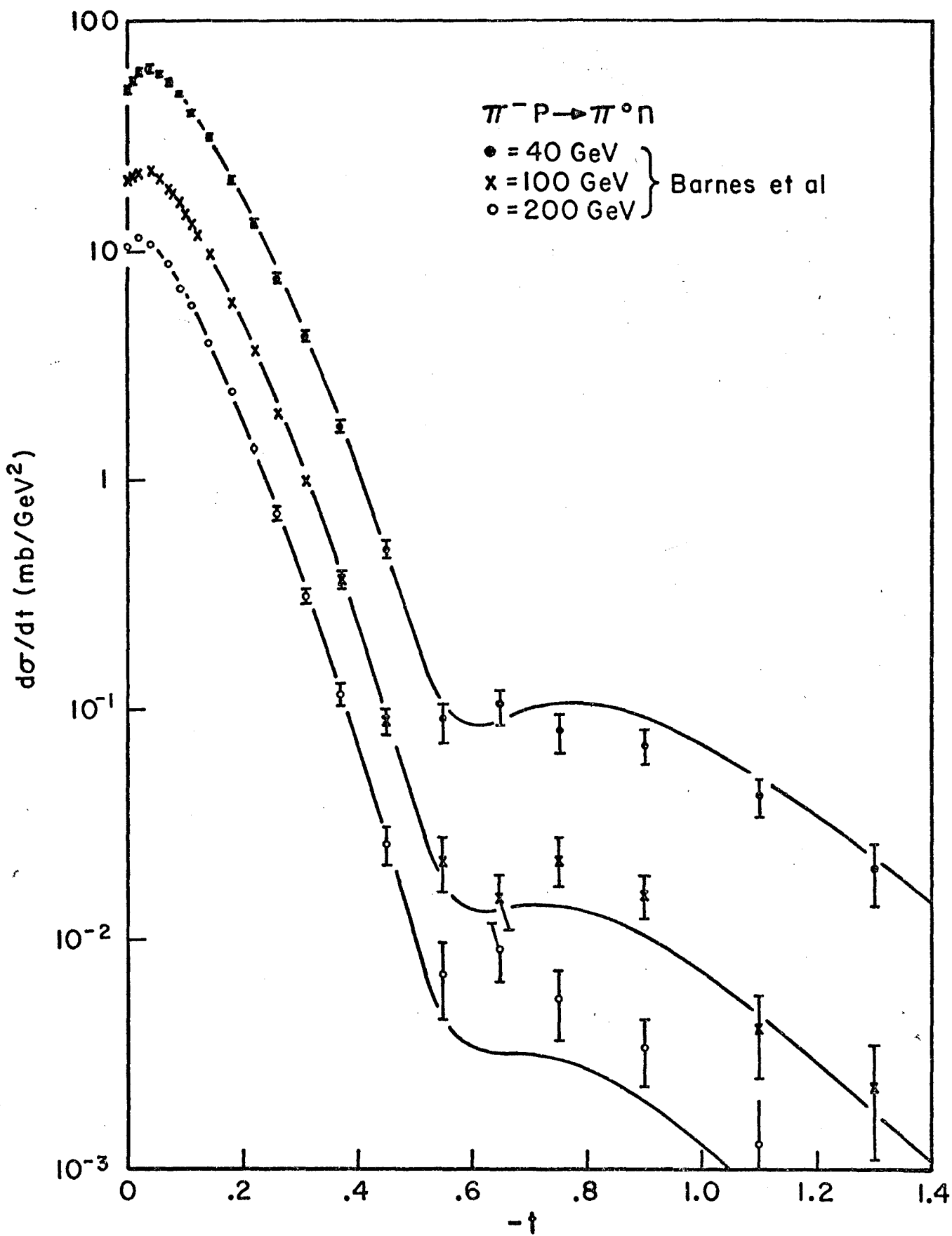
so by first considering the charge exchange reaction we can look immediately at the isovector exchange, without worrying about interference from the isoscalar piece. From eqn. (17) and the line reversal property⁴ the isovector must have odd signature; the only $I=1$, $\xi=-1$ trajectory available is the ρ .

Data exists for the charge exchange differential cross-section^{5,6} from 6 GeV up to 200 GeV; we show several points in figure I-4. Looking at eqn.(14), we see that at fixed t

$$\log \left(\frac{d\sigma}{dt} \right) \rightarrow \log D(t) + (2 \alpha_\rho(t) - 2) \log (E/E_0), \quad (18)$$

so the value of α_ρ can be found from the slope on a $\ln (d\sigma/dt)$ versus $\ln (E)$ plot. It is found that α_ρ is approximately linear, and that a straight-line extrapolation to positive

Figure I-4. πp charge exchange differential cross-sections.
The solid lines are fits from Ref. 5.



t passes near the ρ and g masses. The classic analysis is for the data less than 20 GeV by H hler,⁶ who obtains

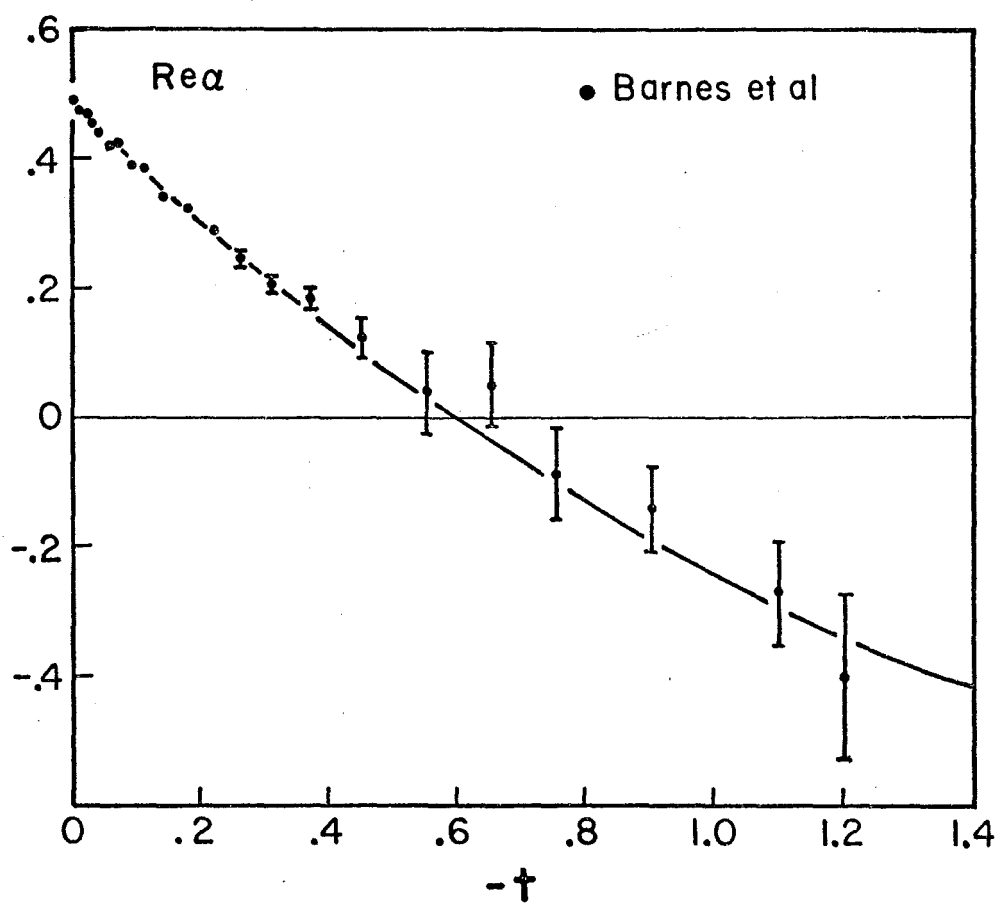
$$\alpha_{\rho}(t) = .58 + 1.0 t$$

while the higher energy data,⁵ though qualitatively consistent, are best fit by a trajectory (figure I-5)

$$\alpha_{\rho}(t) = 0.48 + 0.93 t + 0.2 t^2.$$

The most striking feature of the differential cross-section data is the pronounced dip around $t = -0.6 \text{ GeV}^2$. The usual explanation is that this results from the helicity flip amplitude vanishing at the nonphysical value $\alpha = 0$ of the angular momentum (a "nonsense wrong signature zero"). This can be seen explicitly in eqn. (11b). Also note the dip at $t = 0$, again a result of the vanishing of the helicity flip amplitude to satisfy kinematic constraints. In figure I-4 we have drawn curves through the data according to the residue of ref. 5 and the trajectory of eqn. (20); it is apparent that a single exchanged trajectory fits the data quite well (ref. 5 quotes a χ^2 of 107 for 128 degrees of freedom). This is one of the major successes of the simple pole model, as we noted earlier. Unfortunately, a model with a single exchanged trajectory predicts zero polarization, while experimentally polarizations of ~20-40% have been observed.⁷ While this is possibly caused by a lower lying trajectory, it appears that the most likely explanation is pole-cut

Figure I-5. The ρ trajectory determined from the differential cross-section data of Ref. 5.



interference;¹ we will consider further evidence for cuts, and particular cut models later.

Next consider πp elastic scattering. Referring back to eqn. (17) we see that two amplitudes are involved: the isovector ρ amplitude, and an isoscalar amplitude which we identify with the Pomeron and the f . Thus our amplitudes are

$$T(\pi^+ p) = P + f - \rho \quad (21a)$$

and

$$T(\pi^- p) = P + f + \rho \quad (21b)$$

in an obvious notation, with the polarization given by eqn. (10). The relative signs are given by SU(2) Clebsch-Gordon coefficients. Figure I-6 shows the polarization data⁸ at 6, 10, and 14 GeV. We can duplicate the major features of the data within a pure pole model in the following way:¹ we assume that the (nearly) pure imaginary Pomeron dominates the non-flip amplitude, thus

$$T_{++} \cong i \operatorname{Im} (P_{++}) \quad (22)$$

and that the ρ dominates the flip amplitude, so that

$$T_{-+} \cong \rho_{-+}. \quad (23)$$

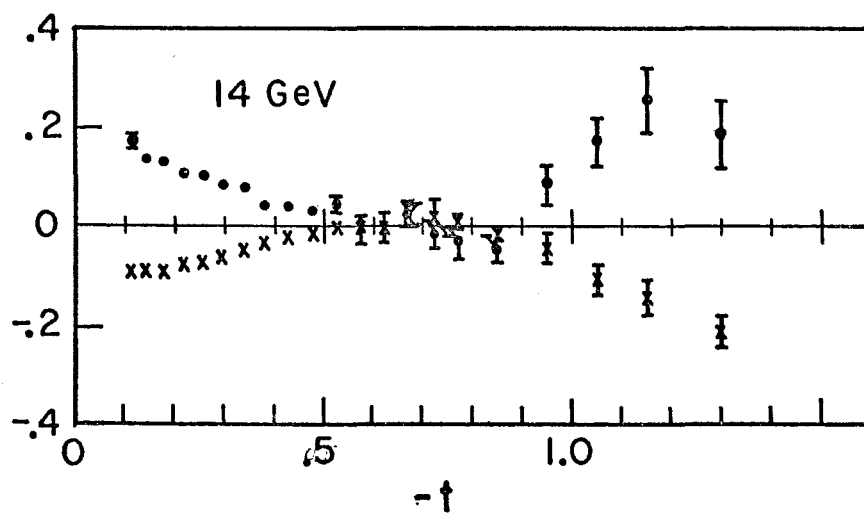
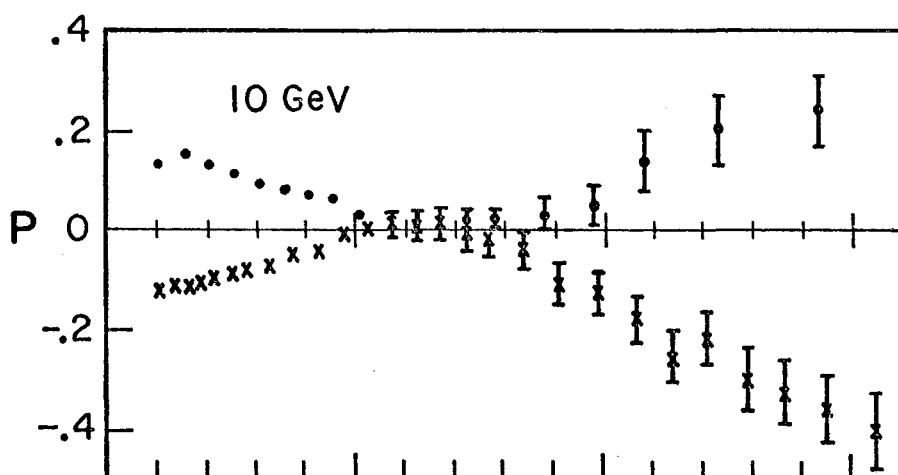
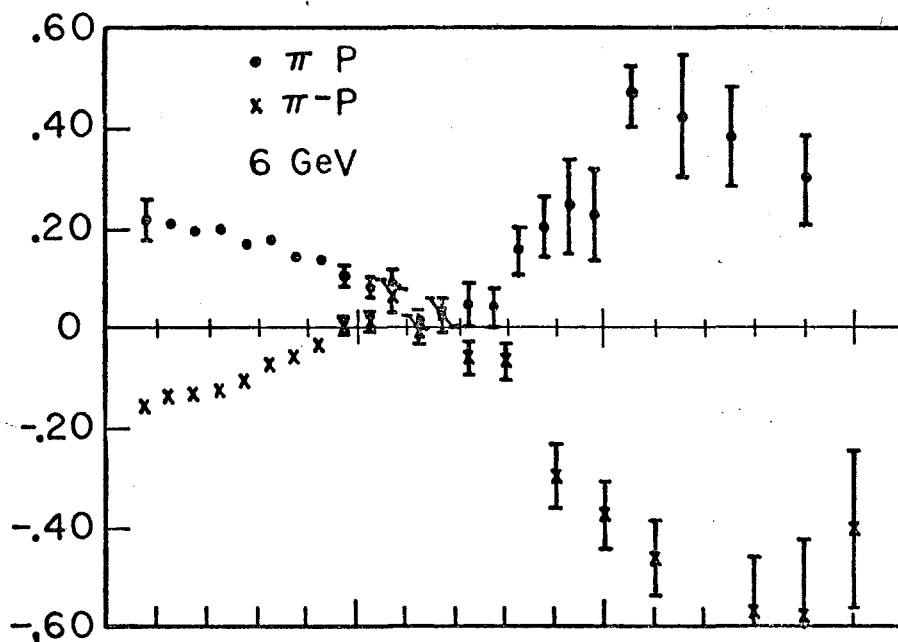
Then

$$P(\pi^+ p) \approx \frac{2 \operatorname{Re} \rho_{-+} \operatorname{Im} P_{++}}{|T_{++}|^2 + |T_{-+}|^2} \quad (24)$$

while

$$P(\pi^- p) \approx \frac{-2 \operatorname{Re} \rho_{-+} \operatorname{Im} P_{++}}{|T_{++}|^2 + |T_{-+}|^2} \quad (24b)$$

Figure I-6. πp polarization data at 6, 10, and 14 GeV.
Data from Ref. 8.



so we immediately find the polarizations to be mirror symmetric. The other notable feature of the data, the double zero at $t=-0.6$, is a result of letting the ρ dominate the flip amplitude, since from eqn. (11) and (12),

$$\begin{aligned} \text{Re}(\rho_{-+}) &\sim (1 - \cos \pi \alpha_\rho) s^{\alpha_\rho} \\ &= 2 \sin^2 \left(\frac{\pi \alpha_\rho}{2} \right) s^{\alpha_\rho}, \end{aligned} \tag{25}$$

which goes to zero as α^2 as α tends to zero. Again for the trajectory, this zero is at $t \approx -0.55$. Thus the dip in the charge exchange differential cross-section and the double zero in the elastic polarizations find a natural explanation in the nonsense zero of the ρ helicity flip amplitude. The polarization is consistent with this two-pole model up to 17 GeV, and possibly up to Serpukhov energies. On the other hand, there is some indication in the Serpukhov data of non-Regge behavior; in particular it is not clear that the π^+p data at 45 GeV scale as expected.⁹ This also shows up in the sum of the polarizations

$$\Sigma = P(\pi^+p) + P(\pi^-p) \tag{26}$$

which should be proportional to the isoscalar flip amplitude. Some authors have interpreted this as an indication that the Pomeron has developed a flip component with phase different from the non-flip component.¹⁰ But the statistics on the polarizations are really not good enough to draw any firm conclusions.

Thus this experiment, with π^+p and π^-p polarizations at 100 GeV, aside from being a measurement in a completely new energy regime, enables us to see if this non-Regge behavior tentatively identified at Serpukhov becomes more apparent. As we shall see later, cut terms are expected to differ in energy dependence from poles by factors of $\ln s$, so one might expect to see the effects of cuts the more easily the higher the energy.

III. Proton-Proton Polarizations

A. Definitions. In proton-proton scattering the presence of non-zero spin on the beam and target particles leads to a much more complicated description of the observables. Instead of two amplitudes, one helicity flip and one non-flip, there are now five. Following the notation of Goldberger et al.¹¹ we write

$$\phi_1 = \langle ++ | T | ++ \rangle = \langle -- | T | -- \rangle \quad (27a)$$

$$\phi_2 = \langle ++ | T | -- \rangle = \langle -- | T | ++ \rangle \quad (27b)$$

$$\phi_3 = \langle +- | T | +- \rangle = \langle -+ | T | -+ \rangle \quad (27c)$$

$$\phi_4 = \langle +- | T | -+ \rangle = \langle -+ | T | +- \rangle \quad (27d)$$

$$\phi_5 = \langle ++ | T | +- \rangle = \langle -- | T | -+ \rangle \quad (27e)$$

$$= -\langle +- | T | ++ \rangle = -\langle -- | T | +- \rangle$$

$$= -\langle +- | T | -- \rangle = -\langle -+ | T | ++ \rangle$$

$$= -\langle ++ | T | -+ \rangle = -\langle -+ | T | -- \rangle$$

where ϕ_1 , ϕ_2 , and ϕ_3 are net helicity non-flip amplitudes, and ϕ_5 and ϕ_4 are single- and double-flip amplitudes. As $t \rightarrow 0$, $\phi_5 \sim \sqrt{-t}$, and $\phi_4 \sim t$, while the non-flip amplitudes can remain non-zero. Following Halzen and Thomas,¹² we can write combinations of the ϕ which have (asymptotically) definite quantum numbers in the t channel:

$$N_0 = \frac{1}{2} (\phi_1 + \phi_3) \quad (28a)$$

$$N_1 = \phi_5 \quad (28b)$$

$$N_2 = \frac{1}{2} (\phi_4 - \phi_2) \quad (28c)$$

$$A = \frac{1}{2} (\phi_1 - \phi_3) \quad (28d)$$

$$\pi = \frac{1}{2} (\phi_4 + \phi_2). \quad (28e)$$

N_0 , N_1 , and N_2 are natural parity exchange, while A and π correspond to unnatural parity exchange with A_1 and π/B quantum numbers. The observables σ_T , $d\sigma/dt$, and P can be written

$$\sigma_{TOT} = -1/8qW \operatorname{Im} (\phi_1(0) + \phi_3(0)), \quad (29)$$

$$d\sigma/dt = (1/256\pi q^2 s) (|\phi_1|^2 + |\phi_2|^2 + |\phi_5|^2 + |\phi_4|^2 + 4|\phi_5|^2) \quad (30)$$

and

$$P = \frac{-2 \operatorname{Im} \{(\phi_1 + \phi_2 + \phi_3 - \phi_4)\phi_5^*\}}{|\phi_1|^2 + |\phi_2|^2 + |\phi_3|^2 + |\phi_4|^2 + 4|\phi_5|^2} \quad (31)$$

As with πp elastic scattering, we can construct invariant amplitudes by extracting appropriate kinematic factors; the resulting singularity free amplitudes are¹³

$$F_1 = q^2 \phi_1 \quad (32a)$$

$$F_2 = q^2 \phi_2 \quad (32b)$$

$$F_3 = \phi_3 / (1 + \cos\theta) \quad (32c)$$

$$F_4 = \phi_4 / (1 - \cos\theta) \quad (32d)$$

$$F_5 = \phi_5 / \sqrt{s} \sin \theta \quad (32e)$$

The three channels which are described by these amplitudes are

(i) s channel: $pp \rightarrow pp$

(ii) t channel: $p\bar{p} \rightarrow \bar{p}p$

(iii) u channel: $p\bar{p} \rightarrow p\bar{p}$

Figure I-7 shows the physical regions for each channel, together with the lowest lying poles in the t-channel. Note that many more poles couple to the pp system than to the $\pi^+\pi^-$ system; pp elastic scattering is more complicated than πp not only because of the richer spin structure, but also because the singularity structure of the amplitudes is more complex.

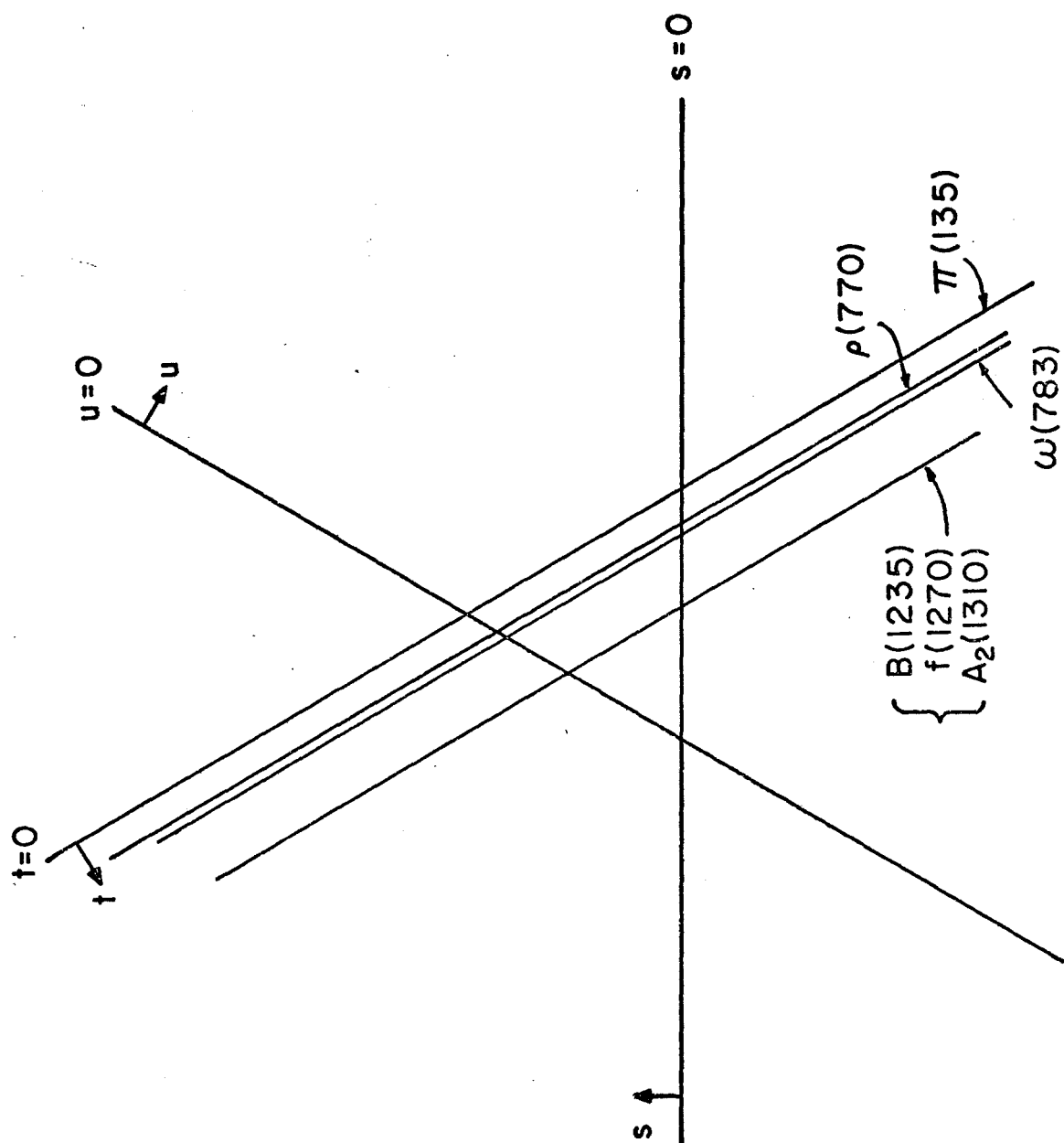
B. Regge Predictions of PP Polarizations. We begin by rewriting the equation for the polarization in terms of the definite parity amplitudes N_i of eqn.(28):

$$P = - \frac{\text{Im} [(N_0 - N_2) N_1^*]}{128\pi q^2 s \, d\sigma/dt} \quad (33)$$

As in πp scattering, the diffractive nature of the differential cross-sections leads us to take the diffractive contribution N_0 as the dominant part of the non-flip amplitude, and Regge contributions (ρ , A_2 , f , ω , ...) of the flip amplitude. Thus with $|N_0| \gg |N_2|$, and $|\text{Im } N_0| \gg |\text{Re } N_0|$ eqn. (33) simplifies to

$$P \approx -\text{Im} (N_0) \text{Re} (N_1) / (128\pi q^2 s \, d\sigma/dt) \quad (34)$$

Figure I-7. s-t-u diagram for pp showing the physical regions of the pp system and t channel poles.



while

$$N_1 \sim \sum \frac{\beta_R(t) (\xi_R + e^{-i\pi\alpha_R}) s^{\alpha_R}}{\sin \pi\alpha_R} \quad (35)$$

Now it is well established that the ρ - A_2 and ω - f pairs of resonances are weakly exchange degenerate (i.e. have the same α : see Figure I-3), so we can write¹⁴

$$\begin{aligned} N_1 &\sim \sum \xi_R \beta_R(t) (1 + \xi_R e^{-i\pi\alpha_R}) s^{\alpha_R} / \sin \pi\alpha_R \\ &= \sum_{\text{even } \xi} \beta_R (1 + e^{-i\pi\alpha_R}) s^{\alpha_R} / \sin \pi\alpha_R \\ &\quad - \sum_{\text{odd } \xi} \beta_R (1 - e^{-i\pi\alpha_R}) s^{\alpha_R} / \sin \pi\alpha_R \\ &= \sum_R (\beta_{\text{even}} - \beta_{\text{odd}}) s^{\alpha_R} / \sin \pi\alpha_R \\ &\quad + \sum_R (\beta_{\text{even}} + \beta_{\text{odd}}) e^{-i\pi\alpha_R} s^{\alpha_R} / \sin \pi\alpha_R \end{aligned} \quad (36)$$

But strong exchange degeneracy - the equality of residues - is on nearly as firm ground, eg as an explanation for the energy independence of $\sigma_T(K^+p)$ at low energies and as a means for understanding the lack of structure of the K^+p differential cross-sections,¹⁵ so we can take

$$\beta_{\text{even}} = -\beta_{\text{odd}}$$

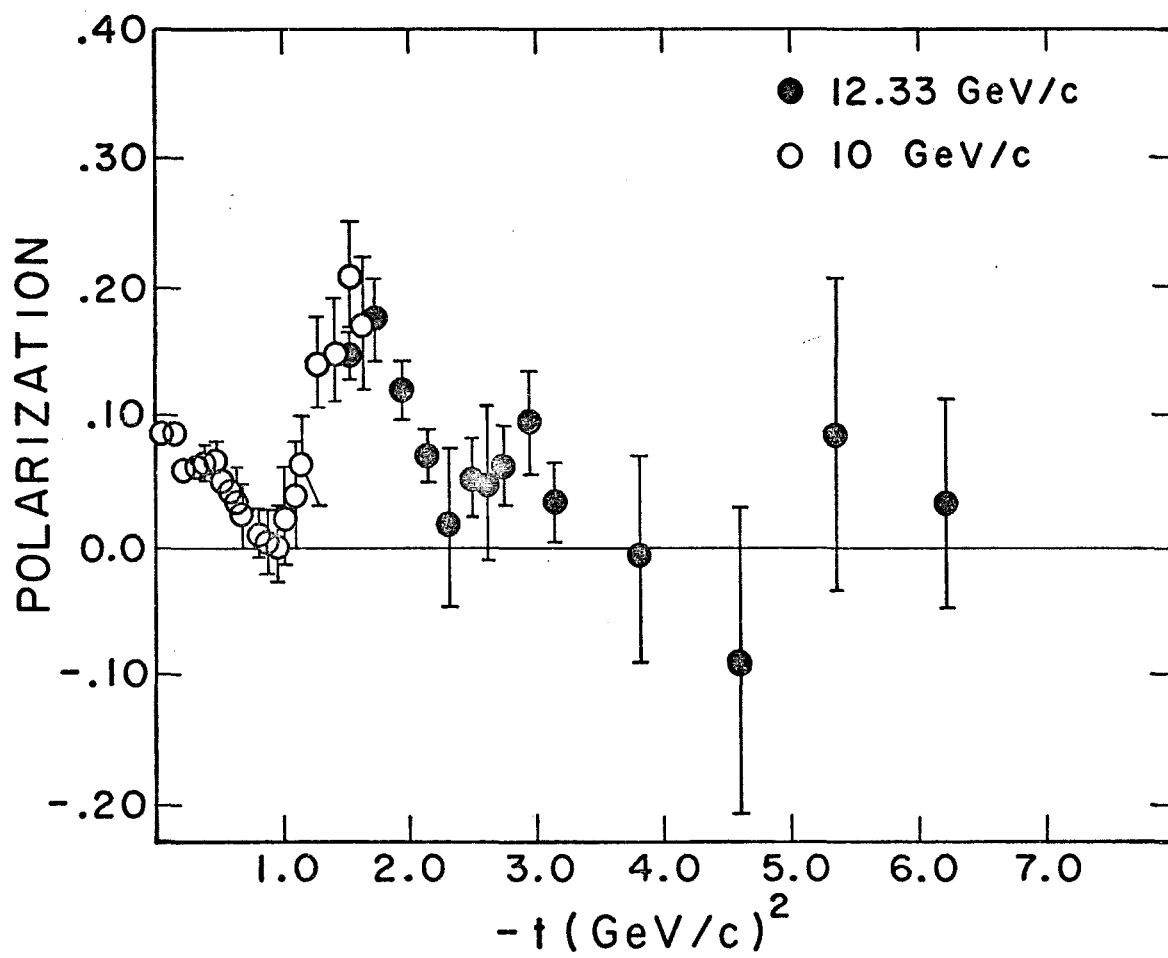
to obtain

$$\begin{aligned} N_1 &\sim 2 \sum \beta_R s^{\alpha_R} / \sin \pi\alpha_R \\ &= 2 \sum \beta'_R s^{\alpha_R} \end{aligned} \quad (37)$$

where we have extracted a factor of $\sin \pi \alpha_\rho$ from $\beta(t)$, since exchange degeneracy requires β to have zeros at each integer value of α . Thus we expect a nearly real N_1 component, slowly varying with t . Since the diffractive component is also expected to be smooth - it is approximately exponential in t - we obtain the standard Regge prediction of a smooth and slowly varying polarization. As we see in Figure I-8, this is a much poorer fit to the data than the analogous prediction in πp scattering. The data, far from being structureless, show a double zero at $t \sim -0.8 \text{ GeV}^2$, with indications of zeros¹⁶ at $t = -2$ and $t = -3.6 \text{ GeV}^2$. To improve our prediction, we might allow exchange degeneracy breaking, but this too has its problems; if we break exchange degeneracy in a natural way, we find either that the double zero is in the wrong place, or that pp and $\bar{p}p$ have mirror symmetric polarizations, contrary to experiment.¹⁴

No way has been found to generate the observed polarizations naturally within a pure pole model. As with the πp charge exchange polarizations, we are faced with introducing cuts.

Figure I-8. pp polarization data at 10 and 12.3 GeV.
Data from Ref. 16.



IV. Cuts

A. The Existence of Cuts. It has been known for some time that cuts must exist, essentially because it can be shown that fixed poles exist, and these must be "shielded" by cuts to preserve unitarity.¹⁷ For simplicity, consider spinless scattering from a spinless target, and suppose that near the point $\alpha=J$, the transition matrix can be written $T \sim R/(\alpha-J)$; then the unitarity equation

$$T - T^+ = i\rho(s) T^+ T \quad (38)$$

(with $\rho(s)$ containing kinematic factors) naively implies a single pole on the left hand side and a double pole on the right hand side which is nonsense; either R must be zero, or T must have a cut running through the point $\alpha=J$; i.e. Gribov-Pomeranchuk fixed poles at wrong signature nonsense zeros must be shielded by cuts.

Experimentally, the need for cuts is compelling. We have already seen that the appreciable polarization observed in πp charge exchange scattering requires either another trajectory, or else cuts; and that the structure observed in pp polarizations appears to be incompatible with an exchange degenerate pure pole model.

We discuss briefly two other effects which suggest the presence of cuts:¹⁸ the cross-over zero observed in πp and $K p$ elastic scattering, and the observation of sharp spikes at small t where dips are expected in the differential cross-

section, e.g. as in pion photoproduction.

The cross-over zero problem is essentially the observation that the differential cross-section for π^+p (or K^+p) and π^-p (K^-p) have different slopes and intercepts at small t , which leads us to an unexpected zero in the ρ amplitude. At $t=0$,

$$d\sigma/dt (\pi^-p) > d\sigma/dt (\pi^+p) \quad (39)$$

while the logarithmic derivatives satisfy

$$d/dt [\ln d\sigma/dt (\pi^+p)] < d/dt [\ln d\sigma/dt (\pi^-p)] \quad (40)$$

The two differential cross-sections cross at $t=-0.15 \text{ GeV}^2$.

Writing

$$d\sigma/dt (\pi^\pm p) = |(P + f \mp \rho)_{++}|^2 + |(P + f \mp \rho)_{-+}|^2 \quad (41)$$

we see that any difference is a consequence of the ρ amplitude changing sign. Making the same assumptions of non-flip Pomeron and flip ρ dominance as before, we obtain

$$d\sigma/dt (\pi^+p) - d\sigma/dt (\pi^-p) \sim \text{Im } \rho_{++} \quad (42)$$

and consequently the imaginary part of the ρ non-flip amplitude must have a zero at $t=-0.15$. Similar results hold in Kp and pp elastic scattering, with the zero in roughly the same place. It can be seen from eqn. (11a) that a priori there is no reason to expect the ρ amplitude to have this zero, so if the amplitude is to have it we must put it in by hand. However this has problems as well: e.g. in $\pi^-p \rightarrow \omega n$ scattering, with ρ exchange, the zero doesn't appear, so the residue doesn't

factorize. Also, a zero in the residue would lead to coincident zeros in the real and imaginary parts of the amplitude, which does not seem to be the case. Again cuts seem to be the most promising way out of the quandary.

We finally consider the problem of peaks in reactions where dips are expected.¹⁹ Angular momentum constraints require that an s-channel helicity amplitude with definite parity in the t channel (i.e., a t channel Regge pole) vanish as $t \rightarrow 0$ as

$$T_{\lambda,\lambda}(s,t) \sim (-t)^{m/2} \quad (43)$$

with m the sum of the helicity flips at each vertex. On the other hand, the general s channel helicity amplitude need only vanish as

$$T_{\lambda,\lambda}(s,t) \sim (-t)^{n/2} \quad (44)$$

with n the net helicity flip. Thus from eqn. (43) all definite parity amplitudes with flips at either vertex should vanish as $t \rightarrow 0$, while from eqn. (44) the general amplitude can remain non-zero as long as the net flip is zero. Consider the reaction $\gamma p \rightarrow \pi^+ n$, in which the π trajectory is expected to dominate. According to eqn. (43) the differential cross-section should vanish as $t \rightarrow 0$, while experimentally it is found to have a peak of width $\Delta t \sim m_\pi^2$. In the absence of a natural parity trajectory with which the pion can conspire, it is generally assumed that the peak is caused by a cut, since

cuts are not expected to have definite parity, and hence are not constrained by eqn. (43). The differential cross-section peak can be understood quite well as an absorptive (i.e. cut) effect.

B. Models for Regge Cuts. Unfortunately, cuts are not nearly as well understood as poles. Theoretically, the various models used to understand pole behavior, such as potential scattering, are much harder to apply to cuts. Experimentally, the main tests of cut behavior, factorization and $\ln s$ behavior, are much less conclusive - $\ln s$ is small, even at ISR energies, and sums of poles will not factor either. And some models suggest that cuts may approximately factor anyway.

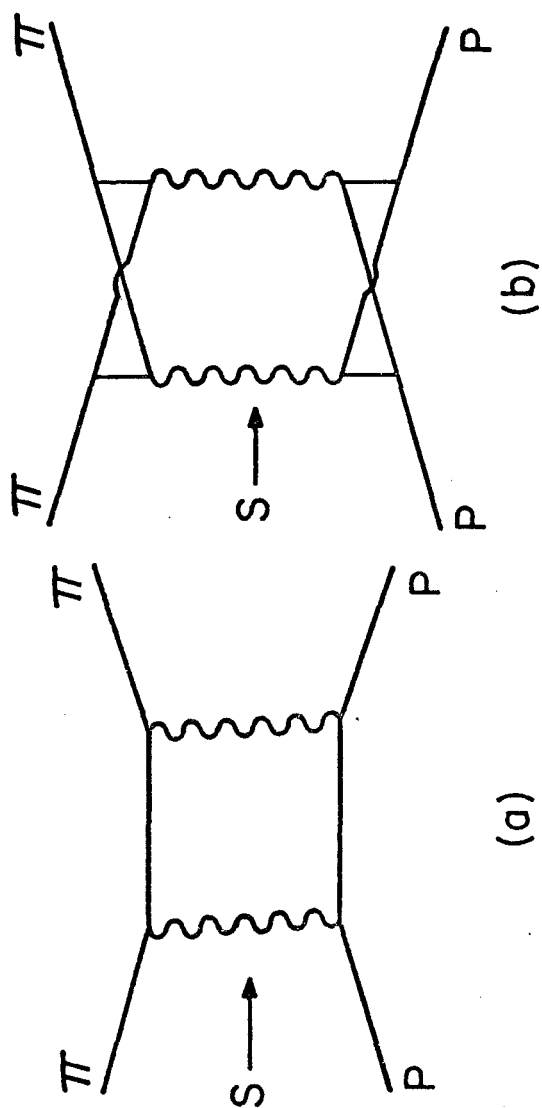
In the absence of any generally accepted theory, two related models have become popular for fitting the data within a Regge pole framework: the eikonal model and the absorption model. Strictly speaking, the absorption model is a particular version of the eikonal model, so we shall develop the more general form. In chapter IV, we will specialize to the absorption model and fit the data from this experiment to the model of the Michigan school.

Before embarking on what may strike the reader as a rather tedious exercise, the derivation of the eikonal model, we comment briefly on the motivation of the model. It should be clear that the Regge pure pole models have been remarkably successful, considering how generally based their foundations;

any model seeking to improve upon the pole models must retain many of the ideas of those models. The correct prediction of the energy dependence of the πp charge exchange differential cross-section, and the predictions of the mirror symmetry and the energy dependence of the πp elastic polarizations are by no means trivial successes. The eikonal model, as applied to high energy physics, is an attempt to modify the Regge pole amplitudes - renormalize them, in a sense - by including absorptive rescattering effects which tend to reduce the amplitudes at small impact parameters. If one analyzes the failures of the pure pole models, one finds generally that the pole models have been least successful when a dominant non-diffractive amplitude is large at small impact parameters, so one might expect absorption corrections to produce amplitudes closer to the actual physics amplitudes.²⁰

It is perhaps worth noting here that the eikonal model is not truly a cut model; as we shall see shortly, it involves diagrams of the sort displayed in Figure I-9, i.e. planar diagrams. It can be shown that such planar diagrams do not lead to cuts (the simplest diagram leading to a cut is shown in Fig. (9b)). Nonetheless, such planar diagrams can be shown to have the same energy dependence as diagrams leading to cuts,²¹ and in the spirit of making corrections (needed both experimentally and theoretically) to the "bare" pole terms, the eikonal model is generally regarded as a reasonable way to parametrize these "renormalizing" corrections.

Figure I-9. a) diagram for the exchange of two Regge trajectories which does not lead to a cut.
b) Mandelstam's diagram, which leads to a cut.



C. The Eikonal/Absorption Model. We begin by deriving the eikonal model from the partial wave expansion of the transition amplitude. Specializing to the helicity non-flip amplitude, we obtain the diffractive peak characteristic of elastic scattering. Obviously, calculating polarizations with only non-flip amplitudes would be a thankless task, so we discuss how cut contributions to flip amplitudes are parametrized. After noting briefly the form and energy dependence of the cut amplitudes, we mention various parametrizations of diffractive scattering—in Regge language, the Pomeron.

The partial wave expansion for the transition amplitude is

$$T_{\lambda',\lambda}(s,t) = 16\pi \sum_{J=M}^{\infty} (2J+1) T_{\lambda',\lambda}^J(s) d_{\lambda',\lambda}^J(Z), \quad M=\max(|\lambda|, |\lambda'|) \quad (45)$$

At high energies and small angles, where $s \gg t$, we can make the usual substitutions

$$d_{\lambda',\lambda}^J(z) \rightarrow J_n((J+\frac{1}{2})\theta)$$

where $n=|\lambda'-\lambda|$ is the net helicity in the s channel,

$$(J+\frac{1}{2}) \hbar \rightarrow qb$$

$$q\theta \approx \sqrt{-t} \equiv \tau$$

$$\Sigma(1) \rightarrow \Sigma(\hbar \Delta J) \rightarrow \int qdb$$

$$T_{\lambda, \lambda}^J(s) \rightarrow T_n(s, b)$$

to get the impact parameter representation of the transition amplitude

$$T_{\lambda, \lambda}(s, t) = 32\pi q^2 \int b db T_n(s, b) J_n(b\tau) \quad (46)$$

We can express T^J in unitary form as

$$T^J(s) = \frac{e^{2i\delta_n^J(s)} - 1}{2i\rho(s)} \quad (47)$$

where $\delta_n^J(s)$ is the usual phase shift for scattering in the J^{th} partial wave with net helicity flip n , and define the eikonal $\chi(b)$ as

$$\chi_n(b) = 2\delta_n^J(s) \quad (48)$$

where we have suppressed the dependence on s to simplify the notation. This assumes of course that δ can be continued analytically between integer values of J . At high energies, the factor $\rho(s) \rightarrow 1$; letting

$$T_n^J(s) \rightarrow T_n(s, b) = \frac{e^{i\chi_n(b)} - 1}{2i} \quad (49)$$

we obtain the small angle form of the eikonal approximation,

$$T_{\lambda, \lambda}(s, t) = -16\pi i q^2 \int b db (e^{i\chi_n} - 1) J_n(b\tau). \quad (50)$$

At the risk of breaking the continuity of the section, we digress to obtain the important result that the general form of the diffractive peak can be obtained using the eikonal

approximation with very simple ideas about the form of the eikonal. We understand diffractive scattering in terms of non-relativistic potential scattering, in which a wave passing through an absorptive potential undergoes small angle scattering; thus, we choose for the eikonal a function which incorporates the idea of scattering from a localized imaginary potential:

$$\chi(b) = i g e^{-b^2/R^2} \quad (51)$$

We proceed by expanding eqn. (50) in a power series in χ :

$$\begin{aligned} T_{\lambda' \lambda}(s, t) &= -16\pi i q^2 \sum_{k=1}^{\infty} \int b db J_n(b\tau) (i\chi_n)^k / k! \\ &= 16\pi \sum T_{\lambda' \lambda}^{(k)} \end{aligned} \quad (52)$$

Specializing to the non-flip amplitude with $n=0$ we obtain

$$T_{00}(s, t) = -16\pi i q^2 \sum s^k / k! \int b db J_0(b\tau) e^{-kb^2/R^2} \quad (53)$$

These integrals can be evaluated using the relation

$$\int_0^{\infty} -a^2 z^2 J_m(cz) z^{1+m} dz = \frac{c^m}{(2a^2)^{1+m}} e^{-c^2/4a^2}$$

with the result

$$T_{00}(s, t) = 16\pi \sum T_{00}^{(k)} \quad (54)$$

where

$$T_{00}^k(s, t) = -iq^2 (-s)^k / k! R^2 / 2k e^{B_k \tau / 2} \quad (55)$$

with

$$B_k = R^2/2k \quad (56)$$

In particular, the first term is

$$T_{00}^{(1)}(s,t) = -iq^2 s R^2/2 e^{-R^2 t/4} \quad (57)$$

and contributes to the differential cross-section the term

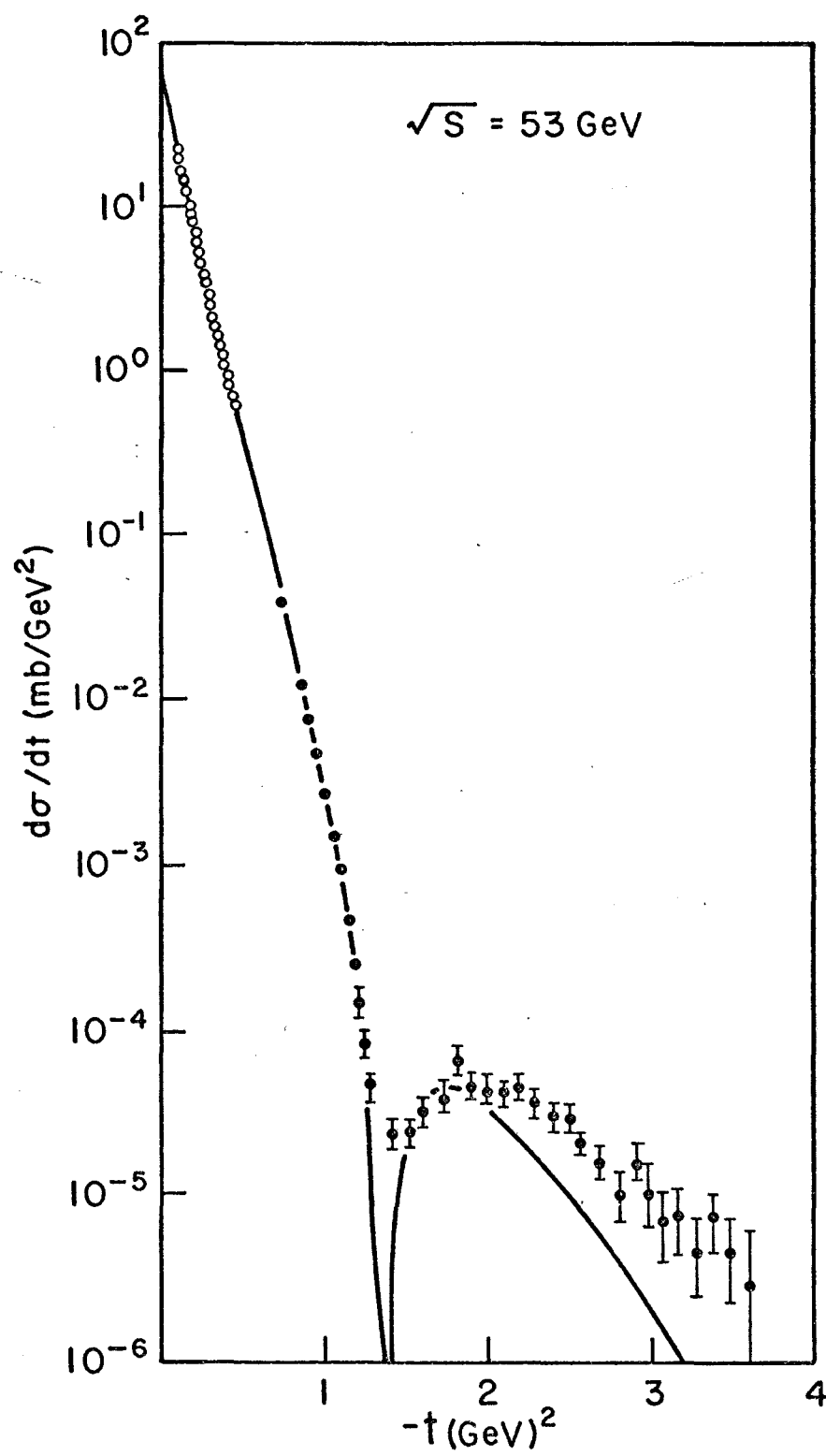
$$\begin{aligned} d\sigma/dt &\approx \frac{\pi |T_{00}^{(1)}|^2}{q^2 s} \\ &\approx \pi g^2 R^4/8 e^{-R^2 t/2} \end{aligned} \quad (58)$$

If we take the logarithmic slope to be that of pp elastic scattering, $B \approx 10 \text{ GeV}^{-2}$, we find

$$R \approx 0.9 \text{ fermi},$$

a result which accords remarkably well with our intuitive ideas about the size of hadrons. Note also that the amplitude, from eqn. (54) and (55), is the sum of exponential terms of decreasing slope, so that at sufficiently large t one would expect to see a break in the differential cross-section. While this particular model is too naive to be taken very seriously, it is nonetheless similar to more reasonable models, e.g. of Chou and Yang.²² As an example of the success this type of model has had in explaining purely diffractive scattering, we show in Figure I-10 a fit to the ISR pp differential cross-section data obtained by Byers.²³

Figure I-10. Fit to the pp differential cross-section
 $\sqrt{s} = 53$ GeV. From Ref. 23.



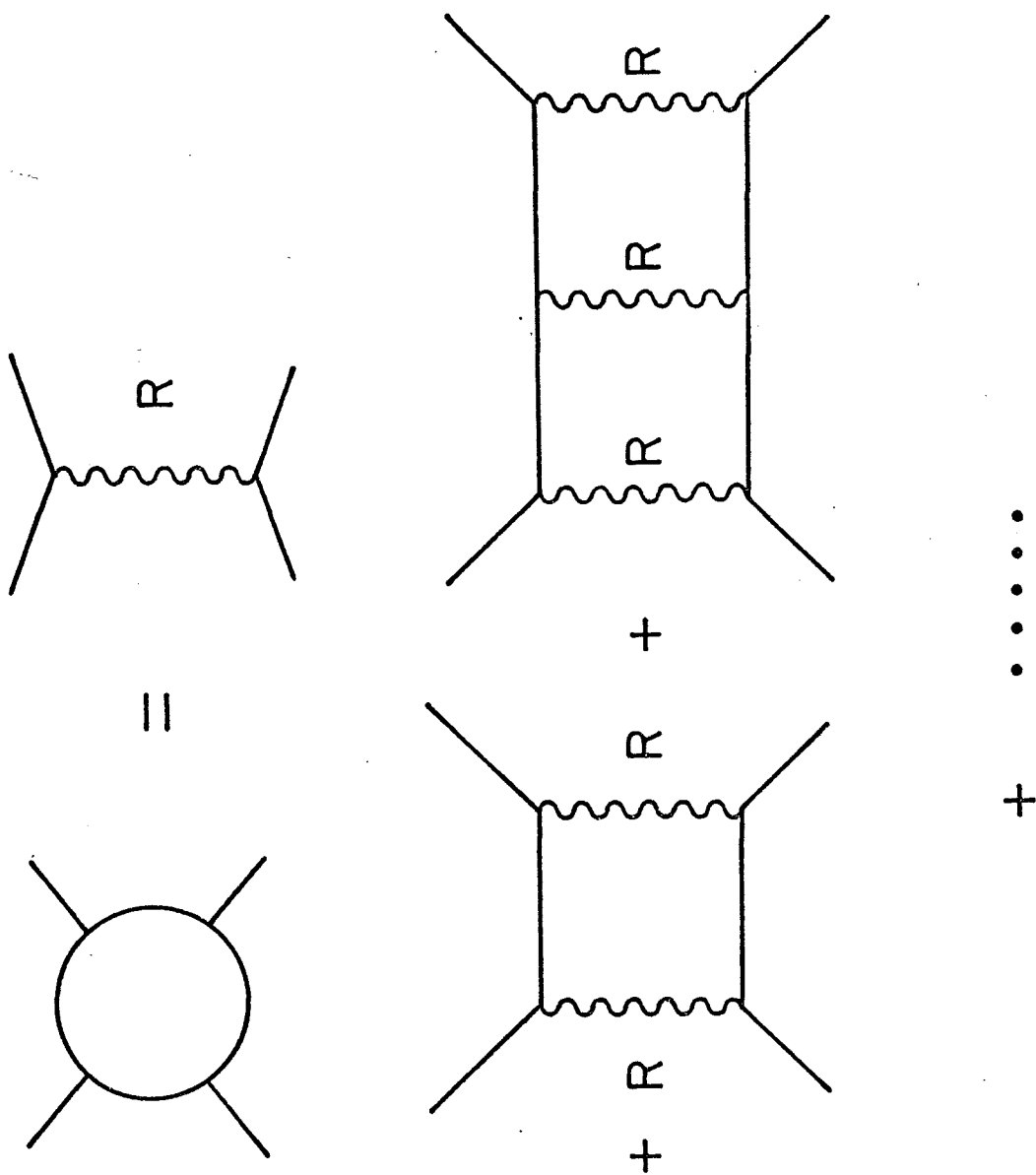
We now wish to consider the interpretation of the eikonal expansion, eqn. (50), in order to choose a form for the eikonal, $\chi(b)$. In nonrelativistic potential scattering, the eikonal expansion can be thought of as a model in which an incident wave undergoes multiple small angle scattering as it passes through the potential. The analogous concept in relativistic scattering is the multiple exchange of quanta characteristic of the interaction. Thus we consider succeeding terms in eqn. (52) as corresponding to increasing numbers of exchanged quanta, which in strong interaction physics we may reasonably take as trajectories. Designating a quantum by R , the expansion of eqn. (52) corresponds to an amplitude

$$T \sim R + (R \times R) + (R \times R \times R) + \dots$$

where the χ term corresponds to single R exchange the χ^2 term corresponds to double R exchange (the cut $R \times R$), etc., as in Figure I-11. Thus the choice of eqn. (49) for the transition amplitude T results in the exchange of quanta of type R . In strong interaction physics it is always the case that several types of "quanta", say R_1, R_2, \dots , can be exchanged; we can put this into our formalism by modifying eqn. (49) via the DWBA:

$$T_n^{R_1 R_2}(s, b) = \frac{(e^{i\chi} - 1)}{2i} e^{i\chi_1} e^{i\chi_2} \dots \quad (59)$$

Figure I-11. Diagrams corresponding to the exchange of two or more Regge trajectories.



and obtain an expansion analogous to eqn. (52). In this case, the exchange of m_1 particles R_1 , m_2 particles R_2, \dots , is written in the form

$$T_{\lambda', \lambda}^{m_1 m_2 \dots}(s, t) = -16\pi i q \int b db J_n(b\tau) \frac{(i\chi_{n_1}^{R_1})^{m_1}}{m_1!} \frac{(i\chi_{n_2}^{R_2})^{m_2}}{m_2!} \dots \quad (60)$$

We have now gone through all the algebra needed to obtain the rescattering corrections to our amplitudes: given the bare amplitude χ_R in impact parameter space, we pick all of the amplitudes $\chi_{R_1}, \chi_{R_2}, \dots$, which can give rescattering corrections and write

$$T_{\lambda', \lambda}^{\text{abs}}(s, t) = -16\pi i q^2 \int b db J_n(b\tau) (e^{i\chi_{n-1}^R}) e^{i\chi_{n_1}^{R_1}} \dots \quad (61)$$

But before we can calculate absorbed amplitudes we must choose a form for the "bare" eikonal χ . Consider the lowest term of the expansion of eqn. (61):

$$T_{\lambda', \lambda}^{(1)}(s, t) = -16\pi q^2 \int b db J_n(b\tau) \chi_n^R(b) \quad (62)$$

We see immediately that T_n and χ_n are Hankel transforms, so we can write T_n as the t space "bare" amplitude corresponding to the "bare" amplitude in impact parameter space:

$$\chi_n^R(b) = 1/16\pi q^2 \int b db J_n(b\tau) T_{\lambda', \lambda}^{(1)}(s, t) \quad (63)$$

In view of our suggestion that Regge models were quite successful, but needed modifications to take into account absorption corrections, it is natural to identify the bare t -space amplitude on the right hand side of eqn. (63) with

the Regge pole amplitude:

$$T_{\lambda'\lambda}^{(1)}(s,t) = \tau^n \gamma_R(t) (\xi_R + e^{-i\pi\alpha_R}) \left(\frac{s}{s_0}\right)^{\alpha_R} \quad (64)$$

and we obtain $\chi_R(b)$ by transforming eqn. (64) to b space.

After obtaining χ_{R_1} , χ_{R_2} , ..., in analogous fashion, we obtain the absorbed amplitude by carrying out the integral in eqn. (61).

We wish to consider the behavior of the $R_1 \times R_2$ term as an example. Following Collins,²¹ we take a linear trajectory

$$\alpha(t) = \alpha_0 + \alpha' t$$

and an exponential residue

$$\gamma(t) = G \exp(at)$$

and obtain for the pole term

$$T_{nR}^{(1)}(s,t) = -x G \tau^n e^{-i\pi\alpha_0} \left(\frac{s}{s_0}\right)^{\alpha_0} e^{ct} \quad (65)$$

where $x=1/-i$ for $\xi=+/-$, and

$$c = a + \alpha' (\ln(s/s_0) - i\pi/2) \quad (66)$$

Substituting into eqn. (63), we obtain for the eikonal (or equivalently, the T amplitude in b space)

$$\chi_n^R(b) = \frac{-xG}{8\pi s} (s/s_0)^\alpha e^{-i\pi\alpha_0/2} \left(\frac{b}{2c}\right)^n e^{-b^2/4c} \quad (67)$$

Note that all amplitudes are Gaussian in b for large b , and that the eikonal vanishes as a power of b as $b \rightarrow 0$, except for

the non-flip amplitudes. This last is quite important, since it means that the absorption will depend only on the helicity of the amplitude - different helicity amplitudes will be absorbed differently, with non-flip amplitudes absorbed the most, single flip amplitudes somewhat less, and so on.

To calculate the cut amplitude, we substitute eqn. (67) back into eqn. (60). Specializing again to $n=0$, we obtain for the $R_1 \times R_2$ cut

$$T_{n=0}^{R_1 R_2}(s, t) = i x_1 x_2 G_1 G_2 \left(\frac{s}{s_0}\right)^{\alpha_{01} + \alpha_{02}} e^{\frac{i\pi}{2}(\alpha_{01} + \alpha_{02})} e^{\tilde{c}_1 \tilde{c}_2 t / (c_1 + c_2)} \quad (68)$$

so that the cut has a flatter t dependence than the pole. For $\alpha' \ln(s/s_0) \gg a$,

$$c_1 c_2 / (c_1 + c_2) \rightarrow \frac{\alpha'_1 \alpha'_2}{\alpha'_1 + \alpha'_2} \left(\log \left(\frac{s}{s_0} \right) - \frac{i\pi}{2} \right) \quad (69)$$

so

$$\begin{aligned} T_{n=0}^{R_1 R_2} &\rightarrow x_1 x_2 G_1 G_2 \left(\frac{s}{s_0}\right)^{\alpha_c(t)} e^{-i\pi \alpha_c(t)/2} / \left\{ a_1 + a_2 + (\alpha'_1 + \alpha'_2) \left(\ln \left(\frac{s}{s_0} \right) - \frac{i\pi}{2} \right) \right\} \\ &\rightarrow s^{\alpha_c(t) / \ln s} \end{aligned}$$

where

$$\alpha_c(t) = \alpha_{01} + \alpha_{02} - 1 + \frac{\alpha'_1 \alpha'_2 t}{\alpha'_1 + \alpha'_2} \quad (71)$$

Note the $\ln s$ modification of the power law behavior, to which we have already referred.

We have neglected one point in the above discussion, the choice of the form for the diffractive amplitude to be used

for rescattering. Since in practice only the diffractive eikonal is used in eqn. (59) to compute the absorption correction, this is a serious omission which we now correct. Essentially all workers have regarded the diffractive ("Pomeron") amplitude as different from a Regge pole term, and have parametrized its t dependence in various ways, e.g. Chou and Yang²² took the Pomeron to be proportional to the nucleon electromagnetic form factor:

$$P \sim (1 - t)^{-4}$$

while Capella et al.²⁴ considered the sum of two exponentials, and Byers²³ and Bourreley et al.²⁵ used a modified electromagnetic form factor. The absorption model of Kane et al.¹⁹ uses a Pomeron

$$P \sim e^{B_c t} J_1(R_c \tau) / \tau + e^{B_e t} J_0(R_0 \tau)$$

to which is added the f amplitude and a term corresponding to intermediate inelastic states, for calculating rescattering corrections. The only a priori rules are that the diffractive amplitude should have a large negative imaginary part and that the square of its modulus should give the corresponding elastic differential cross-section to first order, at least for small t .

Having chosen a form for the diffractive amplitude, one then uses eqn. (63) to get the eikonal, absorbs with the elastic eikonal, and obtains the t space amplitude

$$T_{\lambda'\lambda}^{\text{abs}}(s,t) = -16\pi i q^2 \int b db J_n(b\tau) i\chi_n^R(b) \exp(i\chi_0^{\epsilon 1}(b)) \quad (72)$$

To see quickly the effect of absorption on amplitudes in b space, consider a non-flip term, which according to eqn. (67) is a Gaussian in b peaked at the origin. We can approximate eqn. (72) as

$$T_{\lambda'\lambda}^{\text{abs}}(s,t) = 16\pi q^2 \int b db J_n(b\tau) \chi_n^R(b) [1 - i\chi_0^{\epsilon 1}(b)] \quad (73)$$

which in b space is

$$\chi_n^{\text{abs}}(b) \approx \chi_n^R(b) \{1 - i\chi_0^{\epsilon 1}(b)\} \quad (74)$$

If we now take the diffractive elastic amplitude as a Gaussian in b , the absorbed amplitude will be reduced at low impact parameter as in Figure I-12a. As a result the non-flip amplitude after absorption is largest at the periphery, $b \sim 1$ fm. The flip amplitudes are already peripheral because of the b^n factor in eqn. (67) and are less affected by absorption, as in Figure I-12b. Approximating the b dependence of the absorbed amplitude by a δ function at $b \approx R = 1$ fm,

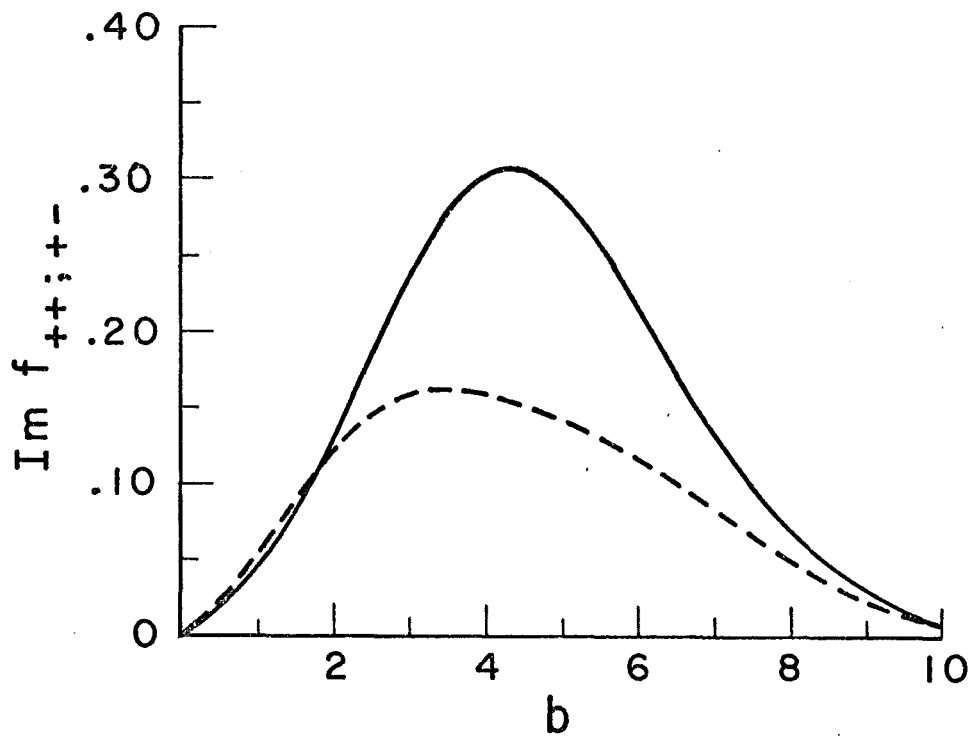
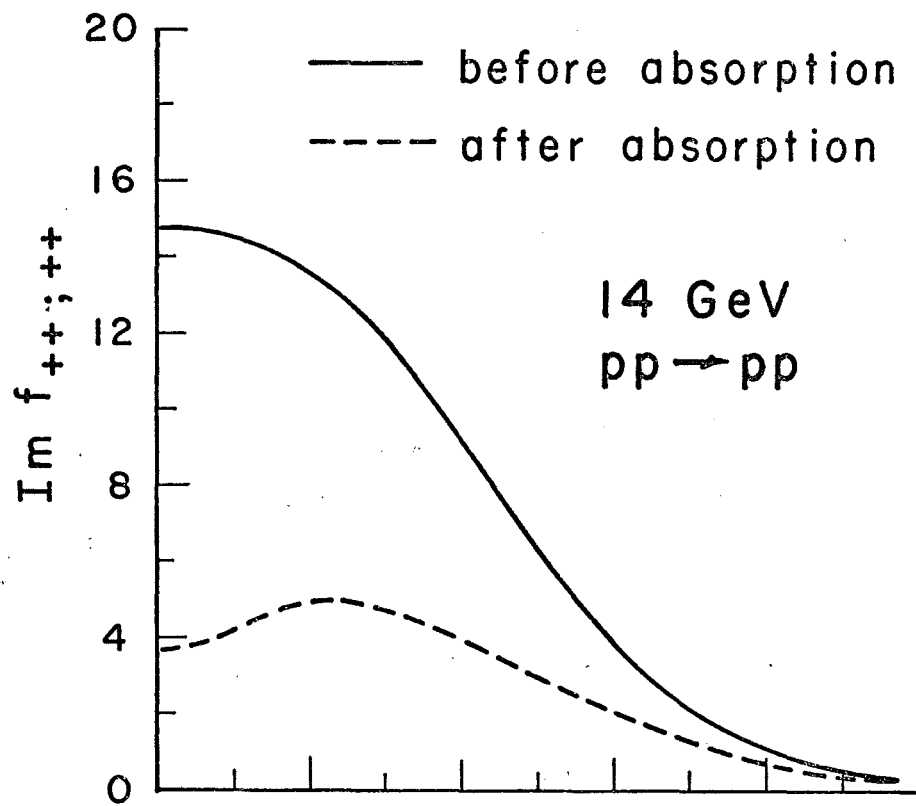
$$\chi_n^{\text{abs}}(b) \sim \frac{-xG}{8\pi s} e^{-i\pi\alpha/2} (s/s_0)^\alpha \delta(b-R)/R \quad (75)$$

we obtain

$$T_n^{\text{abs}}(s,t) = -xG \exp(-i\pi\alpha/2) (s/s_0)^\alpha J_n(R\tau) \quad (76)$$

(where we have ignored phase and power behavior differences between α_R and α_c , and have dropped the $\ln s$ term). For $n=0$

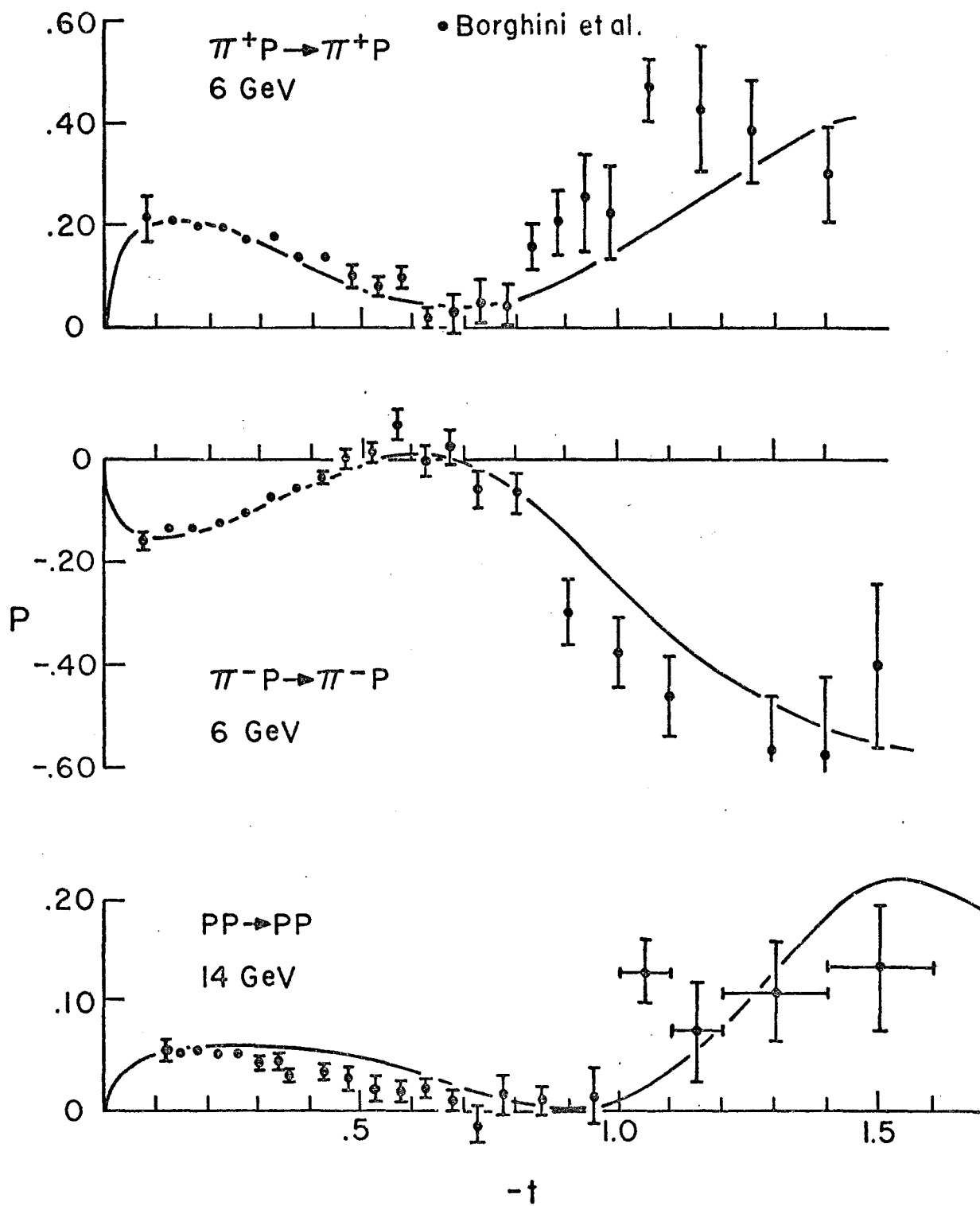
Figure I-12. a) Non-flip Regge amplitude before and after absorption.
b) Flip Regge amplitude before and after absorption.



and $n=1$ the first zeros appear in J_n at $t=-0.2$ and -0.55 GeV^2 , values which correspond to the amplitude zeros noted earlier in this section. The motivation for building eikonal/absorption models is the expectation that when absorptive rescattering effects are taken into account, the various zeros which give pure pole models such difficulties will appear naturally as geometric effects. And since the amplitudes affected most by absorption are those which give the pole models trouble, it is not too unreasonable to hope that the absorption model will improve upon the less successful predictions of the pole models without ruining the more successful ones.

As an example of the power of the absorption model, we present fits to the πp polarizations at 6 GeV and to the pp polarization at 14 GeV in Figure I-13. We will find in chapter IV that the Michigan absorption model¹⁹ (among others) does an impressive job of correlating data from a very large number of reactions in a systematic way. One is led to the conclusion that, whatever the formal status of eikonal/absorption models, they are so successful in describing the data that the ideas which underlie them - complex angular momenta leading to Regge poles, and absorptive rescattering leading to cut singularities - must play an important part in the interaction.

Figure I-13. a) A fit to the 6 GeV πp polarization data
obtained with the model of Ref. 19.
b) A fit to the 14 GeV pp polarization data
obtained with the model of Ref. 19.



References for Chapter I.

1. Martin, A.D., and T.D. Martin, Elementary Particle Theory, North Holland Publ. Col. 1970.
Barger, V., and D. Cline, Phenomenological Theories of High Energy Scattering, Benjamin 1969.
2. We follow the notation of M. Perl in High Energy Hadron Physics, Wiley 1975.
3. See Martin and Spearman, *ibid.*
4. See Barger and Cline, *ibid.*, or Queen, N.M., and G. Violini, Dispersion Theory and High Energy Physics, Wiley (1975).
5. Barnes, A.V., et al., Phys. Rev. Lett. 37, 76 (1976).
6. Hohler, G., Baake, J., Schlaile, H., and Sondregger, P., Phys. Lett. 20, 79 (1966).
7. Hill, D., et al., Phys. Rev. Lett. 30, 239 (1973).
Bonamy, P., et al., Nucl. Phys. B52, 392 (1973).
8. Borghini, M., et al., Phys. Lett. 31B, 405 (1970).
Borghini, M., et al., Phys. Lett. 36B, 493 (1971).
9. van Rossum, L., Book of the AIP Conference on Polarized Beams and Targets, 134 (1976).
10. Irving, A.C., Nucl. Phys. B101, 263 (1975).
Pumplin, J., and G. Kane, Phys. Rev. D11, 1183 (1975).
11. Goldberger, M.L., Grisaru, M.T., MacDowell, S.W., and Wong, D.Y., Phys. Rev. 120, 2250 (1960).
12. Halzen, F., and G.H. Thomas, Phys. Rev. D10, 344 (1974).
13. Martin and Spearman, *ibid.*
14. This argument is sketched by Chiu, S., and Hendry, A.W., Phys. Rev. D6, 190 (1972).

15. See e.g. Perl, *ibid*, or Hartley, B.J. and G.L, Kane, Nucl. Phys. B57, 157 (1973).
16. Borghini, M., et al., Phys. Lett. 36B, 501 (1971).
Abshire, G.W., et al., Phys. Rev. Lett. 32, 1261 (1974).
Bryant, G.W., et al., Phys. Rev. D13, 1 (1976).
17. Collins, P.D.B., Phys. Rept. 1, 103 (1971).
18. Collins, P.D.B., Regge Theory and High Energy Physics, Cambridge, 1977.
19. Kane, G., and A. Seidl, Rev. Mod. Phys. 48, 309 (1976).
20. Kane and Seidl, *ibid*.
21. Collins, P.D.B., Regge Theory and High Energy Physics, Cambridge 1977.
22. Chou, T.T., and C.N. Yang, Phys. Rev. 170, 1591 (1968).
Chou, T.T., and C.N. Yang, Phys. Rev. Lett. 20, 1213 (1968).
23. Byers, N., Lecture delivered at XIth International School of Subnuclear Physics, Erice, Sicily (1973).
24. Capalla, A., J. Kaplan, A. Krzywicki, and D. Schiff, Nuovo Cimento 63A, 141 (1969).
25. Bourrely, C., J. Soffer, and D. Wray, Nucl. Phys. B89, 32 (1975).
Gourrely, C., J. Soffer, and D. Wray, Nucl. Phys. B91, 33 (1975).
Bourrely, C., J. Soffer, and A. Martin, Nucl. Phys. B117, 95 (1976).
Bourrely, C., A. Martin, J. Soffer, and D. Wray, J. Phys. G. 3, 295 (1977).

THE EXPERIMENTAL APPARATUS

I. Introduction

Several considerations entered into the design of the detector. By far the most important was the recognition that the small differential cross-section for $-t > 1 \text{ (GeV/c)}^2$ implied an intense beam was necessary to measure the polarization in this t region. This immediately imposed three restrictions on the detector. First, the species of each incident beam particle could not be determined. This problem was solved by placing the Cerenkov counters downstream of the target and determining only the species of scattered particles. Second, neither proportional chambers nor scintillator hodoscopes are capable of sustaining fluxes on the order of 10^7 particles per pulse (ppp) without saturating. Thus there can be no measurement of each beam particle's trajectory. Of course the same comment applies to outgoing beam particles. Since quasi-elastic events - reactions in which an incident particle scatters from bound protons - form the main background, and since the resolution of these events from elastic events depends on knowing the incident particle's angle to $\pm 20 \text{ MeV/c}$ of transverse momentum, the angular divergence of the beam must be maintained within an appropriately small envelope. Finally, as noted above, beam flux and stability cannot be monitored directly by scintillators or proportional chambers, and in the intensity range below 10^8 ppp, ion chambers are not especially reliable. Thus in this experiment normalization of the data is possible only after

correlation of several indirect monitors of beam flux.

A less direct consequence of the high incident flux was the potentially high trigger rate associated with inelastic events. This was demonstrated in a set of test runs taken without pole tip veto counters: relative to the fraction of elastic and quasi-elastic ("reconstructable") events in normal runs (i.e., runs with the veto counters active) the fraction of unreconstructable, presumably multi-particle final state, events was dramatically enhanced. To avoid extended dead time associated with relatively slow devices, such as spark chambers firing on these inelastic events and limiting the live time for elastic events, the system was designed around intrinsically fast (40 ns) measuring devices, planes of multi-wire proportional chambers (PWC's). In addition, the logic was designed as a multi-level spatially dispersed coincidence circuit capable of resetting, when the stringent coincidence requirements were not met, without intervention from an on-line computer. Finally, perhaps the most interesting aspect of the detector was the use of switchable 'matrix' coincidence circuits operating on pulses from pairs of proportional chambers. With these matrices, coincidences between regions within chambers as small as 8 wires could either be required or entirely removed from the circuit on-line.

As a consequence of the high laboratory momentum of the beam, and resultant small scattering angles on the forward arm, the linear scale of the apparatus was considerably larger than

that of older laboratories. While the calculation of kinematic quantities made possible by a measurement of the momentum and projected angles of the recoil proton suffices to define the kinematics of elastic events, in practice inelastic backgrounds for a single arm spectrometer, especially at these energies and for a polarized target, are large. Consequently the apparatus for this experiment was a double arm spectrometer; the correlation of the forward arm angle measurement with the recoil arm kinematics allowed the rejection of most multiparticle final states in the trigger. Quasi-elastic, elastic, and inelastic events were present in roughly comparable proportions (to about a factor of 2) in the final trigger.

II. The Detector

The detector, shown schematically in Figure II-1, is a double arm spectrometer with roughly uniform acceptance (see Figure II-2) over a range $.25 < -t < 1.75 \text{ GeV}^2$ within a ϕ bite of ± 10 degrees. The momentum, projected scattering angle, and ascension angles are measured on each arm by a superconducting analysis magnet between two pair of PWC's. Note that, as both momenta and both scattering angles can be constructed, the detector in principle allows a 4C fit to the hypothesis of elastic scattering for each event. Experience with polarized target experiments has indicated that the reconstruction of the interaction point is useful in reducing the level of background. In this experiment, the recoil momentum measurement will be accurate only if the transverse displacement of the interaction point is known, allowing compensation for energy loss. At these energies, the forward particle undergoes negligible transverse displacement in the polarized target field, so straightforward ray tracing from WS1X and WS2X gives the desired transverse displacement to $\pm 2\text{mm}$. Similarly, ray tracing from WR1X and WR2X through a hard edge field gives the longitudinal component to $\pm 2\text{mm}$.

The fact that the detector had no active components in the beam has already been discussed at length in the Introduction to this chapter. In addition to the consequent absence of information regarding the incident particle's trajectory, this implies that there could be no veto on an unscattered beam particle. While this is different from many experiments,

Figure II-1. Schematic of the apparatus.

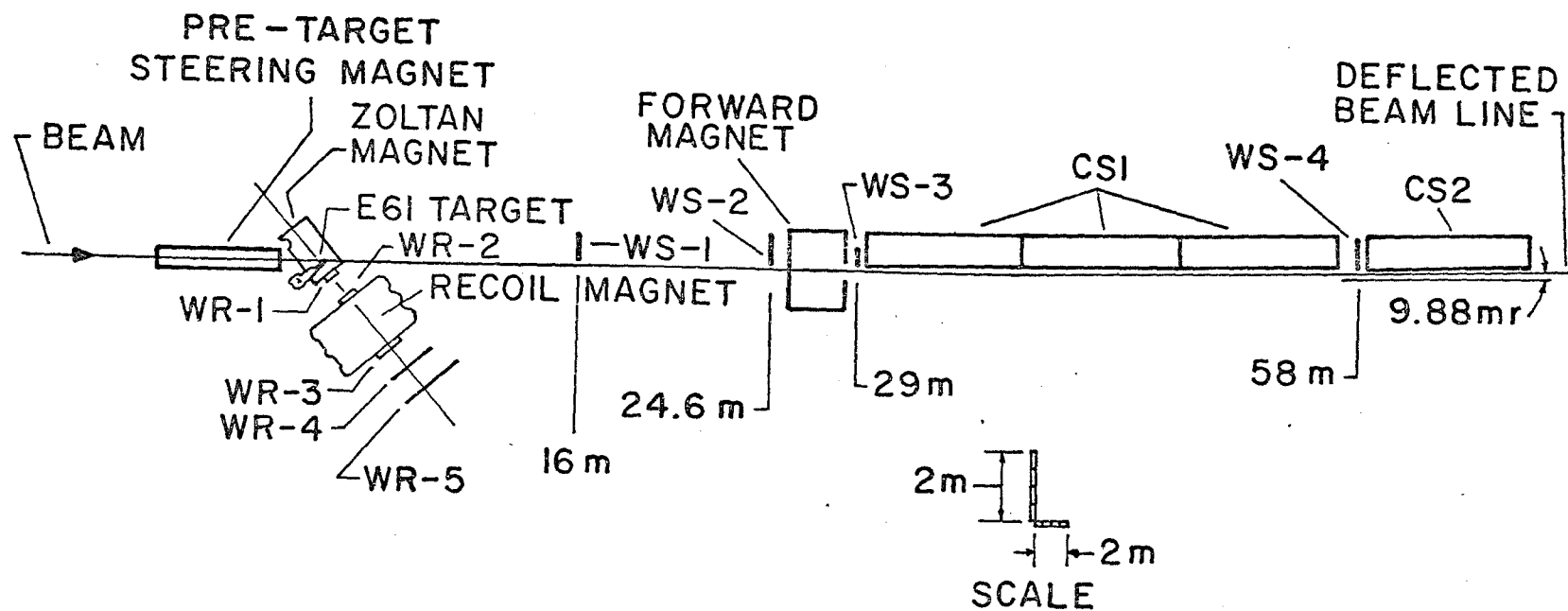
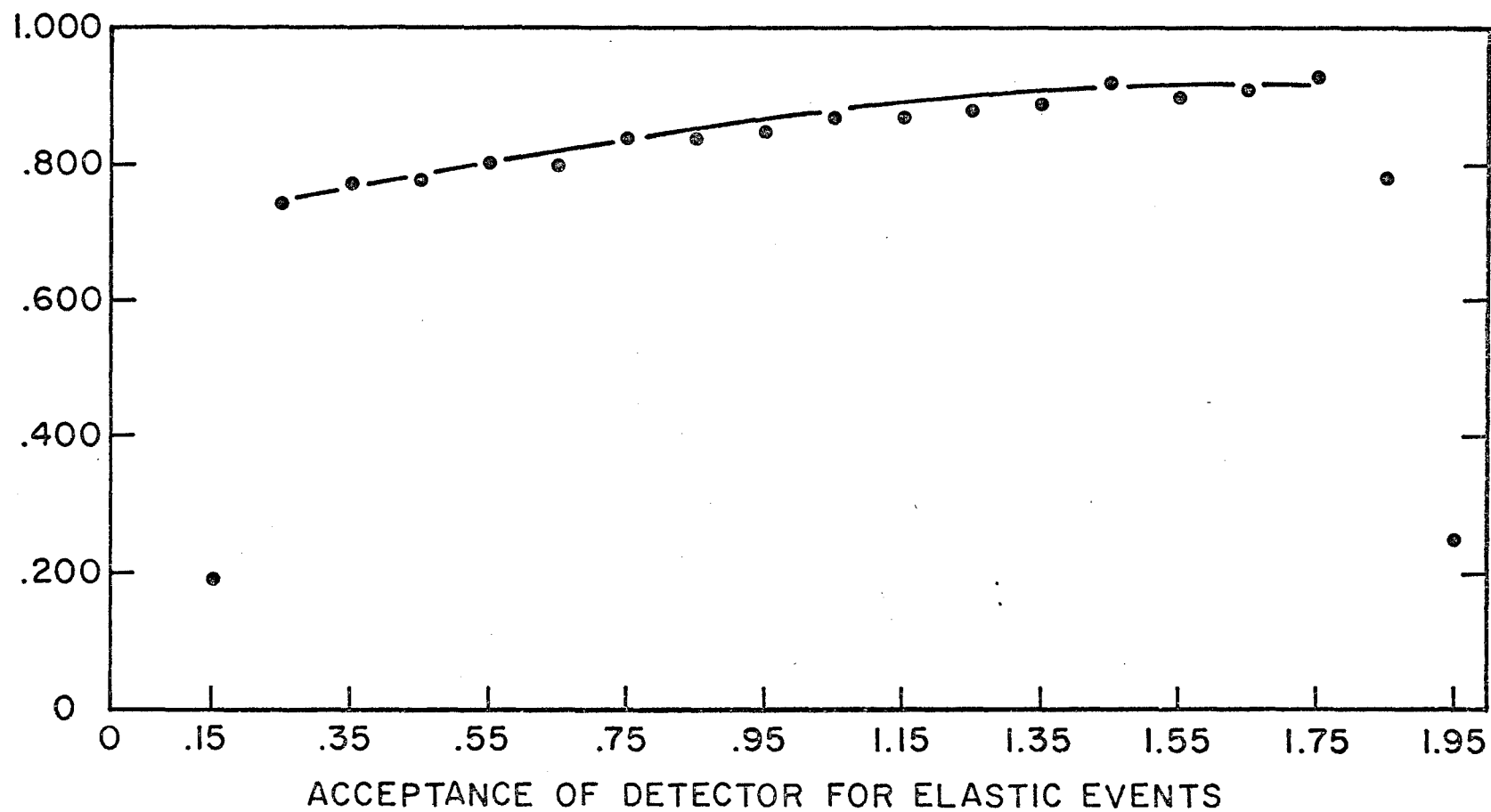


Figure II-2. Monte Carlo acceptance curve for elastic events. Scatters are generated within $\Delta\phi = \pm 10^\circ$.



it is not a problem since the detector is triggered not on the incident beam particle but on a (presumably) scattered particle present on the recoil arm.

To eliminate multi-particle final states and events with a gamma from π^0 decay or from nuclear de-excitation, four scintillator-tungsten sandwich counters were placed over the pole faces of the polarized target magnet. These proved to be essential, as already mentioned: it was found that inelastic triggers were much more probable than elastic triggers in the absence of the veto counters, to the extent that elastic events were locked out. The positioning of these counters is shown in Figure II-5.

Any discussion of background acceptance hinges on the resolution of the proportional chambers. Relevant details are assembled in Table II-1. As a way of estimating contributions to the trigger from inelastic reactions, and inelastic contamination of the signal, we have generated Monte Carlo quasi-elastic and N^* events and tracked them through the system. The results of these calculations are given in Table II-2. We have taken lower energy data and scaled as $s^{-1/2}$ to estimate inelastic cross-sections¹ at 100 and 300 GeV/c, and compared these with known elastic cross-sections at the same energies.² The quasi-elastic events are generated with the usual P^2 dP distribution with a sharp cutoff at 200 MeV/c.

The principal reason that the inelastic contribution is so small is the presence of the forward arm. Not only is the solid angle of the forward arm relatively smaller for multi-

TABLE II-1

Some Details of PWC Resolution and Positioning

I. RESOLUTION - Wire spacing and number of wires.

<u>PWC</u>	<u>X(mm)</u>	<u>Y(mm)</u>	<u>N_x</u>	<u>N_y</u>
WR1	2	2	144	144
WR2	2	4	192	88
WR3	2	6	245	160
WR4	2	6	320	200
WS1	1	1.5	288	128
WS2	1	1.5	408	112
WS3	2	2	192	192
WS4	2	2	312	288

TABLE II-1 (cont'd)

II. POSITIONING, Recoil chambers: all chambers were perpendicular to a ray from the target center making an angle of 50° with the undeflected beam line. For X planes, wire number increased toward the beam line. For Y planes, wire number increased downward. Offsets are given from wire 1 to the 50° line for X planes, and from the $y=0$ plane (i.e. x-z plane through target center) for Y planes. The recoil elements were in the same position for both 100 and 300 GeV data.

<u>PWC</u>	<u>D(cm)</u>	<u>X Offset</u>	<u>Y Offset</u>
WR1	55.	10.95	12.70
WR2	135.	10.26	17.40
WR3	325.	17.52	50.70
WR4	405.	29.49	57.30

Forward chambers: all chambers were perpendicular to the undeflected beam line. For X planes, wire number increased from beam right to beam left. For Y planes, wire number increased downward. Spacing of the forward arm elements increased by a factor of ≈ 2 from the 100 GeV run to the 300 GeV run.

<u>PWC</u>	<u>D(cm)</u>	<u>X Offset</u>	<u>Y Offset</u>
100 GeV			
WS1	1600	-3.59	13.13
WS2	2450	-3.81	0.32
WS3	2950	10.80	32.40
WS4	5900	52.15	-8.00

TABLE II-1 (cont'd)

<u>PWC</u>	<u>D(cm)</u>	<u>X Offset</u>	<u>Y Offset</u>
300 GeV			
WS1	3200	-3.87	13.13
WS2	4800	-4.75	8.32
WS3	5300	8.07	30.8
WS4	9500	31.20	4.90

III. Miscellaneous.

A. Dead Areas: Wires 1-48 in WS1X and 1-112 in WS2X were kept at lower voltage than the rest of the wires; the beam passed through these areas.

B. 26° Planes: WS3Y, WS4Y, WS3Y, and WS4Y had their wires angled at 26° from the horizontal. Coordinates in these chambers were calculated according to

$$Y = \sec(26^\circ) (n \times \Delta S + \text{Offset}) + X \times \tan(26^\circ)$$

with n the center wire in the cluster, ΔS the wire spacing, and X the X coordinate of the cluster in the corresponding X plane.

Table II-2(a)

Monte Carlo Acceptances
for Quasi-Elastic Events

-t	Generated	Recovered	%
.15	1598	60	3.8
.25	3308	224	6.8
.35	3326	184	5.5
.45	3267	199	6.1
.55	3170	200	6.3
.65	3264	241	7.4
.75	3148	257	8.2
.85	3198	262	8.2
.95	3230	251	7.8
1.05	3262	288	8.8
1.15	3328	305	9.2
1.25	3183	283	8.9
1.35	3277	328	10.0
1.45	3204	362	11.3
1.55	3280	355	10.8
1.65	3246	396	12.2
1.75	3184	290	9.1
1.85	3253	207	6.4
1.95	3274	64	2.0

Table II-2(b)

Monte Carlo Acceptances for
Events Decaying to $p (n\pi^+)$

-t	Generated	Recovered	%
.15	272	9	3.3
.25	569	33	5.8
.35	575	45	7.8
.45	561	42	7.5
.55	566	36	6.4
.65	536	31	5.8
.75	523	42	8.0
.85	519	31	6.0
.95	542	39	7.2
1.05	549	25	6.4
1.15	546	45	8.2
1.25	542	46	8.5
1.35	525	33	6.3
1.45	528	43	8.1
1.55	500	47	9.4
1.65	572	53	9.3
1.75	561	40	7.1
1.85	496	39	7.9
1.95	518	6	1.2

particle final states, the momentum measurement in some sense gives an orthogonal indication of the elasticity of the reaction.

III. Logic

In any high statistics experiment, two considerations are of primary importance in the design of the trigger logic. On the one hand, dead times, during which the system cannot register the desired types of events, should be minimized to avoid the loss of events. On the other hand, to be able to subtract background under the signal peak, one must trigger loosely enough to have a statistically significant sample of background events outside the signal region.

The fast logic for the present experiment was designed to be flexible in both respects: within broad constraints it was possible at run time to include or exclude kinematic regions in coplanarity and angle-angle space not populated by elastic events. In addition, with a dynamic trigger and physically dispersed logic stations where each unsatisfied coincidence level reset the dead time gates and reactivated the system, the dead time for any reaction which satisfied the first coincidence but failed to interrupt the online computer was less than 2 μ s. In fact, in the vast majority (>90%) of these reactions, the apparatus reset within 200 ns (i.e. the second level coincidence was not satisfied). Dead times resulting from the fast logic were less than 5% of the live time at the highest fluxes. The selection of specific kinematic regions was possible through the use of flexible two dimensional (matrix) coincidence units, with each dimension fed by 16 channels of proportional chamber fast 'or' outputs. Each 'vertex' in the

matrix, corresponding to the time coincidence of a specific channel from each PWC, was switchable between active and inactive states. In the active state the vertex produced a logical 'YES' (NIM standard for 40 ns) output if the two channels were in time coincidence, else a logical 'NO' output. The outputs from all the vertices were either ganged together to form a single (OR) output for use in standard logic modules, or else were grouped along diagonals to feed another matrix. Figure II-3 indicates schematically how this process worked.

The matrices are useful because elastic events satisfy the following criteria:

- (1) the trajectories of elastic events from WR3X to WR4X are nearly parallel, independent of t ,
- (2) the forward and recoil particles are coplanar with the beam,
- (3) the forward and recoil scattering angles occupy a relatively small region within the acceptance of the detector in angle-angle space, and
- (4) the deflection angle in the forward analysis magnet is for practical purposes constant.

Thus by activating specific regions in the matrices the experimenters were able to require approximate coplanarity, correct scattering angles, and correct forward momentum while excluding events failing any of these criteria. The principal use of parallelism was to eliminate multi-particle final states on the recoil arm. In practice the requirements that (1) a

particle pass through all the recoil arm chambers, (2) without the pole tip veto counters firing, while (3) in proper time coincidence with a particle in WSlX proved sufficient to reduce the trigger rate to manageable levels without selecting specific regions in the matrices at intensities up to $2 \text{ or } 3 \times 10^7$ ppp. Accordingly, the matrices were left open, and the forward momentum and coplanarity matrices not required. It was useful to keep the trigger as loose as possible to permit background studies and to reduce systematic effects associated with fluctuations in trigger devices.

The schematic for the trigger is shown in Figure II-4, and a diagram indicating the placement of counters around the target is given in Figure II-5. A particle scattered from the target was indicated by the RC5 coincidence (particle on recoil arm, incident particle from central region of beam, since no veto from the hole counters). If the recoil particle passed through the recoil analysis magnet and fired WR3X and WR4X in time coincidence with the 'YES' output of RC5, RC1 (M1.RC5) was satisfied. RC1 set the dead time gate to insure that no other reaction could start the trigger sequence before the system was ready. If M2=WR1X.WR2X was satisfied and in coincidence with the signal from RC1, and there was no veto pulse from the pole tip counters (any of the four - see Figure II-4), RC3 was satisfied and the recoil arm PWC's were latched. The SlC1 (=RC3.M3, with M3=WSlX.M2) coincidence contained the angle-angle requirement in the form (WR2X-WR1X) vs. WSlX; the minimum requirement imposed at this

Figure II-3. Schematic use of the matrix coincidence units.

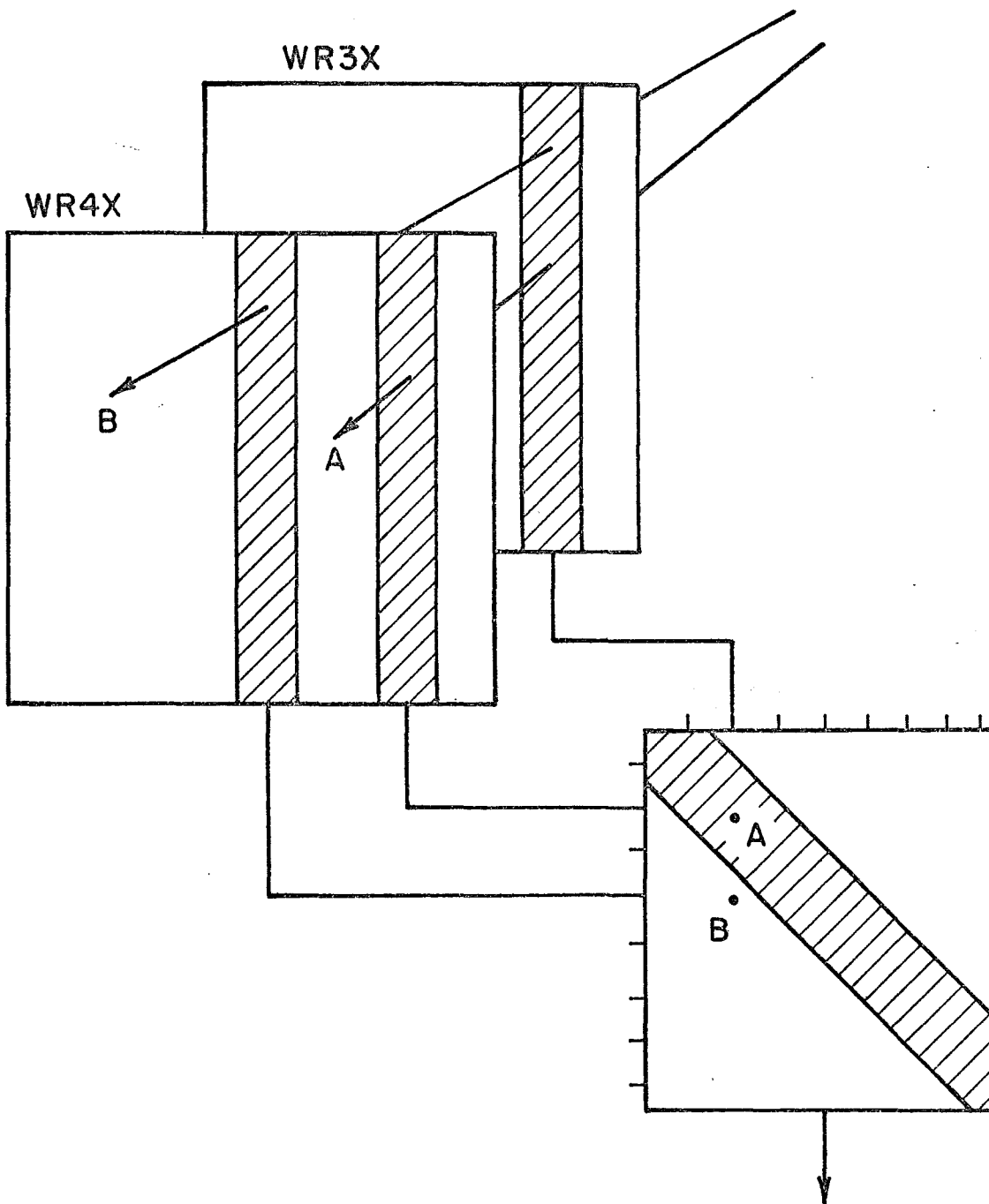


Figure II-4. Fast logic schematic.

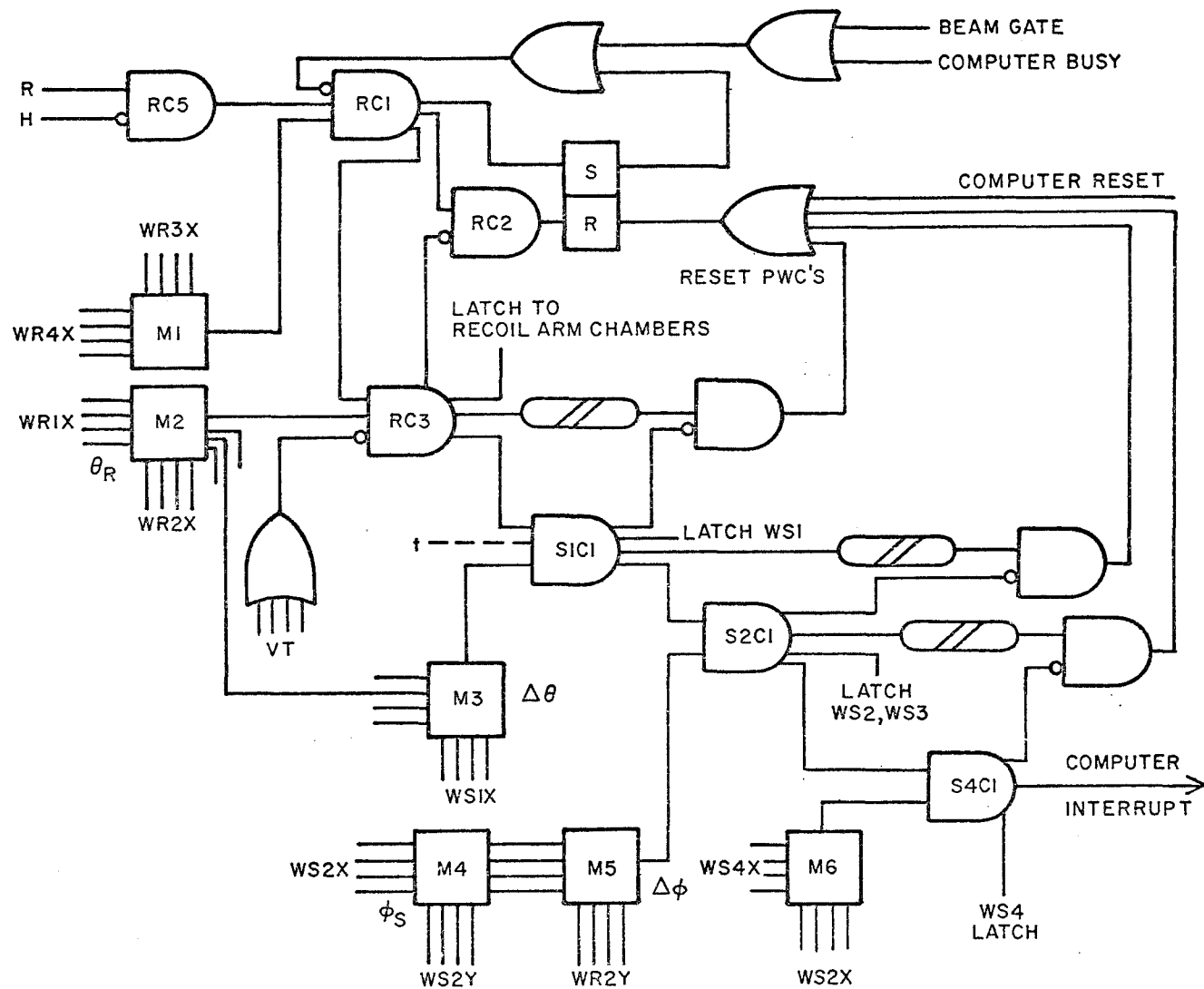
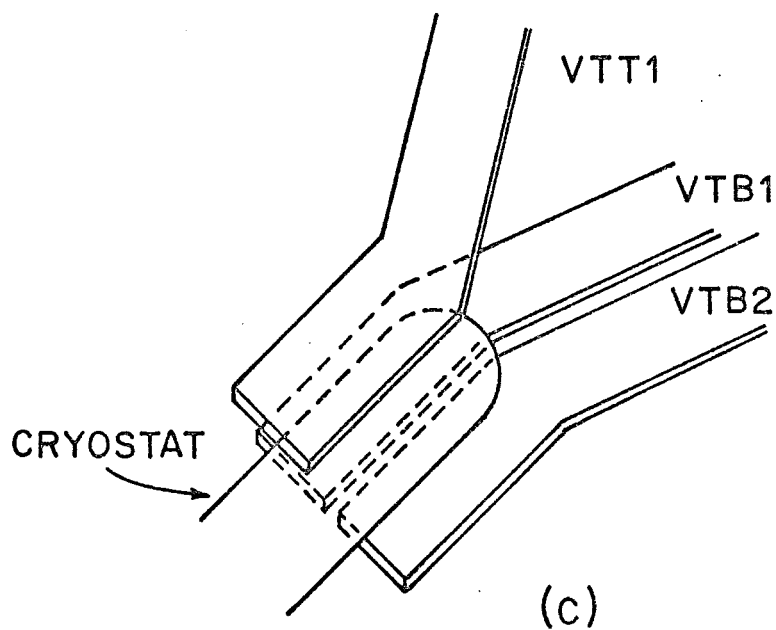
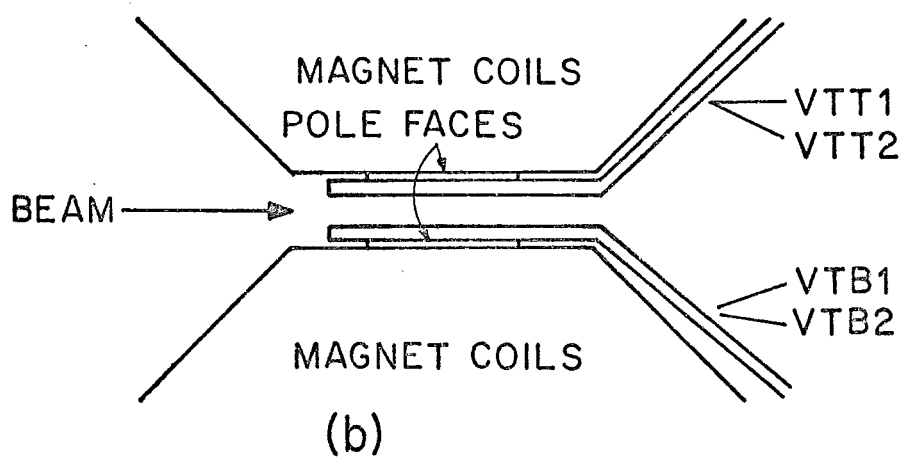
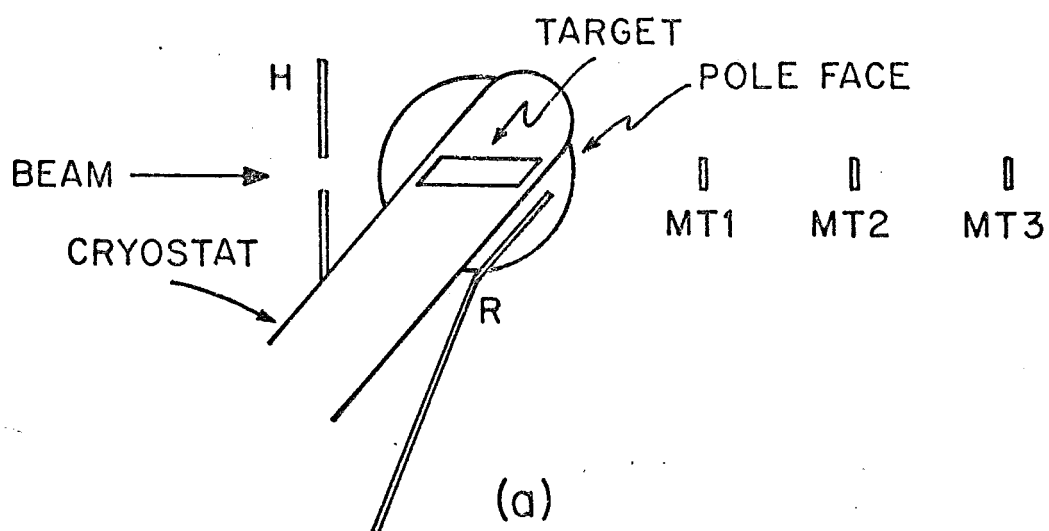


Figure II-5. Schematic for placement of counters around target. Not to scale.

- a) overhead view
- b) side view
- c) detail of pole face veto counter placement.



coincidence was that there be a particle on each arm. During part of the 300 GeV/c run, the S1C1 coincidence was augmented by the addition of a counter (T5) with an adjustable low t cutoff. The S2C1 coincidence ($S2C1 = S1C1.M5$, with $M5 = M4.WR2Y$, and $M4 = WS2X.WS2Y$), nominally the coplanarity requirement, was set to require only S1C1 during the 100 GeV/c run; for the 300 GeV/c run, M5 was required in coincidence with S1C1, but was jumpered to be WS2X alone. Finally, the S4C1 coincidence, which in principle contained the forward momentum requirement, in practice required only the 'YES' output from S2C1 during both the 100 and 300 GeV/c runs. WS1X-Y was latched at S1C1, WS2X-Y and WS3X-Y were latched at S2C1, and WS4X-Y was latched at S4C1. At S4C1 the interrupt to the online computer was generated, and the fast logic locked out until the computer lifted the dead time gate. Usually the total dead time from the interrupt to the dead time gate being lifted was slightly less than 1 ms (about 800 μ s).

At each satisfied coincidence level starting with RC1, an output pulse was generated which, unless vetoed by the next higher coincidence level, reset the dead time gate. For example, if RC1 were satisfied, RC2 would also be satisfied, and would reset the dead time gate, unless RC3 were also satisfied, in which case it vetoed RC2 and left the dead time gate up. The reason for this interlocking set of coincidence levels was to allow the trigger to reset itself, avoiding extremely slow computer intervention, or the yet more serious possibility of the system locking up permanently.

IV. Beam

The beam used in this experiment was the 3.5 mr beam (MLE) in the Meson Lab at Fermilab. Figure II-6 is a schematic of the beam line as it was set up during the present experiment. At the time the maximum momentum at which particles could be transported to the experimental area was 380 GeV/c. The beam line was instrumented with integrating 1 mm wire chambers at various locations. As mentioned above, beam stability was monitored in the experimental area by slit counters immediately upstream of the target and of WS2. The final beam tune had the following parameters at 100 GeV:

momentum bite:	$\delta P/P \sim \pm 1\%$
angular divergence:	$\pm 0.2 \times 0.2$ mr
intensity:	up to $1.5 \times 10^7 \text{ s}^{-1}$.
beam spot size	2 cm horiz x 1.5 cm vert

At 300 GeV these parameters were

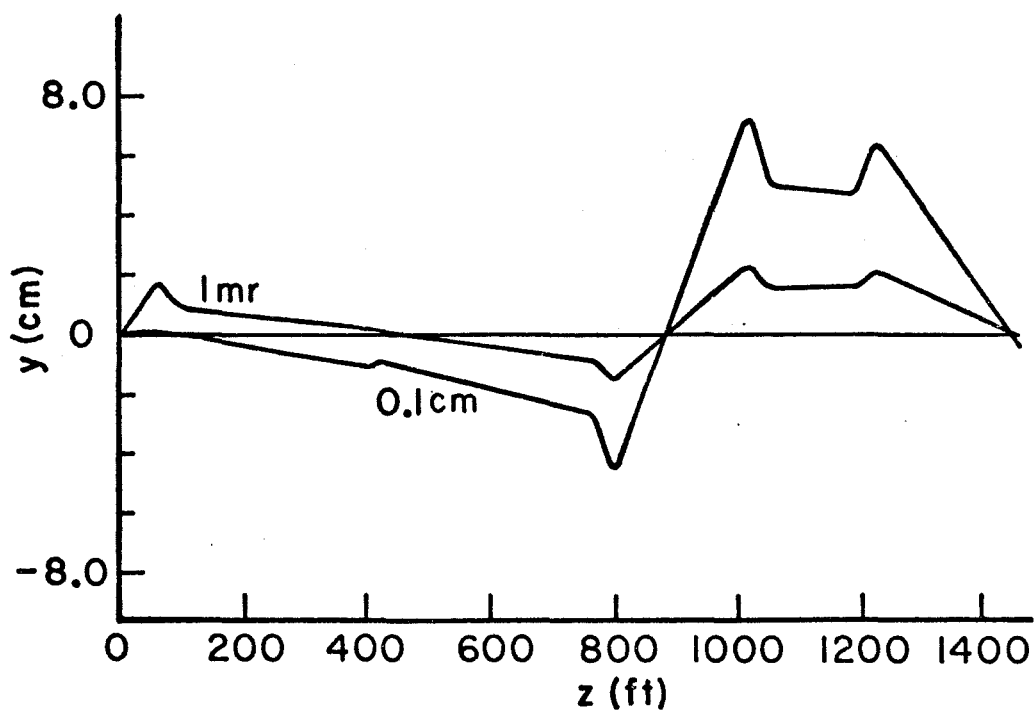
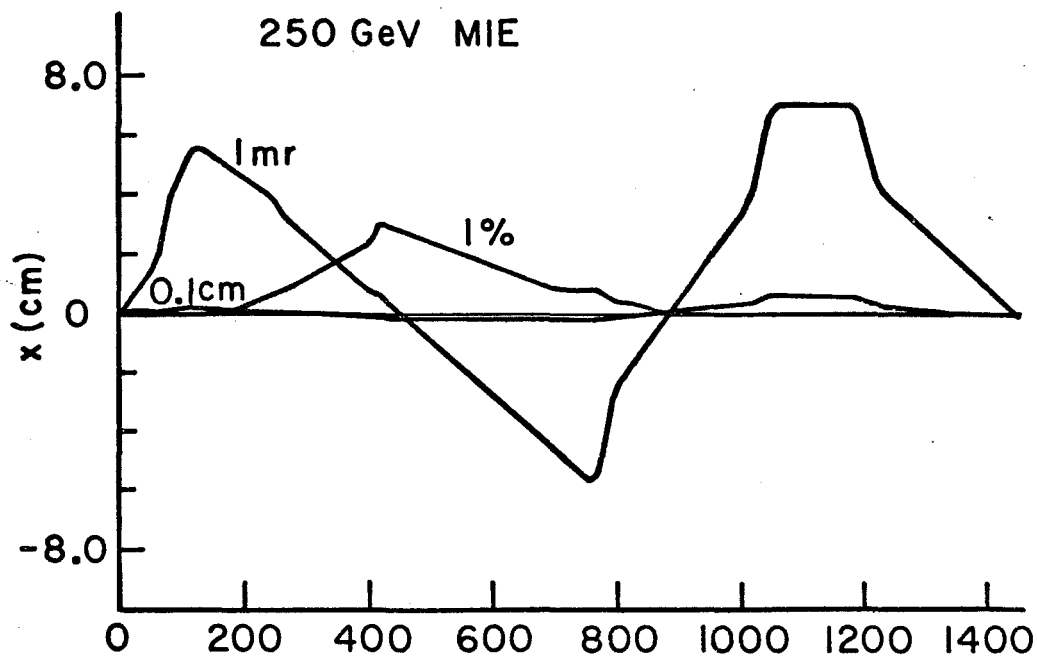
momentum bite:	$\delta P/P \sim \pm 1\%$
angular divergence:	$< \pm 0.1 \times 0.1$ mr
intensity:	up to $3 \times 10^7 \text{ s}^{-1}$.
beam spot size	1.5 cm horiz x 1 cm vert

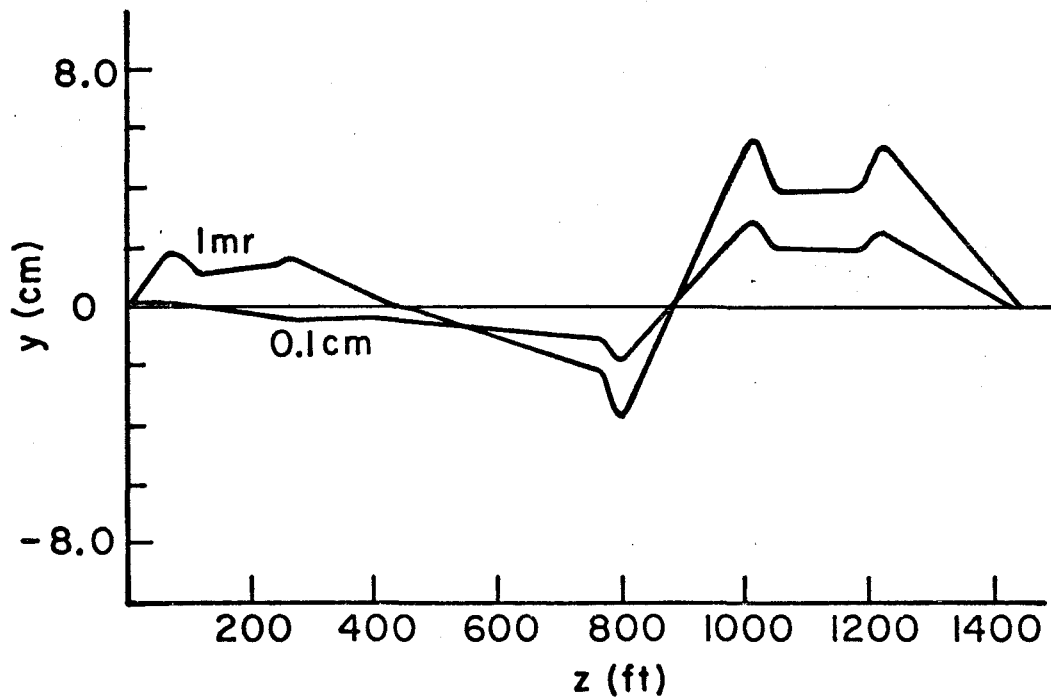
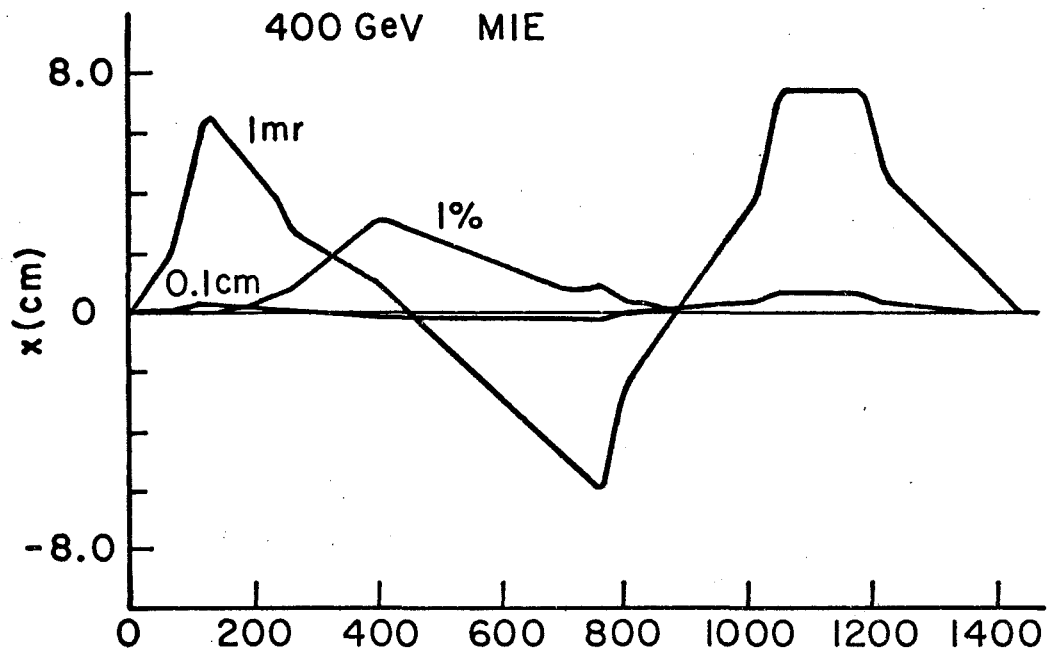
Both 100 and 300 GeV data were taken with primary beam moments of 300 GeV/c and 400 GeV/c; in each case the beam composition was as follows:

100 GeV/c secondary:

300 GeV/c primary:	$\pi/p/K \sim 40/54/6$
400 GeV/c primary:	$\pi/p/K \sim 47/47/6$

Figure II-6. Schematic of beam line. From Ref. 7.





300 GeV/c secondary:

300 GeV/c primary: essentially all p

400 GeV/c primary: $\pi/p \sim 3/97$.

The duration of the beam spill was approximately 1 second with a 400 GeV primary beam, and approximately 2 seconds with a 300 GeV primary beam. The repetition rate was six to eight spills per minute.

With the discovery of significant polarization in inclusive lambda production³ it was obviously of interest to check for polarization in the proton beam. Rather than attempt to measure the beam polarization, it was decided to precess the vertical component of the polarization into the scattering plane. The rationale for this procedure is as follows: since the production of a secondary proton beam proceeds via the strong interactions, parity is conserved, and the only component of polarization which can be non-zero is that normal to the scattering plane at the production target. To first order (i.e. ignoring quadrupoles and the 3.5 mr production angle) this component will be normal at the polarized target, so that a set of dipole magnets, properly oriented and with appropriate fields, will precess the spins into the scattering plane at the polarized target. The configuration chosen is shown in Figure II-7. Several magnets are required since any single magnet not only precesses the beam but also changes its direction.

Appendix II contains a slightly more detailed discussion of the transport system.

Figure II-7. Schematic of spin precession magnet placement.

$$\int \mathbf{B} \cdot d\mathbf{l} = 27 \text{ kG-m for all magnets.}$$

V. Cerenkov Counters

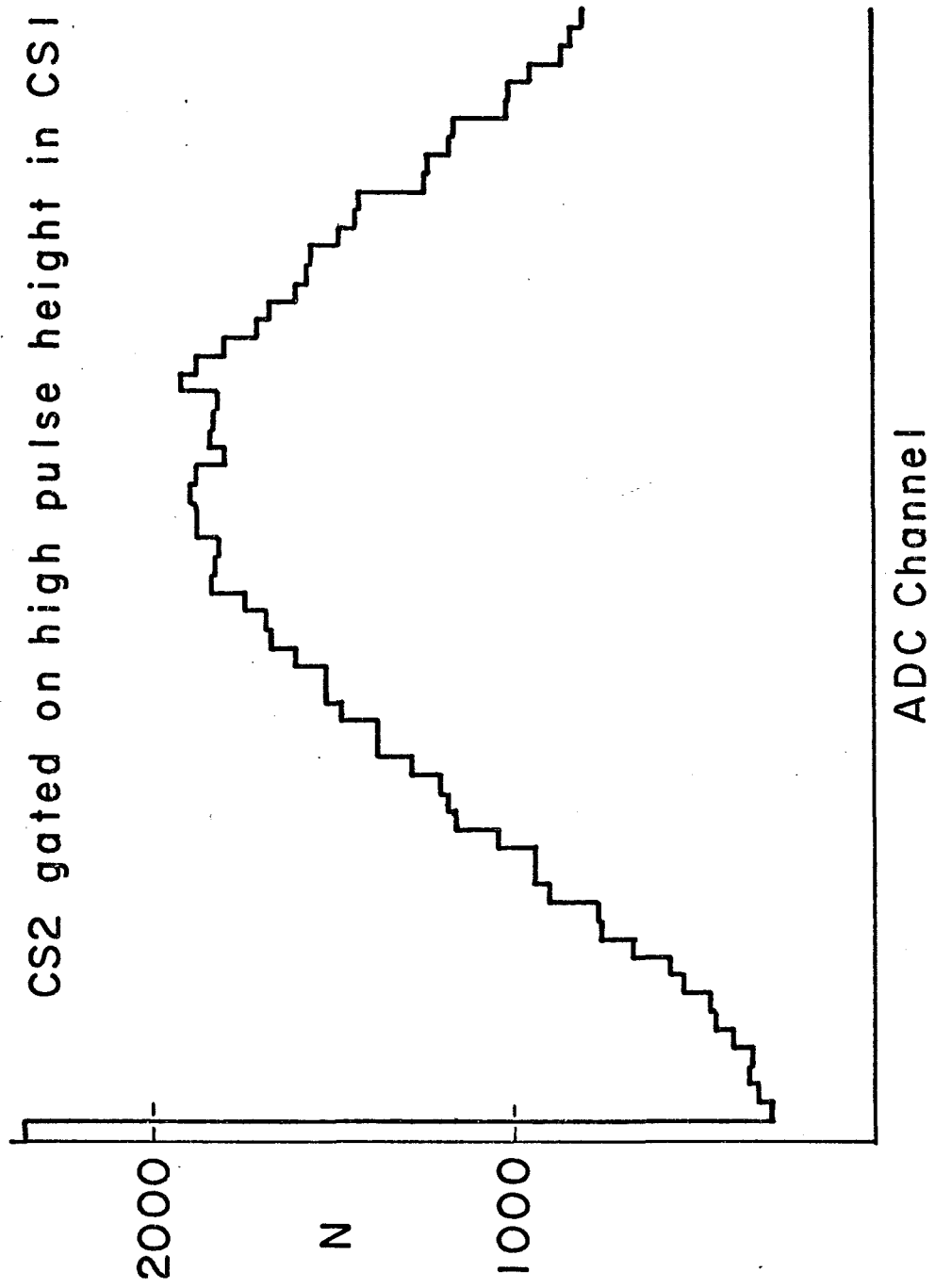
To discriminate among scattered pions, protons, and kaons two threshold Cerenkov counters (CS1, CS2) were placed downstream of the forward arm analysis magnet. The counters were constructed from 9 m sections; CS2 consisted of a single section while CS1 consisted of three sections for the 100 GeV run and four sections for the 300 GeV run. Both counters were filled with N_2 gas at low pressure. During the 100 GeV run the pressure in CS1 was set at 31 mm Hg, the kaon threshold, while CS2 was set at 112.6 mm, the proton threshold. Thus a pi would be indicated by large pulse height in CS1 and CS2, a kaon by large pulse height in CS2 and small pulse height in CS1, and a proton by small pulse height in both counters. However, the number of photo-electrons expected in CS2 from a kaon is small, so that a kaon may well correspond to a small pulse height in CS2 and be counted as a proton; similarly, protons may contaminate the kaon sample by knock-on collisions. We estimate about 5% of the proton sample to be mis-identified, and in view of the small number of incident kaons and the difficulty of extracting kaon scatters from pion and proton scatters, have not tried to calculate polarizations for Kp scattering. During the 300 GeV run, the pressure in both counters was set at ≈ 10 mm, the proton threshold.

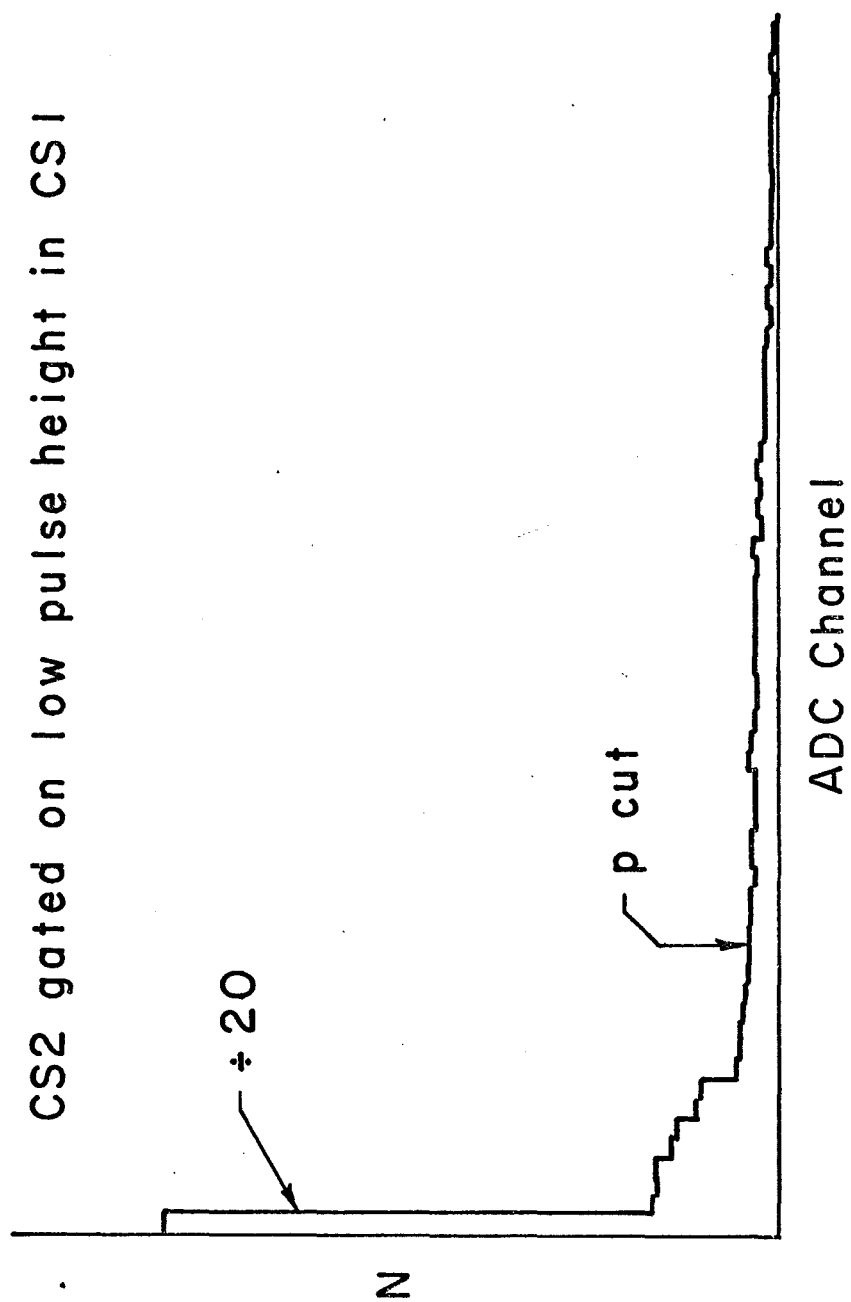
The efficiency of the Cerenkov counters was measured at 100 GeV by tagging beam particles at low rates upstream of the detector with a differential Cerenkov counter; allowing for

differences in the scattering cross-sections and for decays upstream of CS1, it is possible to calculate the efficiencies directly. Again at 100 GeV, the pion efficiency was found to be about 99.3%, when the pulse height in CS1 was above a certain level. CS1 and CS2 can also be gated on each other, although this is not immediately susceptible to interpretation since each counter has its own inefficiencies, and the presence of three different particles prevents us from identifying a unique part of pulse height space with a given particle. The least ambiguous test involves looking at the pulse height spectrum in CS2 gated on high pulse height in CS1, which is nearly all pion. This plot is given in Figure II-8; the lowest channel contains approximately 2% of the events in the plot, consistent with the direct measurement of CS2 efficiency.

At 300 GeV, with protons comprising 97% or more of the beam, contamination of protons by pions is important only at high t , and even at $t = -1.3 \text{ GeV}^2$ proton scatters should be about three times more numerous than pion scatters. Using the differential Cerenkov counter the pion inefficiency was found to be about 5% which is sufficient for the pp polarization measurement at high t .

Figure II-8. Cerenkov counter ADC spectra.





VI. Polarized Proton Target

No polarized target experiment would be complete without a polarized target. The present experiment used a target developed at Argonne National Laboratory. Since by 1977 the technology of polarized targets is relatively standard, we refer the reader to the literature,⁴ and content ourselves with a brief summary of the operating parameters of the present target.

The target magnet was the Zoltan magnet used at Berkeley during the polarization experiments of the 1960's: it generated a central magnetic field of 25 kG uniform to a few gauss over the target volume, and had an integrated Bdl over a diameter of 1130 kG-cm.

The target material was ethylene glycol doped with potassium dichromate radicals. Its equilibrium polarization under normal conditions was approximately 0.1%; with standard spin pumping techniques polarizations as high as 90% were achieved, although an average polarization between 75 and 85% was more common. The volume density of free protons was approximately 0.07 gm/cm³, comparable to that of a liquid hydrogen target. The target canister was a teflon box with dimensions 2 cm x 2 cm transverse to the beam by 8.4 cm longitudinal to the beam (see Figure II-5) into which the target material, formed into .1 mm beads, was deposited. The target was cooled to the operating temperature of 0.45°K by a closed loop He³ system in contact with an open He⁴ system. Every two runs the target enhancement was reversed; under normal conditions this corresponded to a reversal each hour.

VII. Monitors

As mentioned in the Introduction to this section, the intense flux, necessary for a high t measurement of the polarization, made the use of direct particle monitors such as proportional chambers or scintillator hodoscopes impossible. Obviously a knowledge of the incident particle flux is necessary for any measurement of cross-sections; it is even more crucial for polarization measurements, since the polarization is proportional to the difference of cross-sections for different spin orientations of the target. Of course, it is also necessary to monitor beam stability. Deprived of the usual direct monitors, we relied on several indirect monitors, and estimated the errors on our normalization from the deviations among them.

The position and shape of the beam were monitored by integrating proportional chambers at several locations along the beam line. These chambers proved extremely useful; many times they alerted us to magnets which were not regulating properly.

In the experimental area beam position and divergence were monitored by slit counters immediately in front of the target, and in front of WS2. By putting the counters at the target into the trigger circuitry in anti-coincidence, we obtained a trigger sensitive primarily to the beam incident on the target.

To monitor beam flux we relied primarily on monitors such as telescopes and veto counters which detected (inelastic)

scattered particles from the target. While an ion chamber was available and operational, it was less sensitive to beam fluctuations than were the other monitors. Of these indirect monitors, two proved most useful: a pair of three-counter-telescopes, mounted at 100 milliradians above and below the horizontal (for the 100 GeV run only the lower telescope was mounted) and in coincidence with the hole veto counter in front of the target (MT. \bar{H} (U) and MT. \bar{H} (D)), and coincidences between pairs of the four pole tip veto counters (VTT1, VTT2, VTB1, and VTB2). Typically these monitors agreed within a few per cent. Normalization of telescope counts to incident flux was made by scaling counts in a pair of crossed scintillators in coincidence which were directly in the beam. Over a wide range of intensities the telescope counting rate was found to be proportional to the scintillator counting rate (up to intensities at which the scintillator phototubes saturated). The proportionality constant thus determined was used to normalize the telescope at intensities at which the scintillators would have been useless. To calculate polarization, we defined a monitor:

$$F = \text{MT.}\bar{H}(\text{U}) + \text{MT.}\bar{H}(\text{D}) + 0.01 * (\text{VTT1.VTB2} + \text{VTT2.VTB1}) \quad (1)$$

(the factor of .01 is included to make the two monitors comparable, $100 \text{ MT.}\bar{H} \approx \text{VT}$. We chose to include the two monitors with equal magnitudes since the statistical error associated with either is much smaller than the error on the number of elastics and probably smaller than the systematic error associated with either monitors; it was our hope that by using the sum of two

independent monitors of equal size, the systematic error on the new monitor would be reduced). In the future, we shall abbreviate $MT.\bar{H}(U) + MT.\bar{H}(D)$ as MT , and $VTT1.VTB2 + VTT2.VTB1$ as VT .

One other monitor deserves attention, the quasi-elastic scattered particles. In many polarized target experiments this background serves as the principal monitor,⁵ against which all others are checked for stability. In this experiment, the number of events identified as elastic is roughly double the number identified as quasi-elastic (because of differing acceptances for the two kinds of triggers), so normalizing to this background would mean that the statistical errors would be dominated by the error on the background. We have used the numbers of quasi-elastic events only to calculate background asymmetries, i.e. as a loose check on the stability of the other monitors. It turns out, however, that there is a systematic error associated with the other monitors as described in Chapter III, and after normalizing and including these errors, the polarizations calculated with either monitor are very similar.

Various other monitors have been useful, primarily in the analysis of the data, e.g. coincidences between proportional chambers (from the matrices), various fast logic coincidences, and 'accidental' coincidences, in which one of the signals into the coincidence is delayed by several RF buckets.

VIII. CAMAC and the On-Line Program

The interface between the detector on the experimental floor and the online computer was a conventional CAMAC system consisting of CAMAC crates and modules, connected with the online computer by an EG&G BD011 branch driver. The data written into and read from the CAMAC system can be classified under one or the other of two broad types: data read by the computer once each spill, and data read each event.

Included under the "data each spill" heading are scaler data, beam magnet data, and target polarization data. The scaler data consisted of counts in various external monitors, e.g. the counts in telescopes or in the matrices, number of times during the spill certain coincidences in the fast logic occurred, and certain integrated pulse heights. These counts were accumulated in Jorway quad blind scalers, and were used on-line to monitor the stability of components of the apparatus, and offline to normalize the data.

The beam magnet data, obtained only during the 300 GeV running period, were digitised forms of beam magnet shunt readings provided by the Fermilab magnet control system (MAC). While potentially useful, these were in practice never used.

Finally, the polarization data consisted of a digitised form of the NMR sweep. This was provided by the Berkeley "1260" system used in earlier polarization experiments by the Berkeley group. It coupled to the CAMAC system through two Jorway CAMAC modules.

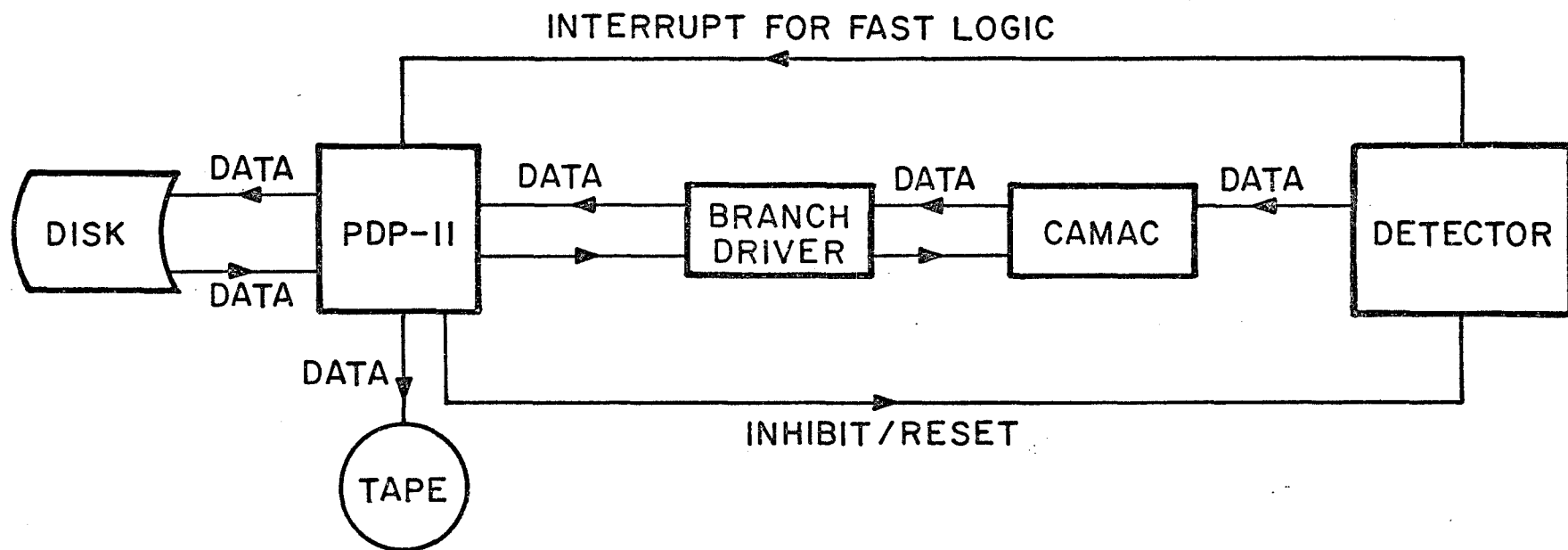
The data read each event divide naturally by type of measuring device: pulse height information from the Cerenkov counters was digitised in LeCroy analogue to digital converters (ADC's), positional information collected by scintillators was indicated by set latch bits in latch modules, and positional information collected by the proportional chambers was stored in compact format in special CAMAC modules designed and built at Yale, called PWC word buffers.⁶

IX. The On-Line Program

To collect the formatted data from the CAMAC hardware, to write it to magnetic tape for later analysis, and to provide diagnostic information about the state of the apparatus, a Digital Equipment Corporation (DEC) PDP-11/20 16 bit mini-computer was supplied by Fermilab. The on-line program, written specifically for this experiment, was a complex swapping system running under the general auspices of DEC's DOS operation system with 24 K of 16 bit ferrite core memory, a fixed head disk drive, and a 9 track magnetic tape drive.

The general flow of the data taking process is shown in the schematic in Figure II-9. An interrupt generated by the fast logic alerted the on-line computer that a scattering reaction satisfying all the coincidence requirements had occurred; by this time the gates on the fast logic (the "suicide gates") prevented the logic from responding to other reactions. This interrupt caused a jump to the data collection routine; and the BD011 was conditioned to transfer data from CAMAC buffers into a buffer in the computer memory. On the completion of the transfer the computer was interrupted a second time, from the BD011, at which time it conditioned the BD011 to initialize appropriate CAMAC modules. After clearing the suicide gates the computer returned to the task in which it had been engaged when interrupted. The entire process, from first interrupt to the clearing of the gates, was accomplished in 600 to 800 μ s, assuming buffer space was available. In principle the program was capable of accepting more than 1000 events each spill; in

Figure II-9. Schematic of data flow.



practice memory limitations and disk access times limited the rate to approximately 600 events per spill (an "event" comprised 40 to 100 16 bit words).

When not engaged in a data transfer, the program was set up to process the most recent data to provide diagnostic information on the apparatus. Typical of this information were proportional chamber wire maps and pulse height spectra for the Cerenkov counters. An interesting and often useful feature of the program was its ability to display wire maps or spectra gated on the presence or absence of data in a particular chamber. Another useful feature was the ability to set up histograms and scatterplots during the data taking process. These two features were especially useful in locating failures in the PWC associated electronics.

References for Chapter II.

1. Giacomelli, G., in Proceedings of the Sixteenth International Conference on High Energy Physics 1972 (Fermilab, Batavia, Illinois 1972).
Edelstein, R.M., et al., Phys. Rev. D 5, 1073 (1972).
Kwak, N., et al., Phys. Lett. 62B, 359 (1976).
2. Akerlof, C.W., et al., Phys. Rev. D 14, 2864 (1976).
Kwak, N., et al., Phys. Lett. 58B, 233 (1975).
3. Bunce, G., Phys. Rev. Lett. 36, 1113 (1976).
4. See e.g. the Book of the 2nd International Conference on Polarized Targets, Berkeley, 1972 (G. Shapiro, ed.),
Jeffries, C.D., Dynamic Nuclear Orientation, Interscience, 1963, or A. Etkin, thesis, Yale University 1971 (unpublished).
5. For example see the comments in Gaidot, A., et al., Phys. Lett. 57B, 389 (1975).
6. Dhawan, S., IEEE Trans. Nucl. Sci. 21NS, 922 (1974).
7. Ecklund, S., M1 Users' Guide, FNAL TM 743-2833 (Batavia, Illinois).

DATA ANALYSIS

I. Introduction

The data reduction process can be divided into three well defined stages: the processing of the raw data tapes to eliminate those triggers in which it was not possible to reconstruct a track on each arm, and elimination of unnecessary information from acceptable events; the kinematic analysis of the reconstructed events and production of second pass magnetic tapes containing kinematic information; and the study of the data sample as a whole, leading to the calculation of quantities relating directly to the physics of the experiment. The analysis described below was implemented on a Digital Equipment Corporation (DEC) PDP-11/45 mini-computer equipped with 28 K of 1 μ s ferrite core memory, a 2.5 Mbyte disk, two 9 track magnetic tape drives and a Tektronix 4012 storage oscilloscope with graphics capabilities. Hard copy was obtained from two DEC teleprinters, the LA36 and LA180. Programs were written either in FORTRAN (as implemented by DEC in its RT11 operating system) or in PDP11 assembly language.

II. The Condensed Tape Program

The condensed tape program served two functions, both deriving from the large number of raw data tapes (more than 300 over two 6-week runs). First, culling the data to eliminate ambiguous or unreconstructable events and producing a relatively small number (~30) of first pass tapes is desirable since it is inconvenient to transport the larger number of tapes. Second, separating the thinning process from the kinematic analysis enable us to analyze the data several times. This would not have been possible if each analysis had proceeded directly from the raw data tapes.

Our criteria for selecting events to be passed to subsequent stages for the analysis were determined by the need to reconstruct the momentum of the recoiling particle and the horizontal and vertical projected angles of both particles. We consider the requirements on each arm separately.

On the forward arm, to reconstruct the horizontal projected angle we required WS1X and either WS2X or WS3X. The combination of WS2X and WS3X was unacceptable since those two chambers were too close to allow an accurate measurement of the angle. We were reluctant to use WS4X in combination with another X chamber for two reasons: first, we considered it unlikely that a trigger with two of the first three chambers empty would be elastic, and second, we intended to use WS4X in the later stages of the to determine the momentum of the forward particle.

To enable us to reconstruct the vertical projected angle

on the forward arm we required WS1Y and any other Y chamber, or WS2Y and WS4Y. Again the WS2Y-WS3Y combination is an imprecise measurement of the angle. (We note here that whenever we say that we require a particular 3Y or 4Y chamber on either arm, we implicitly require that the X view was present, since the 3Y and 4Y chambers have their wires at 26° from the horizontal).

On the recoil arm, the need to reconstruct the momentum accurately led us to require that all four recoil X chambers have clusters present. To reconstruct the vertical projected angle (the ascension angle), we required either of the two vertical chambers between the PPT magnet and the analysis magnet, and any other recoil Y chamber.

Triggers which satisfied the above conditions contained the necessary information for us to reconstruct angles and the recoil momentum. However this information was sufficient only for "clean" events, triggers in which each required chamber had exactly one cluster. More often the trigger had several clusters in one or more chambers; to recover triggers in such cases without admitting appreciable inelastic background we imposed cuts based on the following assumptions.

First, we felt that there was no simple way to retrieve events with two tracks on either arm, and consequently eliminated triggers with multiple clusters in both the 1X and 2X chambers. Second, we felt that the chambers on the side of the analysis magnets furthest from the target should be relatively clean, since these magnets tend to sweep low momentum particles away from the chambers. We therefore eliminated triggers with multiple clusters on both sides of an analysis magnet. For

both reasons we eliminated triggers with multiples in both WR3X and WR4X. We allowed multiples in WS3X and WS4X when WS1X and WS2X were "clean", since the momentum measurement on the forward arm is not as crucial as on the recoil arm, and since there is an appreciable probability of scattering between WS3X and WS4X.

Since the system had more redundancy on the vertical projected angles - to first order, the analysis magnets did not affect the vertical component of momentum - our requirements for this measurement were looser: triggers with any one vertical chamber having exactly one cluster were accepted (as long as that chamber were one of the pair satisfying the minimum requirements stated earlier). We then resolved the ambiguity in the chamber with multiple clusters by ray tracing to a second chamber with exactly one cluster, if possible, or back to the target, if not.

After the appropriate clusters in each chamber had been selected, the positions and number of wires in each cluster, along with the ADC data from the Cerenkov counters and the latch data, were packed into a buffer and subsequently written to magnetic tape.

III. The Analysis Program

The analysis program constructed positions and angles from the data packed on the condensed tape, and used these quantities to construct the kinematic variables characterizing each event. While the details were quite involved, the process can be quickly summarized. Figure III-1 shows our coordinate system.

We first constructed projected angles ψ_S , ψ_R , ψ'_R , in the x-z plane, and ascension angles α_R and α_S . The horizontal component of the recoil momentum was taken proportional to the inverse sine of the difference $\psi'_R - \psi_R$. Knowing the momentum of both particles, we could then compensate for the deflection angles in the target magnet and construct laboratory scattering angles θ_S , θ_R , and ϕ_S , ϕ_R . By compensating for energy loss in the target we constructed the momentum at scatter of the recoil particle. This gave us six quantities characterizing each event: the two scattering angles, two azimuthal angles, and two momenta. We chose as measures of the "elasticity" of the scatter the coplanarity and the chi-square of the fit to the average t of values of t calculated from the two scattering angles and from the recoil momentum (the error on the forward momentum determination of t is larger than the t acceptance of the detector, so we excluded it from the fit). The formulae for these calculations are

$$t_{RP} = 2 m_P (m_P - E_R) \quad (1)$$

with
$$E_R^2 = P_R^2 + m_P^2,$$

$$t_{R\theta} = \frac{-4 m_P^2 \cos^2 \theta_R}{\left(\frac{m_P + E_B}{P_B}\right)^2 - \cos^2 \theta_R} \quad (2)$$

with $E_B(P_B)$ the energy (momentum) of the beam, and

$$t_{S\theta} = -P_S^2 \theta_S \quad (3)$$

with P_S obtained by a single iteration using the beam momentum as the starting value for P_S .

Having formed the individual t 's, we obtained the best fit to t by minimizing the quantity

$$\chi^2 = \Sigma \frac{(t - t_i)^2}{\delta^2(t_i)} \quad (4)$$

where the $\delta(t_i)$, resulting from chamber resolution, multiple scattering, and the error on our energy loss compensation, are calculated for each event as a function of t . The quantities t , t_i , $\delta(t_i)$, and $\Delta\phi/\delta\phi = (\phi_S - \phi_R)/\delta\phi$, along with the χ^2 and the Cerenkov pulse heights and a status word for the event are then packed to a buffer to be written to the second pass "physics" or "summary" tape.

As an example of this process we show in Figure III-2 plots of χ^2 versus number of events cut on coplanarity for various t . The shaded region in each plot is the same quantity cut on large coplanarity. Figure III-3 is a plot of number of events versus coplanarity cut on small χ^2 . We also show in Figure III-4 various other plots obtained from the analysis program.

Figure III-1. Coordinate system for analysis.

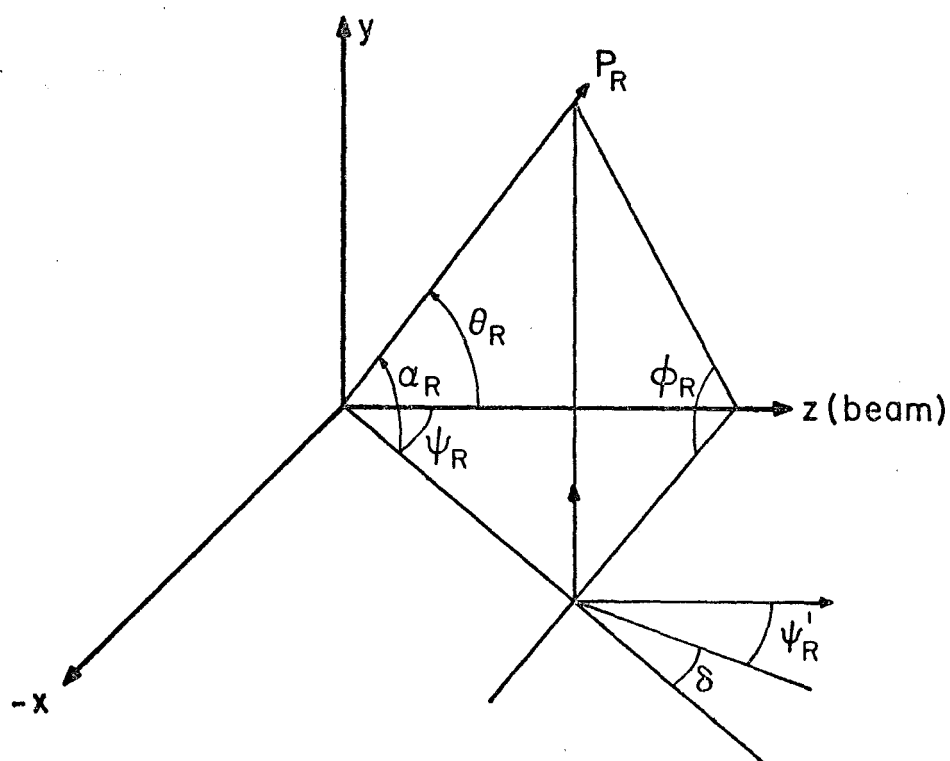
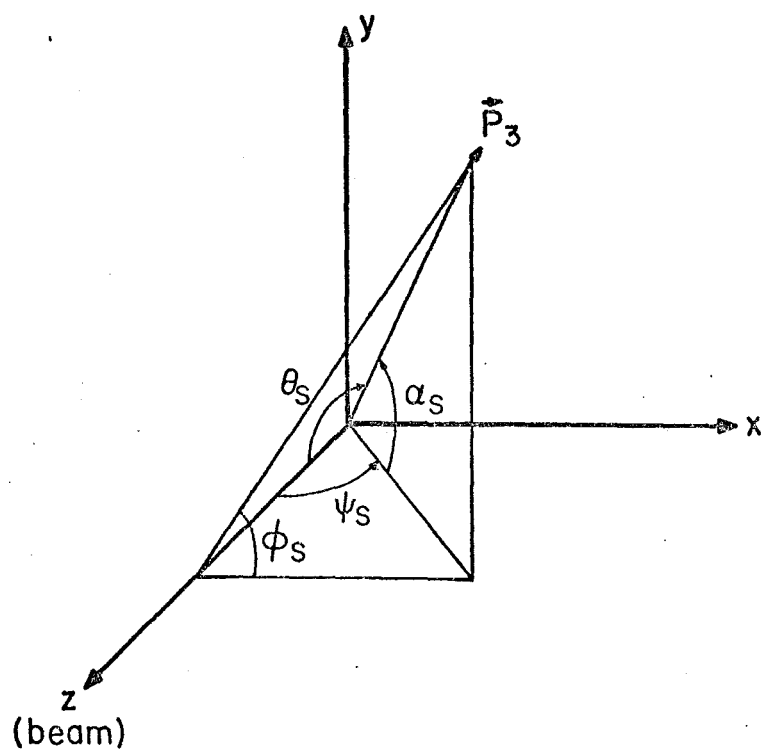


Figure III-2. Plots for 300 GeV pp data, cut on coplanarity.
The shaded region is cut on large coplanarity
and scaled to fit the tails of the distribution
cut on small coplanarity.

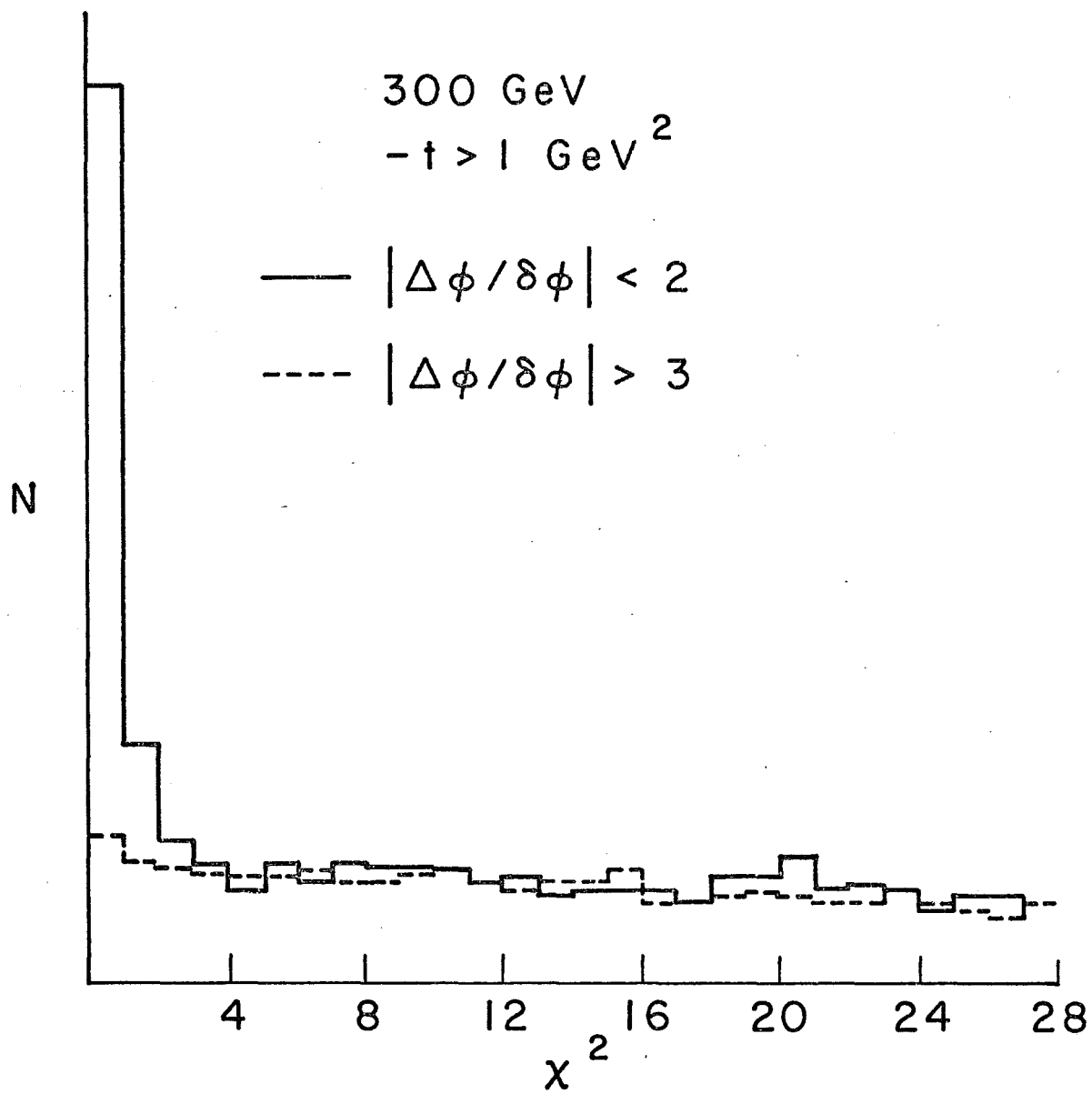
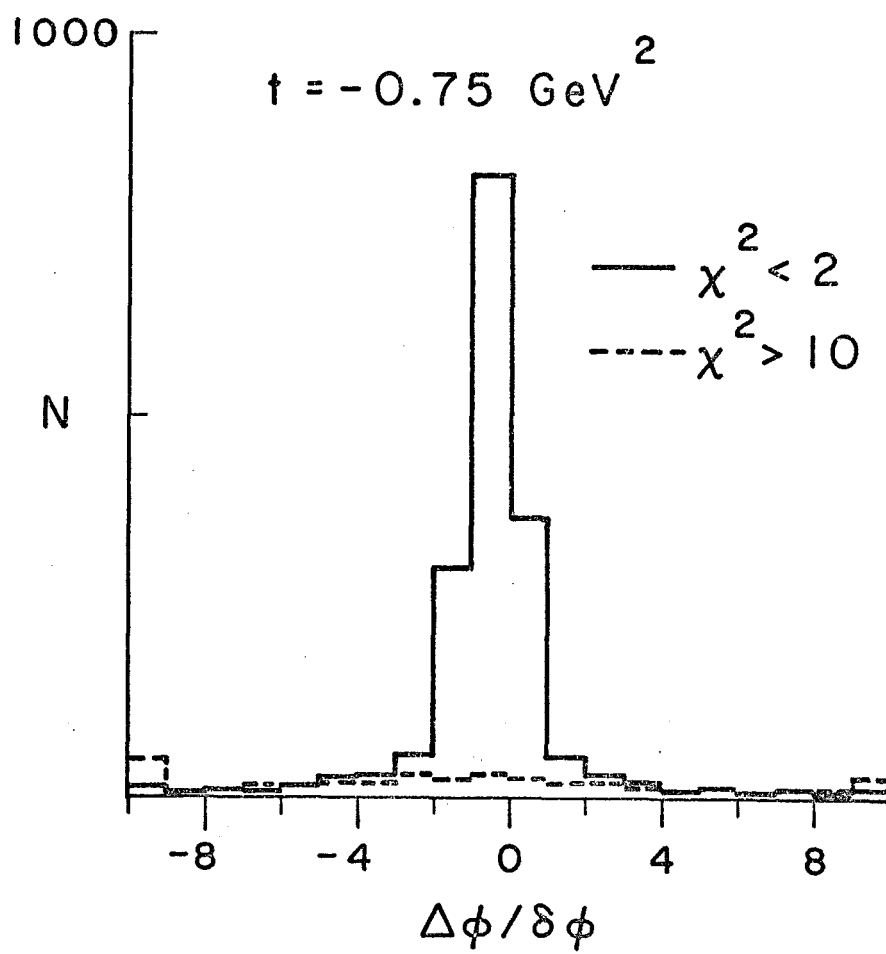


Figure III-3. Delta coplanarity plots for 300 GeV data cut on chi square distribution. The shaded region is cut on large chi square and scaled to fit the tails of the distribution cut on small chi square.

a) at $t = -0.75 \pm 0.05 \text{ GeV}^2$

b) at $t = -1.35 \pm 0.05 \text{ GeV}^2$



$\sqrt{s} = -1.35 \text{ GeV}$

300 GeV

48 evts signal / 60 evts background

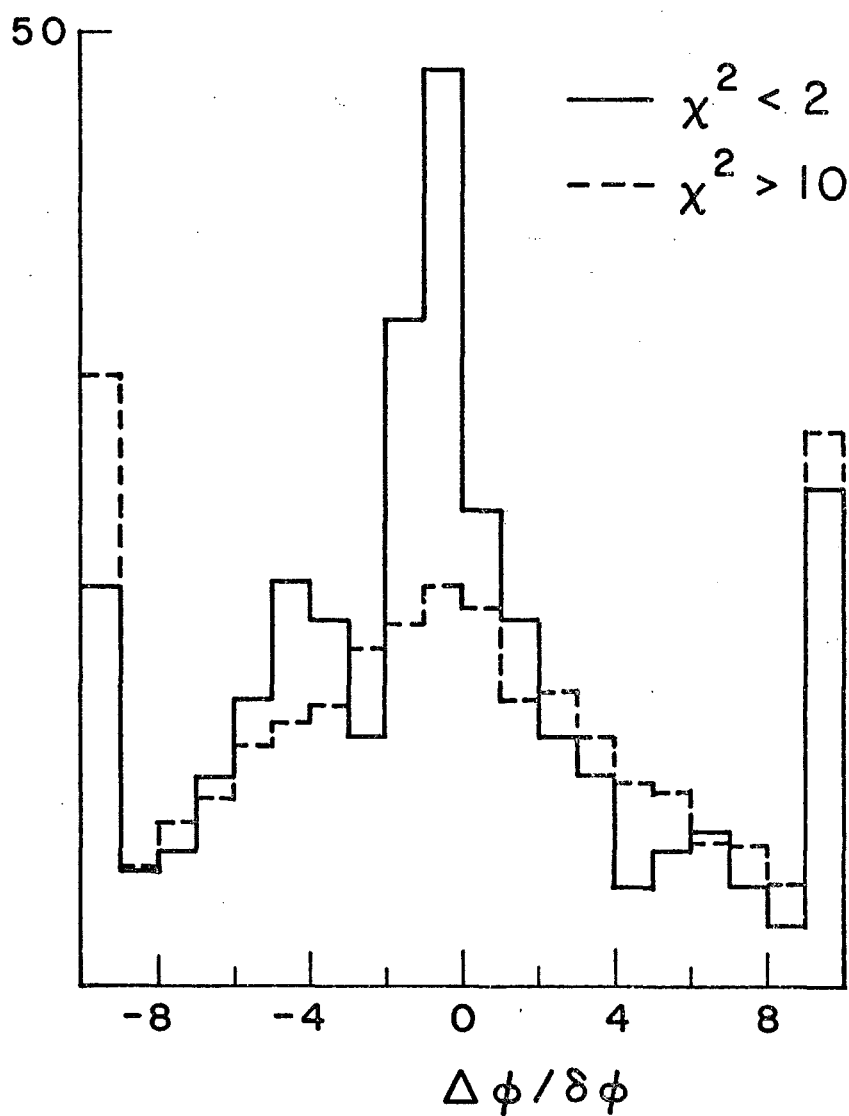
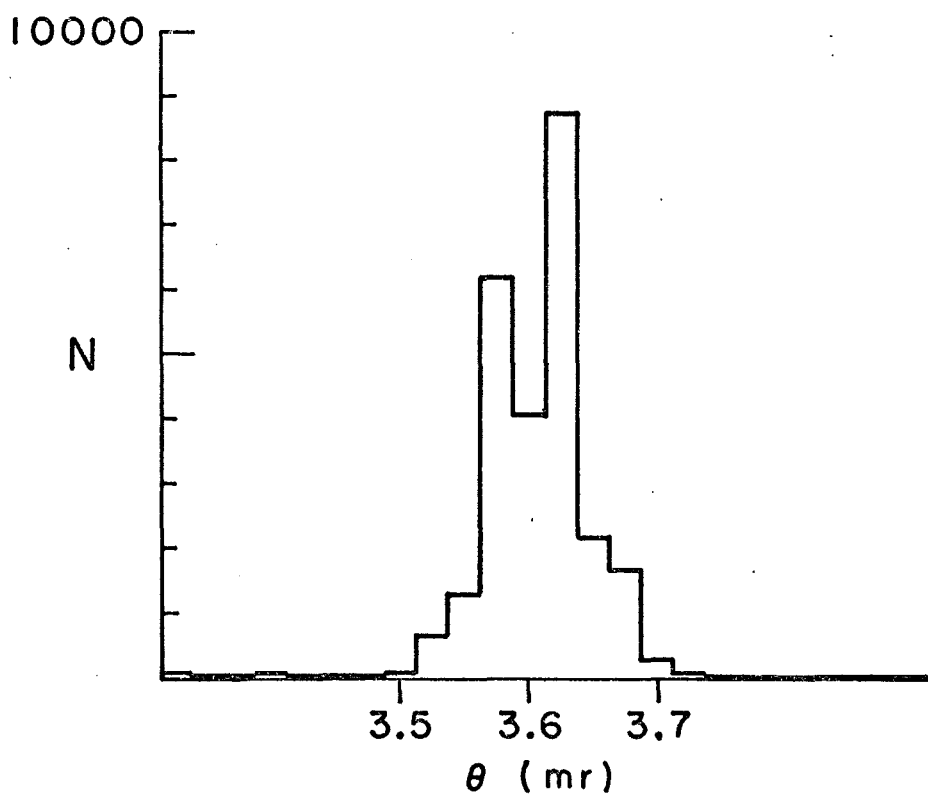
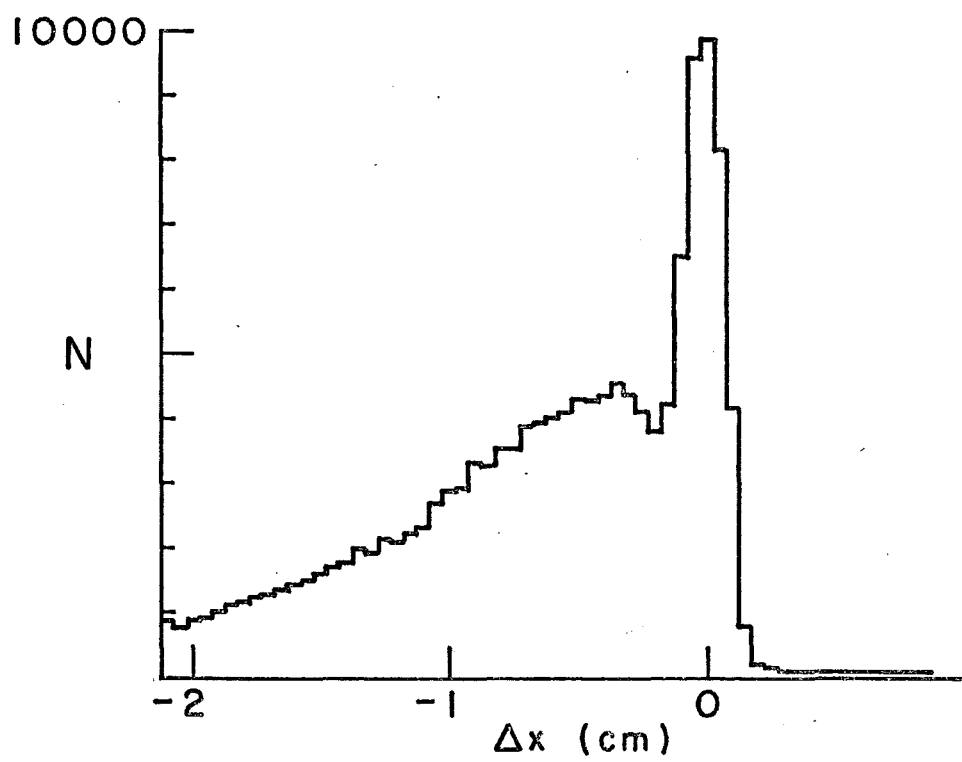


Figure III-4. Analysis plots.

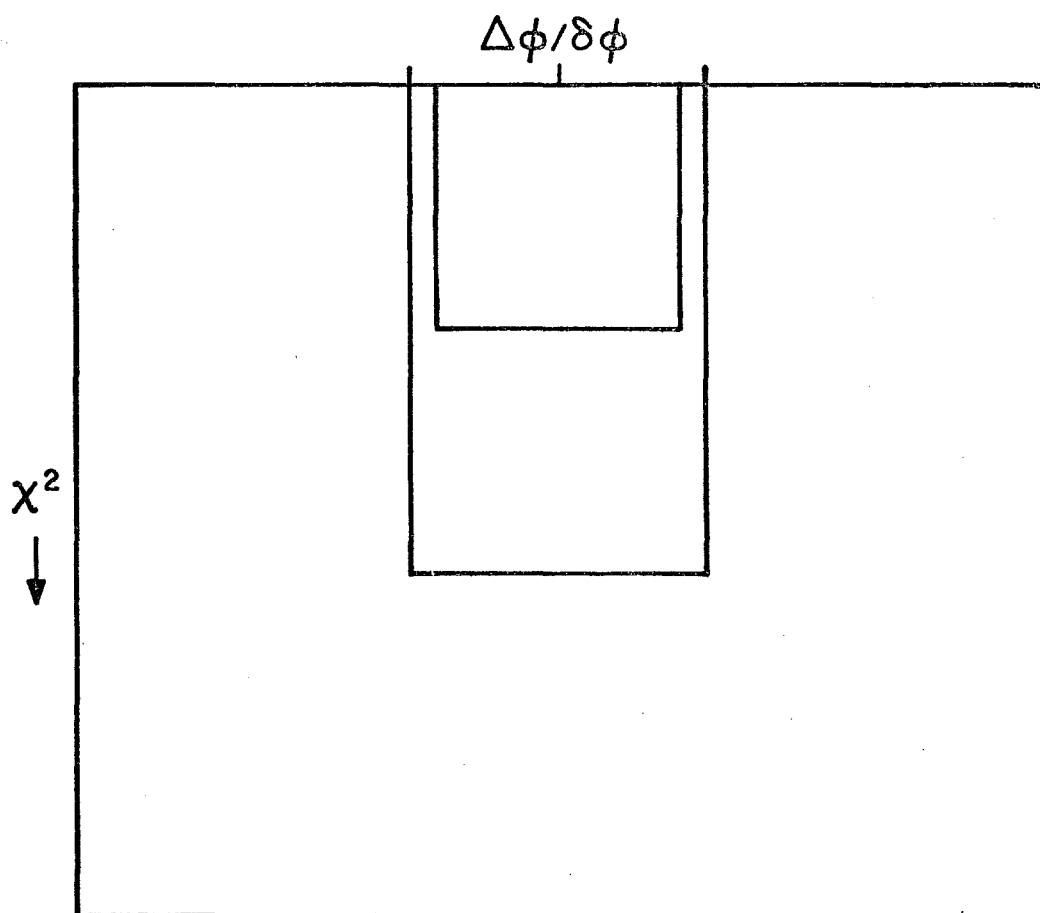
- a) Difference between observed position of forward particle in WS3X and position expected from observed position in other forward chambers. 300 GeV data with t defining counter set at $t = -0.6 \text{ GeV}^2$. The only requirement placed on events for this plot is that there should be tracks present on both arms and a cluster present in WS3X.
- b) Calculated deflection angle of forward going particle in elastic events.



IV. The Summary Program

The summary program processed the second pass tapes produced by the analysis program to obtain histograms of numbers of events versus t in χ^2 - coplanarity space for pions and protons. At the end of each run, pertinent information, principally the scaler data and the number of events in particular regions of the χ^2 - coplanarity plots, were written to a disk file for subsequent processing. Figure III-5 indicates how we defined the signal and background regions.

Figure III-5. Definitions of signal and background regions.



V. The Display Program

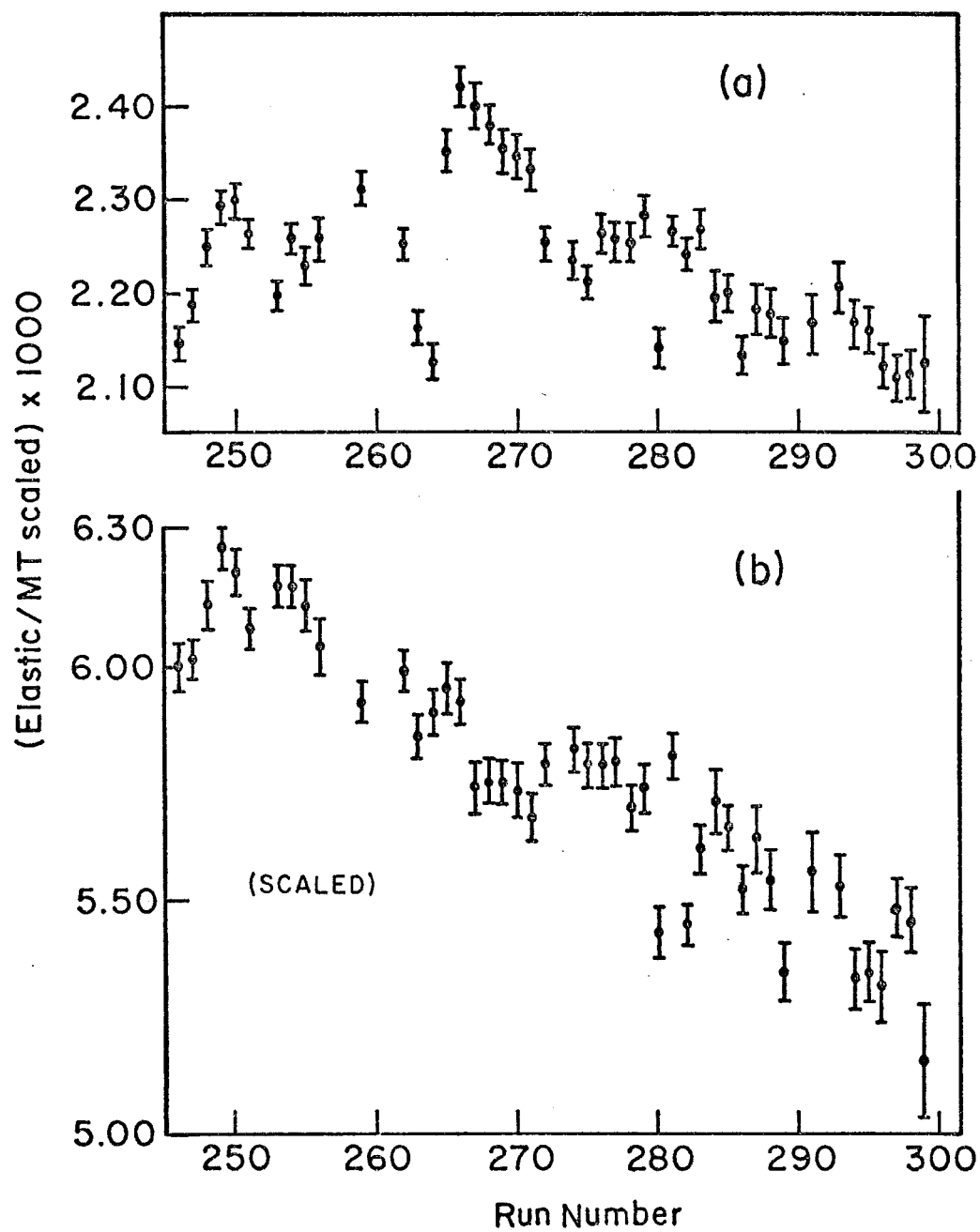
This program, which operated upon the disk file created by the summary program, calculated ratios of scalers and summarized data and displayed these ratios versus run number in a point plot with error bars on the 4012 oscilloscope screen. Typical of the displayed quantities were ratios of beam monitors and ratios of elastic and background events to beam monitors. In Figure III-6a we show one of these plots. This plot, of the ratio of elastic events to our usual beam monitor, indicates the problem we faced in calculating polarizations: the fluctuations of this ratio is much larger than can be explained from statistical error alone. Another way of saying this is that the χ^2 per degree of freedom of the fit of the data to a zero slope straight line is much larger than unity. Thus one justification for the program is that it enabled us to monitor the fluctuations in the data over a series of runs.

The program also enabled us to make various "corrections" to the data, and to see quickly the effect of these corrections. In practice, we assumed that the major effects were rate associated. Consequently, our first attempt to smooth the data was to compensate the elastic events by a factor which depended on the average flux per spill:

$$N_{\text{elastic}}^{\text{corrected}} = N_{\text{elastic}} / (1 - f_{\text{MT}} \Sigma \text{MT} / N_{\text{SPILLS}}) (1 - f_{\text{VT}} \Sigma \text{VT} / N_{\text{SPILLS}})$$

with a similar correction for the number of background events. Recall that VT and MT were defined in Chapter II, section VII.

Figure III-6. a) Plot of the ratio of elastic events to monitors for a subset of the 100 GeV data.
b) Plot of the ratio of elastic events, corrected for average monitors per run, to monitors for the same subset of 100 GeV data.



Since the rate factors f_{MT} and f_{VT} are positive, the higher the flux, the larger the correction. In Figure III-6b we display the ratio of elastic events compensated according to Eq. (5) to beam monitors for the same set of runs.

It is clear that our rate correction of Eq. (5) will be most accurate when the instantaneous flux is constant (and equal to the average flux, i.e. $dMT/dt = \Sigma MT/N_{SPILLS}$, and $dVT/dt = \Sigma VT/N_{SPILLS}$). Unfortunately in most runs this is a poor approximation, and we were obliged to apply the rate correction on a spill to spill basis. We calculated corrected monitors

$$MT' = \sum_{i=1}^{N_{SPILLS}} MT_i (1-f_{MT}^{MT_i}) (1-f_{VT}^{VT_i}) \quad (6a)$$

and

$$VT' = \sum_{i=1}^{N_{SPILLS}} VT_i (1-f_{MT}^{MT_i}) (1-f_{VT}^{VT_i}) \quad (6b)$$

$$F' = MT' + .01*VT' \quad (6c)$$

and compensated the total number of elastic events in the run by

$$N_{elastic}^{corrected} = N_{elastic} / (F'/F) \quad (7)$$

We chose to apply this correction instead of compensating the number of elastic events directly partly for convenience and partly to avoid round-off error in the programs ($N_{elastic}$ is an integer).

It is worth noting that this compensation of elastic events defined by Eqs. (5-7) is not entirely ad hoc, even though the rate factors f_{MT} and f_{VT} were determined empirically. First, at sufficiently low flux, the dead time (during which elastic triggers will not be recorded) and the number of times non-elastic reactions will fire veto counters (and thereby prevent elastic events from being recorded) will be proportional to beam flux. To the extent that the assumption of beam stability mentioned above is correct, the use of compensated numbers of elastic events is an improvement over the use of the raw numbers. A corollary of our claim that the compensation can be physically justified is that we should be able to calculate the rate factors, and in fact our estimates are fairly close to the numbers we have determined empirically. A second point is that these factors remain nearly constant over the entire set of data runs; thus the rate factors used to compensate the 100 GeV data with 400 GeV primary were the same used to compensate the 300 GeV with 300 GeV primary. Third, the χ^2 for the fits of the ratios to straight lines were rather stable with respect to variation of the rate parameters; the χ^2 varied only slightly with 10-20% variations of the parameters, but increased rapidly with larger changes in the parameters. We selected our rate factors to be in the center of this χ^2 plateau.

From the two plots of Figure III-6 it is clear that while we have smoothed the ratios of elastic events to beam monitors considerably by compensating for rate effects, these corrections are not sufficient to enable us to calculate polarizations with

any confidence. The problem is evident in the figure: while the ratio is constant within statistical errors for any small set of consecutive runs, there are long term drifts in the ratios which will lead to spurious asymmetries. We chose to deal with these drifts by dividing the data into sets of consistent runs, compensating each run to remove the effect of the drift, and calculating a total error on the ratio which included both the statistical error and an estimated systematic error.

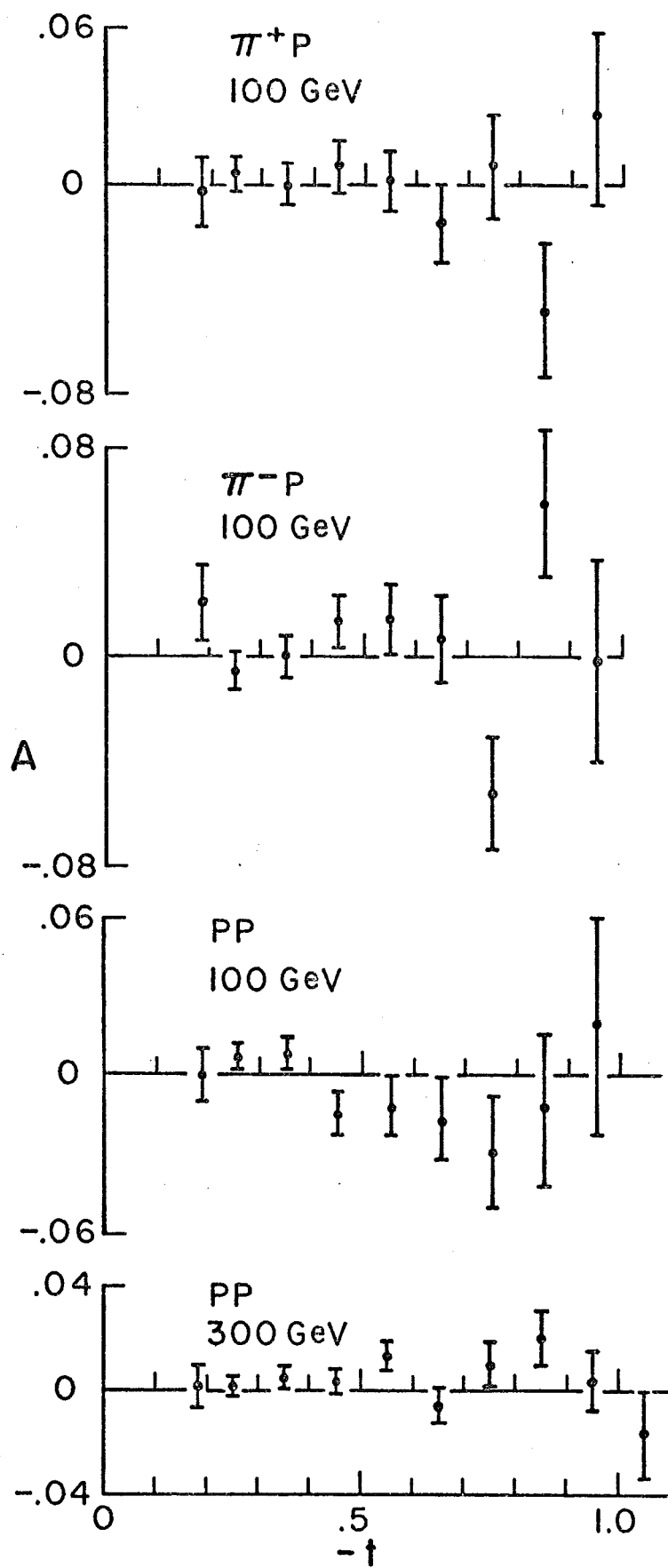
Each set was determined by examining plots such as Figure III-6b. The principal requirements were that there should be a reasonable number of runs in the set (at least 20), that the run to run fluctuations within the set should be not much larger than expected from statistical error, and that all runs within the set should lie on a straight line (not necessarily with zero slope). The compensation was determined by finding the straight line which best fit the set of data, and then correcting each ratio to remove the slope:

$$R'_i = R_i - \text{slope} * (i - i_0) \quad (8)$$

with R the ratios, i the run number, and i_0 the run number at the center of the set. Finally, the error was determined as follows: determine the χ^2 for the least squares fit to the ratio for a particular enhancement. If ϵ_{STAT} is the fractional statistical error, then we can define an approximate total error as

$$\epsilon_{\text{TOT}}^2 = \epsilon_{\text{STAT}}^2 \chi^2 / N_f \quad (9)$$

Figure III-7. Background asymmetries.



Thus if the systematic error is much smaller than the statistical error, we obtain

$$\chi^2/N_f \approx 1 \quad (10)$$

and

$$\epsilon_{\text{TOT}}^2 = \epsilon_{\text{STAT}}^2 \quad (11)$$

Otherwise the extent to which the χ^2/N_f differs from unity indicates how much larger the total error is than the statistical error. We can also define a systematic error, ϵ_{SYS} , as

$$\epsilon_{\text{SYS}}^2 = \epsilon_{\text{TOT}}^2 - \epsilon_{\text{STAT}}^2 = \epsilon_{\text{STAT}}^2 (\chi^2/N_f - 1) \quad (12)$$

The fractional error on the ratio of the number of events within a given t bin to monitors is then obtained by adding in quadrature the fractional statistical error on the ratio together with the systematic error as determined above (on the entire sample).

The same procedure can be applied to the background events, which we expect to be mostly from quasi-elastic reactions. In Figure III-7 we display background asymmetries, calculated as described above. There is no evidence for any polarization of the background, except in the 300 GeV data, for which the background asymmetry as a whole is 0.005 ± 0.002 . We mention that this asymmetry is seen in all subsets of the 300 GeV data. We have attempted to understand this in several ways. First, this asymmetry was not the result of our rate corrections; if we calculate asymmetries without rate corrections, the background

asymmetry is slightly larger. Our next thought was that this asymmetry could be the result of polarization in some sample of the data which we had classified as background. We checked this in two ways, first by making our definition of background as stringent as possible, in the hope of eliminating all but quasi-elastic scatters, and second by calculating asymmetries in different regions in χ^2 -coplanarity space (see Figure III-5 for our definition of background). Neither of these changes had a consistent effect: the asymmetries decreased in some samples of data, and remained roughly constant in others.

Our final thought was that the number of quasi-elastic scatters could in fact be asymmetric with respect to target polarization, if the level of He^3 around the target varied systematically with target polarization. We tested this hypothesis by calculating asymmetries in the upper and lower halves of the target, with the same results as before: both halves of the target showed the asymmetry.

Our feeling about this residual asymmetry is that it affects only the background (i.e. is not a monitor problem, so that our polarizations are correct as calculated), partly because polarizations at small t calculated by normalizing to background would be strikingly different from what is seen at all other energies. Nonetheless, in view of our inability to resolve this uncertainty, we assign an additive systematic error of 0.005 to our polarizations at 300 GeV, i.e. we allow the polarization scale to shift up or down within ± 0.005 .

VI. The Polarization Program

The polarization program calculated polarizations according to the standard form

$$P(t) = \frac{\Sigma_{\text{elastics}} (+) - \Sigma_{\text{elastics}} (-)}{\Sigma_{\text{monitors}} (+) - \Sigma_{\text{monitors}} (-)} + P_T^+ \frac{\Sigma_{\text{signal}} (+)}{\Sigma_{\text{monitors}} (+)} + P_T^- \frac{\Sigma_{\text{signal}} (-)}{\Sigma_{\text{monitors}} (-)} \quad (13)$$

where +/- refers to target polarization, signal refers to elastic events with background subtracted, and P_T is the average target polarization. Ratios of "signal" and "elastic" events to the monitors are compensated within each set as discussed in the previous section. We calculated a fractional systematic error on the ratio of the number of elastic events to monitors as described in the previous section, a fractional statistical error on each t bin, $\epsilon_{\text{STAT}}(t)$, and calculated an approximate total error for the polarization,

$$\delta P(t) = (1/P_T) (\Sigma \text{ elastics} / \Sigma \text{ signal}) \sqrt{\epsilon_{\text{STAT}}^2(t) + \epsilon_{\text{SYS}}^2} \quad (14)$$

The sources and relative sizes of errors contributing to the total calculated error on the polarizations are summarized in Table III-1. As with the display program, the input for the polarization program was the disk file created by the summary program.

Table III-1

Sources and Sizes of Errors Quoted on
Polarization Data

Source of Error	Kind of Error	Size of Error
1. Statistical uncertainty	Statistical, adds in quadrature	0.20% at $t=-0.2$ 10% at $t=-1.2$
2. Systematic fluctuations	Systematic, adds in quadrature	0.50% at all t
3. Uncertainty in target polarization	Systematic, multiplies scale	5% at all t
4. Difference between monitor and background normalizations	Systematic, adds linearly to scale	0.50% at all t

RESULTS AND CONCLUSIONS

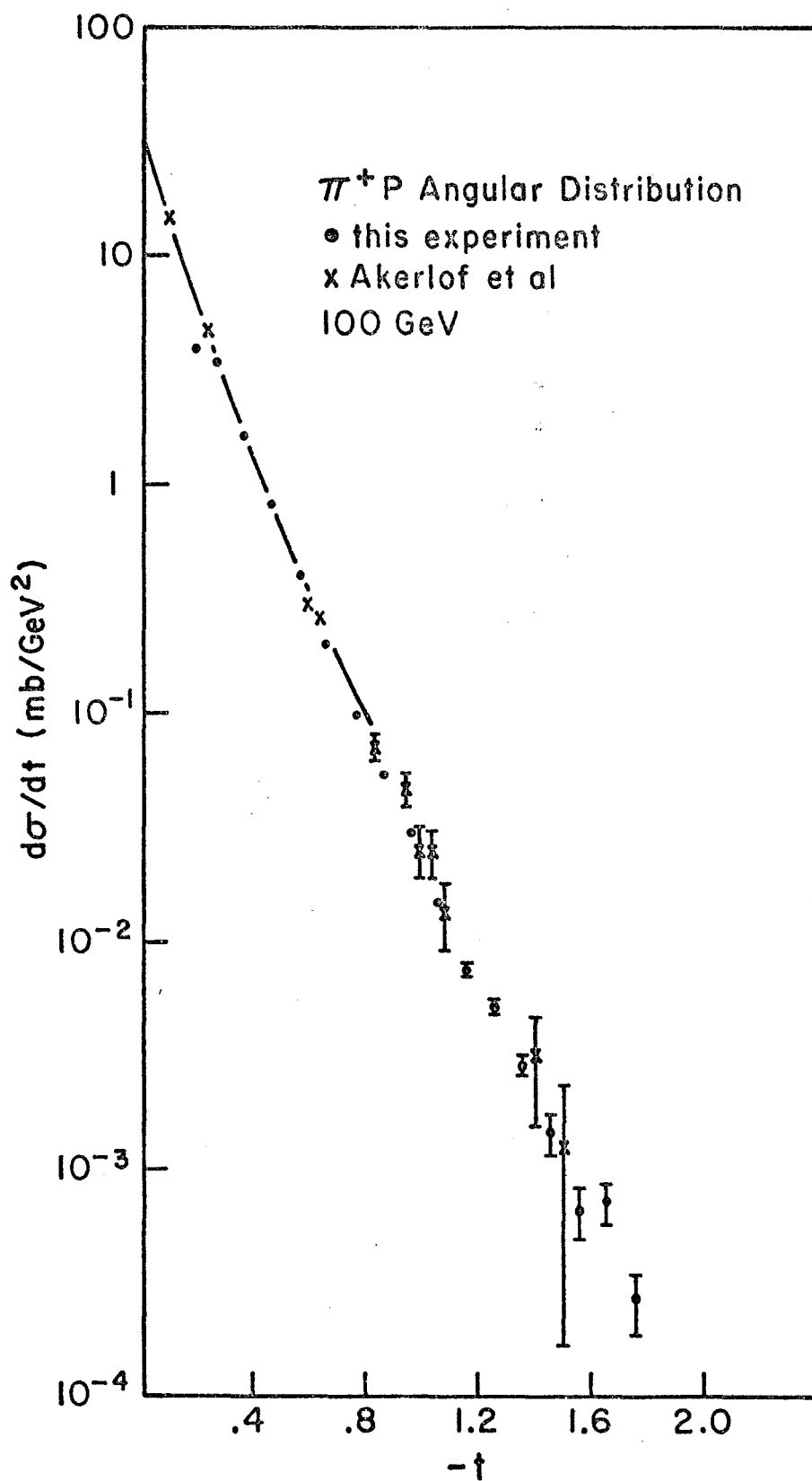
I. π P Scattering

We present our results for π^+ P scattering angular distributions in Table IV-1 and polarizations in Table IV-2, and our results for π^- P angular distributions in Table IV-3 and polarizations in Table IV-4. In Figure IV-1 we show our angular distributions plotted with previously reported results from Fermilab,¹ and in Figure IV-2 show our polarizations for both reactions, together with an extrapolation of data² at 10 GeV to our energy according to s^Δ , with $\Delta = -0.5 + .9t$. Generally speaking, there are no surprises; our angular distributions are in qualitative agreement with previous measurements, and the polarizations at low t still show the approximate mirror symmetry observed at lower energies. Note also the qualitative agreement between the scaled 10 GeV data and our data at small t ; this indicates that the energy dependence of our data is consistent with Regge behavior of the polarization. Theoretically, this puts a limit on the isosingle helicity flip contribution - i.e. the f , and in some models, a "diffractive" piece - since the polarization is approximately given by

$$P(\pi^\pm P) \sim \text{Im } N(I=0) \text{Re} \{ F(I=0) + F(I=1) \} \quad (1)$$

where N and F denote helicity non-flip and flip amplitudes, and I denotes isospin. It is somewhat interesting to note that our data is consistent with Regge behavior for this isosinglet piece (albeit within large error bars), consistent with polari-

Figure IV-1. Angular distributions for πp scattering at 100 GeV. Data from this experiment and Ref. 1; solid curve from Ref. 1.



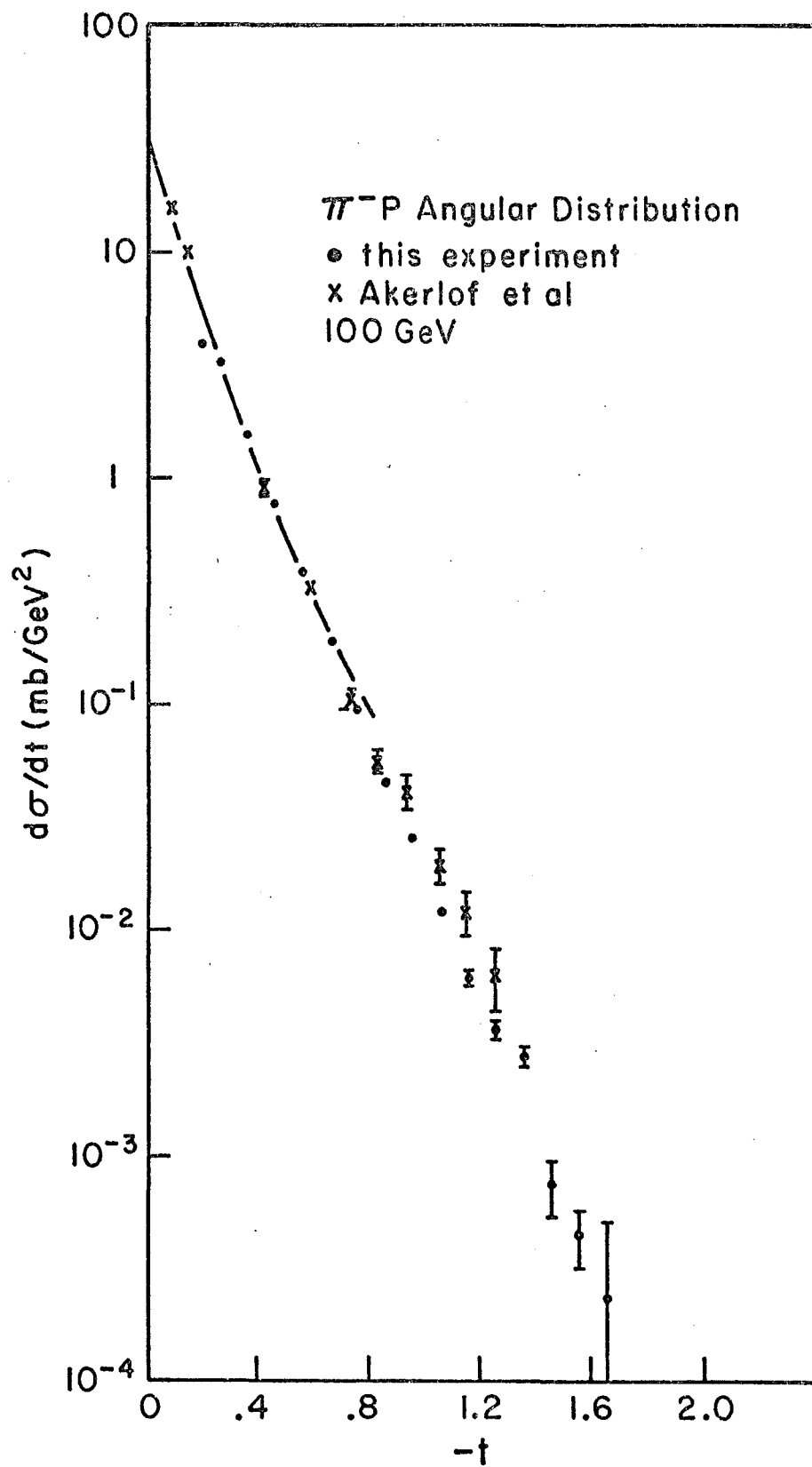


Figure IV-2. Polarizations for πp scattering at 100 GeV.
Data is from this experiment.

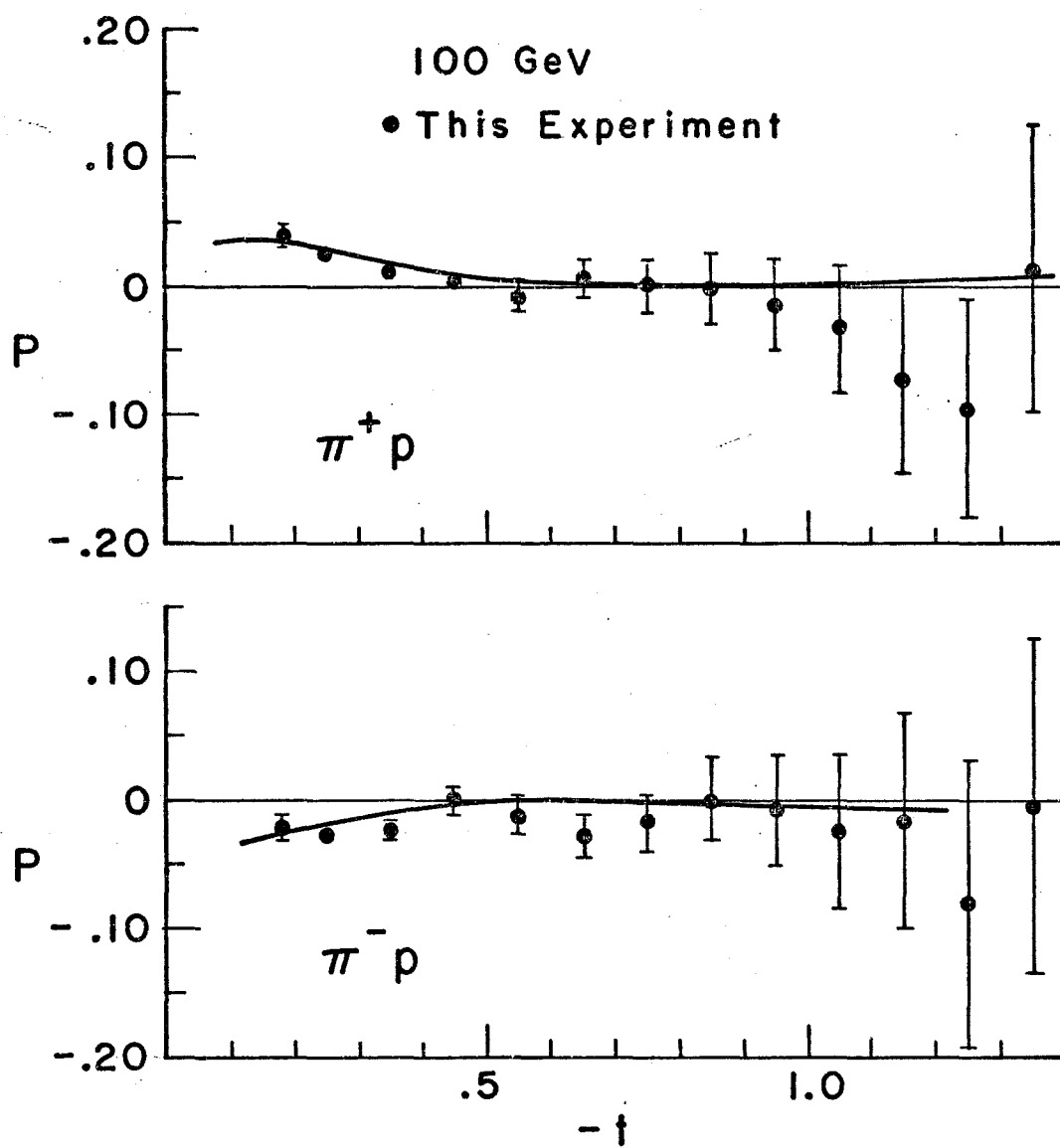


TABLE IV-1

 π^+p Angular Distributions

100 GeV/c

$-t$	$N(t)$	$\delta N(t)^{13}$
0.18	178879	1074
0.25	151062	505
0.35	73260	339
0.45	36405	236
0.55	18283	164
0.65	8949	115
0.75	4271	80
0.85	2400	58
0.95	1327	42
1.05	666	30
1.15	339	22
1.25	231	18
1.35	128	13.5
1.45	65	9.7
1.55	29.5	7.5
1.65	32.4	6.1
1.75	12.0	3.6

TABLE IV-2

 π^+P Polarizations

100 GeV/c

$-t$	$P(t)$	$\delta P(t)^{13}$
0.18	0.0374	0.0074
0.25	0.0247	0.0049
0.35	0.0091	0.0061
0.45	0.0030	0.0080
0.55	-0.0085	0.0106
0.65	0.0053	0.0147
0.75	-0.0014	0.0205
0.85	-0.0042	0.0272
0.95	-0.0161	0.0365
1.05	-0.0348	0.0506
1.15	-0.0768	0.0700
1.25	-0.0967	0.0848
1.35	0.0116	0.1116

TABLE IV-3

 π^- P Angular Distributions

100 GeV/c

$-t$	$N(t)$	$\delta N(t)^{13}$
0.18	142653	895
0.25	120704	455
0.35	58557	305
0.45	28284	209
0.55	14373	147
0.65	6937	101
0.75	3487	67
0.85	1688	47
0.95	948	35
1.05	446	24
1.15	227	18
1.25	135	13
1.35	102	11
1.45	27.5	7.9
1.55	16.4	4.9
1.65	8.7	10.3
1.75	2.2	9.4

TABLE IV-4

 π^- P Polarizations

100 GeV/c

$-t$	$P(t)$	$\delta P(t)^{13}$
0.18	-0.0225	0.0094
0.25	-0.0278	0.0069
0.35	-0.0241	0.0080
0.45	-0.0013	0.0099
0.55	-0.0138	0.0126
0.65	-0.0292	0.0170
0.75	-0.0180	0.0232
0.85	0.0007	0.0324
0.95	-0.0082	0.0428
1.05	-0.0253	0.0611
1.15	0.0176	0.0845
1.25	-0.0817	0.1111
1.35	-0.0068	0.1286

zation data at energies up to 20 GeV, and thus we do not support the tentative identification of non-Regge behavior in the Serpukhov data.³

To test the sensitivity of Regge phenomenology to our data we have chosen, among many models of strong interaction physics, the model of the Michigan school as described in recent review article by G. Kane and A. Seidl in Reviews of Modern Physics.⁴ This model appealed to us for several reasons. First, the authors have attempted to describe in a unified fashion all of high energy two body hadron physics in which the nuclear force is generated through meson exchange. Variations in the parametrization of the model from reaction to reaction occur only when dictated by the underlying physics. Second, this model appeared to be among those most closely connected to Regge pole phenomenology, and not simply a fit of some complicated function or functions to published data. Third, the model appeared to correlate an immense amount of disparate experimental data, much of it not easily described by pure pole models. Finally, and apart from any questions of physics, the model is among the most explicitly described in the literature.

Technically, the Michigan model is a strong absorption model with no nonsense wrong signature zeros (i.e. at $\alpha=0$) in the residues; apart from phase zeros, all zeros in the amplitude are the results of absorption. This is in contrast to the pole model of Chapter I and e.g. the absorption model of Field and Stevens.⁵ Thus strong exchange degeneracy is not automatic in

the model; it is interesting that the parameters which fit the data are approximately exchange degenerate. Amplitudes for the reaction $a + b \rightarrow c + d$ are generated in s and t according to a minor variation of the usual Regge prescription

$$R_{\lambda_c \lambda_d; \lambda_a \lambda_b}^r(s, t) = \frac{1}{2}(-t)^{\frac{n+x}{2}} \gamma_{acr}(t) \gamma_{bdr}(t) \\ r^{\left\{\frac{(\alpha_r - J)}{2}\right\}} (s/s_0)^{\alpha_r} \exp\left\{-\frac{i\pi}{2} (\alpha_r - J)\right\}$$

with λ_i the helicities, n the net helicity flip, x the sum of the flips at each vertex, and J the spin of the lowest lying particle on the trajectory α_r . These "bare" amplitudes are transformed to impact parameter space where they undergo absorptive rescattering via Pomeron and f exchange, and are finally transformed back to t space. This process is carried out exactly as outlined in Chapter I.

Diffraction scattering - in Regge language, Pomeron exchange - is parametrized in a complicated (and rather ad hoc) form by

$$P(s, t) = -is A_c e^{B_c t} R_c^2 J_1(R_c \sqrt{-t}) / R_c \sqrt{-t} \\ - is A_e e^{B_e t} R_e^2 J_0(R_e \sqrt{-t})$$

intuitively justified as the form of scattering in impact parameter space from a potential which is the sum of a hard edge disk and a peripheral ring. Shrinkage of forward elastic peaks is parametrized by taking the radii R_i^2 to be

linear in $\log(s)$. Observables such as the differential cross-section and the polarization are then calculated in the usual way with the absorbed Regge amplitudes and the Pomeron. Taking our case of πP scattering as an example, we find that the three allowed exchanges are the f and p Regge trajectories and the Pomeron; thus we calculate all observables by forming helicity amplitudes

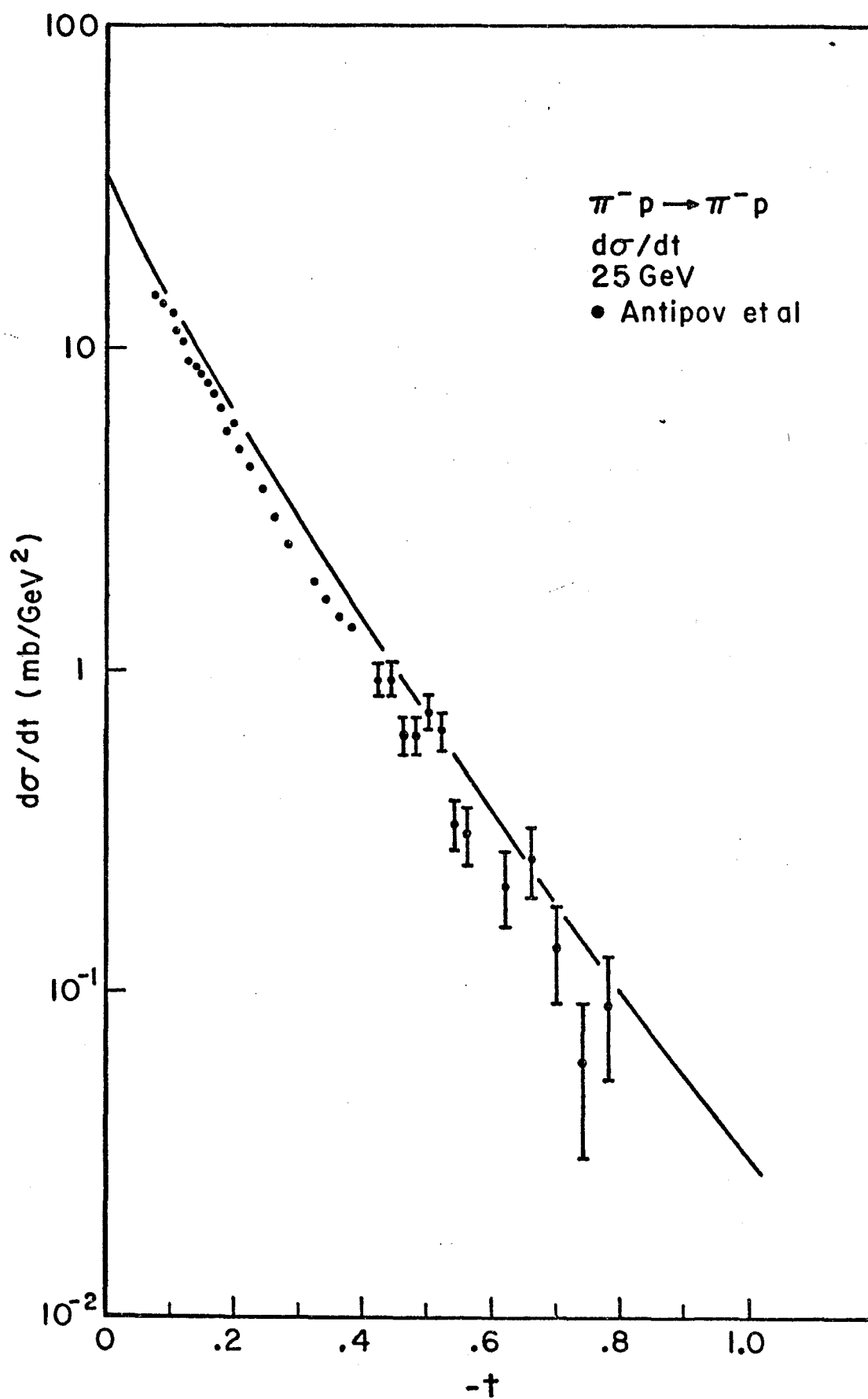
$$N = P + \tilde{f}_{++} + \tilde{\rho}_{++} \quad (4a)$$

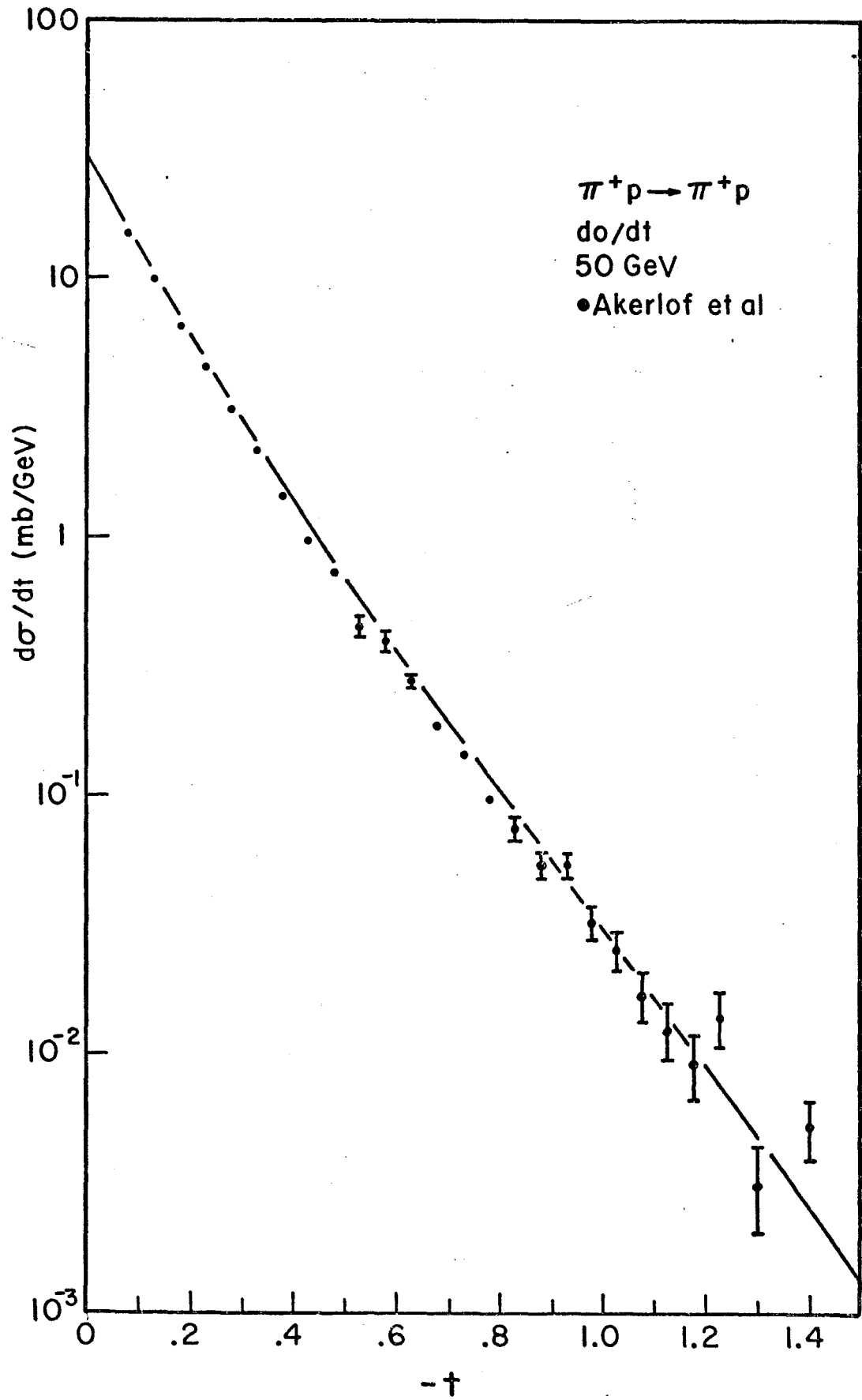
$$F = \tilde{f}_{-+} + \tilde{\rho}_{-+} \quad (4b)$$

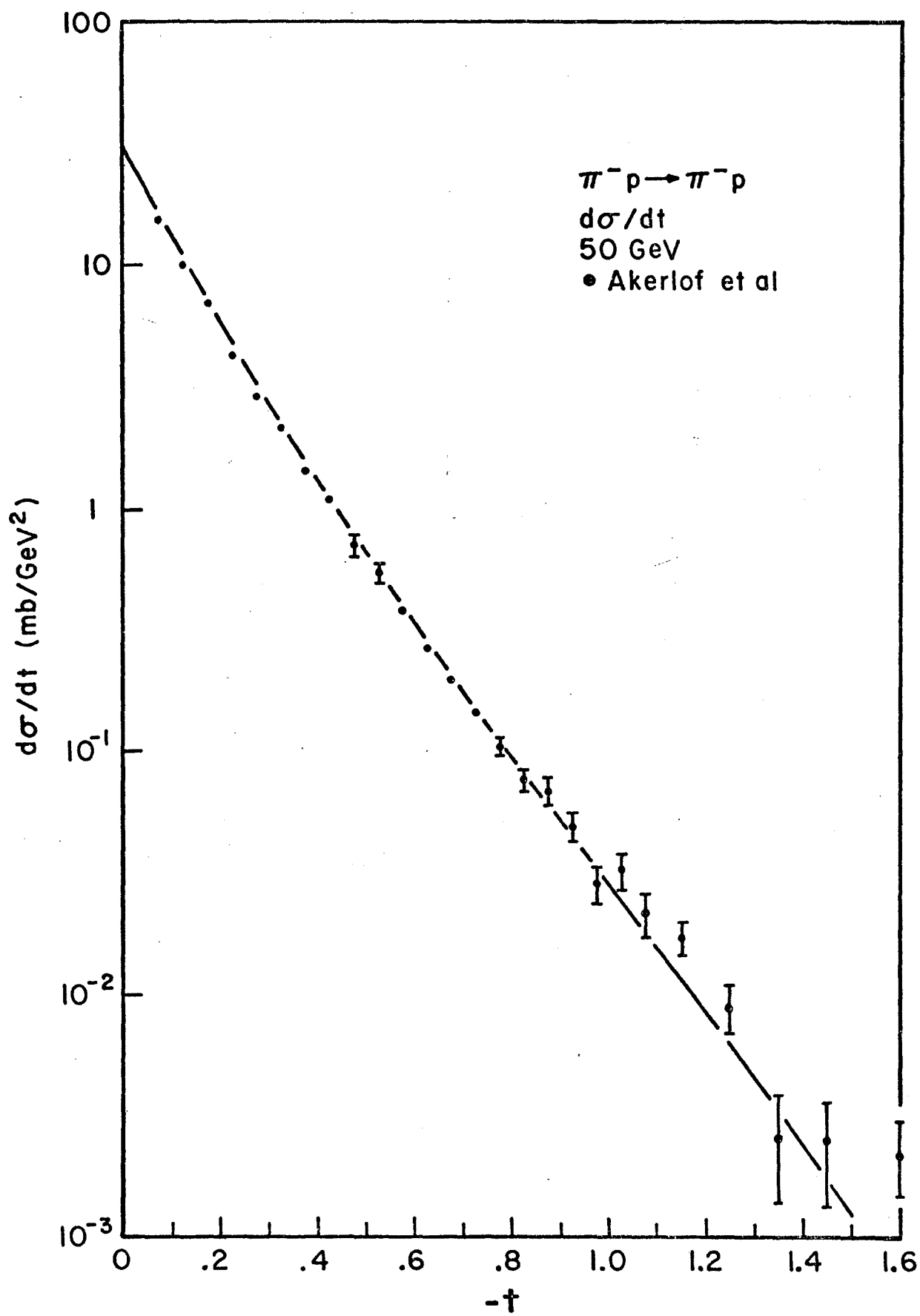
where the tilde indicates an absorption corrected amplitude. We have collected in Appendix I all of the formulae needed to calculate amplitudes; reference 4 contains a detailed exposition of the model.

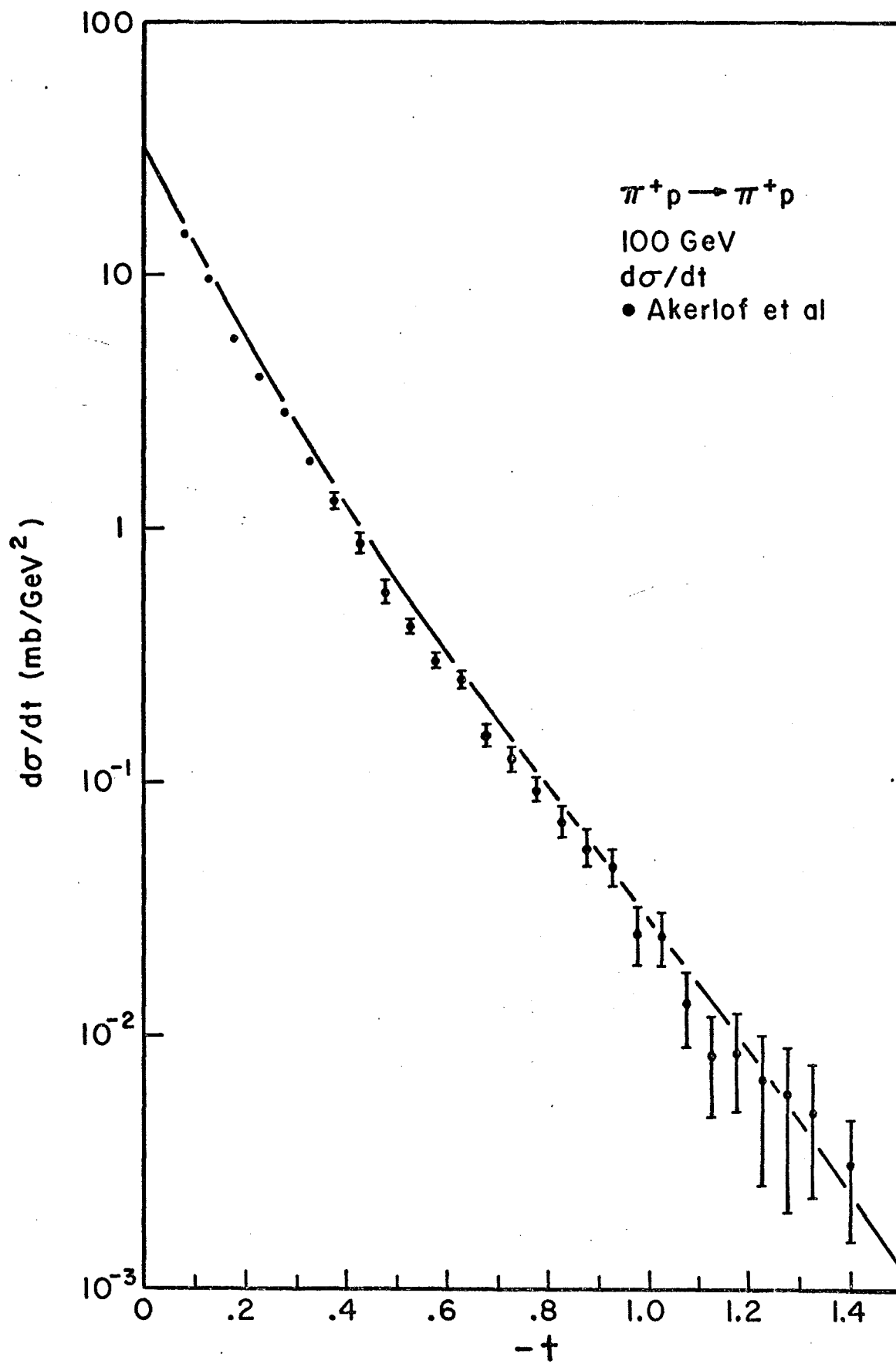
We give differential cross-sections at various energies for πP scattering, together with predictions of the model, in Figure IV-3. In Figure IV-4 we give the polarization data at various energies,⁶ including our data at 100 GeV, again with predictions of the model. As can be seen from these two figures, the predictions of the model are in fairly good agreement with the data. Since the model as published fits low energy differential cross-sections, we do not think the disagreement between the 25 GeV differential cross-section data and the model predictions at that energy is significant. It is possibly a result of a slight shift in the t scale of the data; shifting the data by $\Delta t \sim .02 \text{ GeV}^2$ brings the experimental data into line with the model predictions.

Figure IV-3. Differential cross-sections for πp scattering at various energies, with model predictions. 25 GeV data is from Antipov et al., Nucl. Phys. 57B, 333 (1976); higher energy data is from Ref. 1.









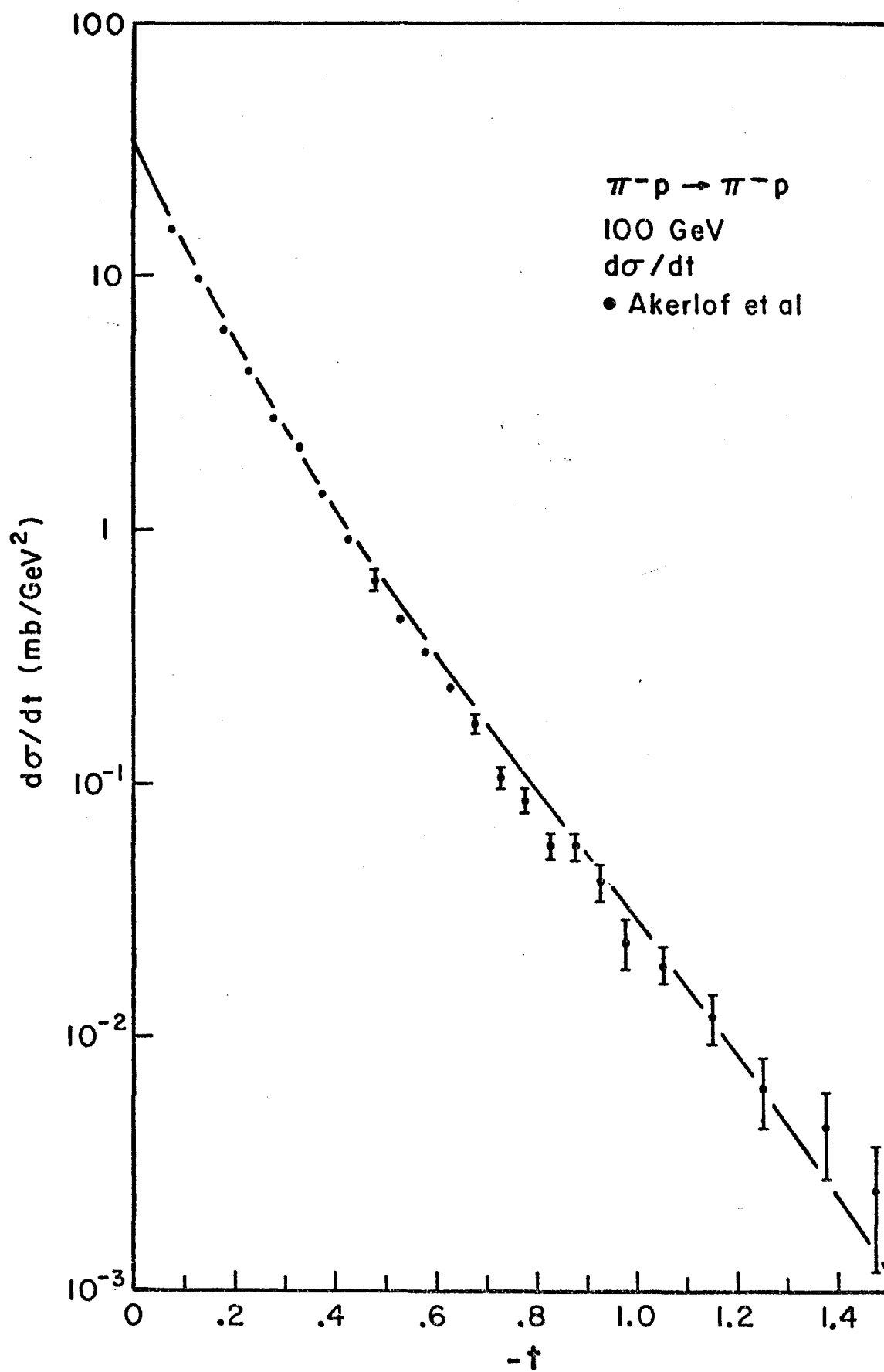
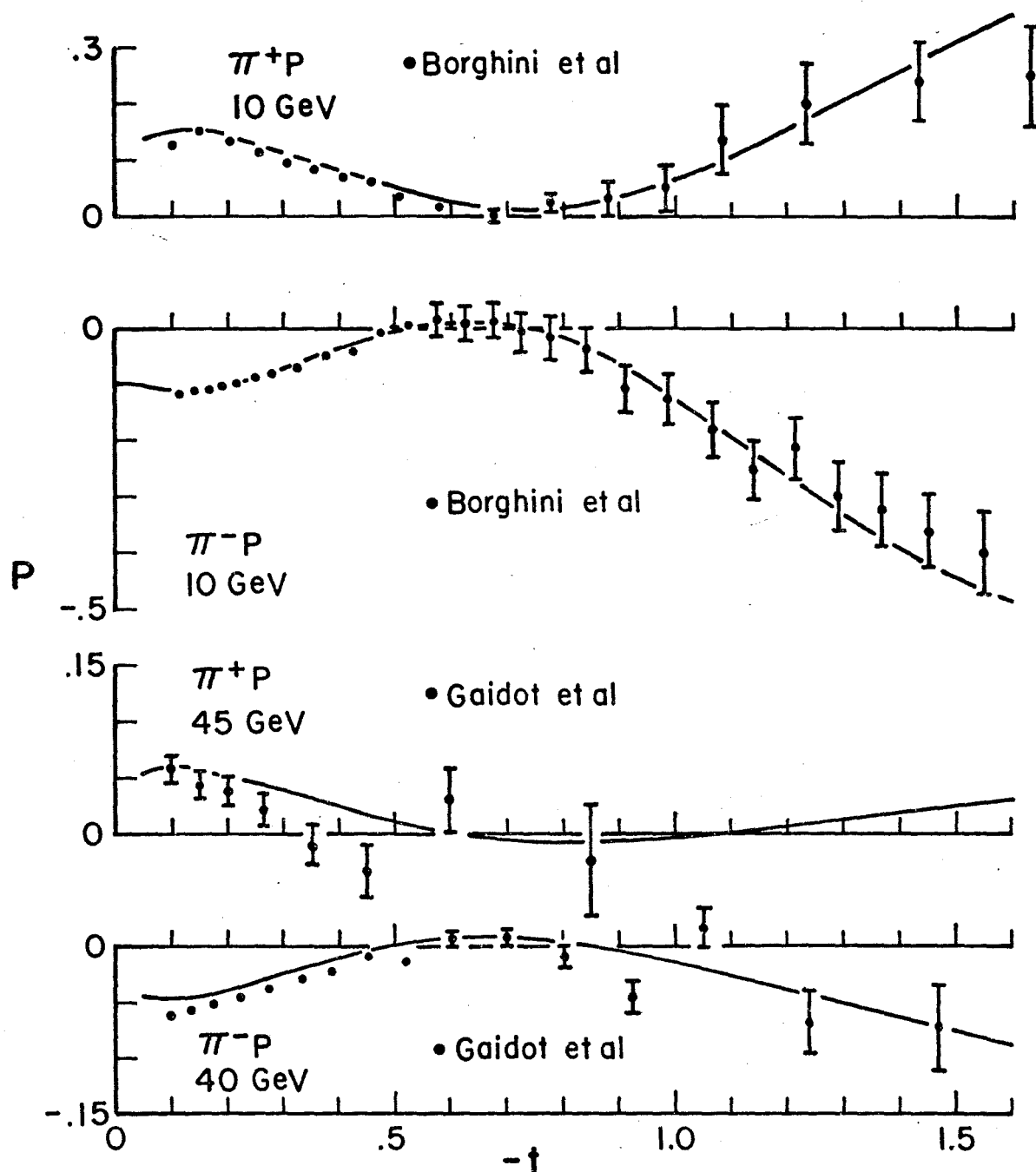
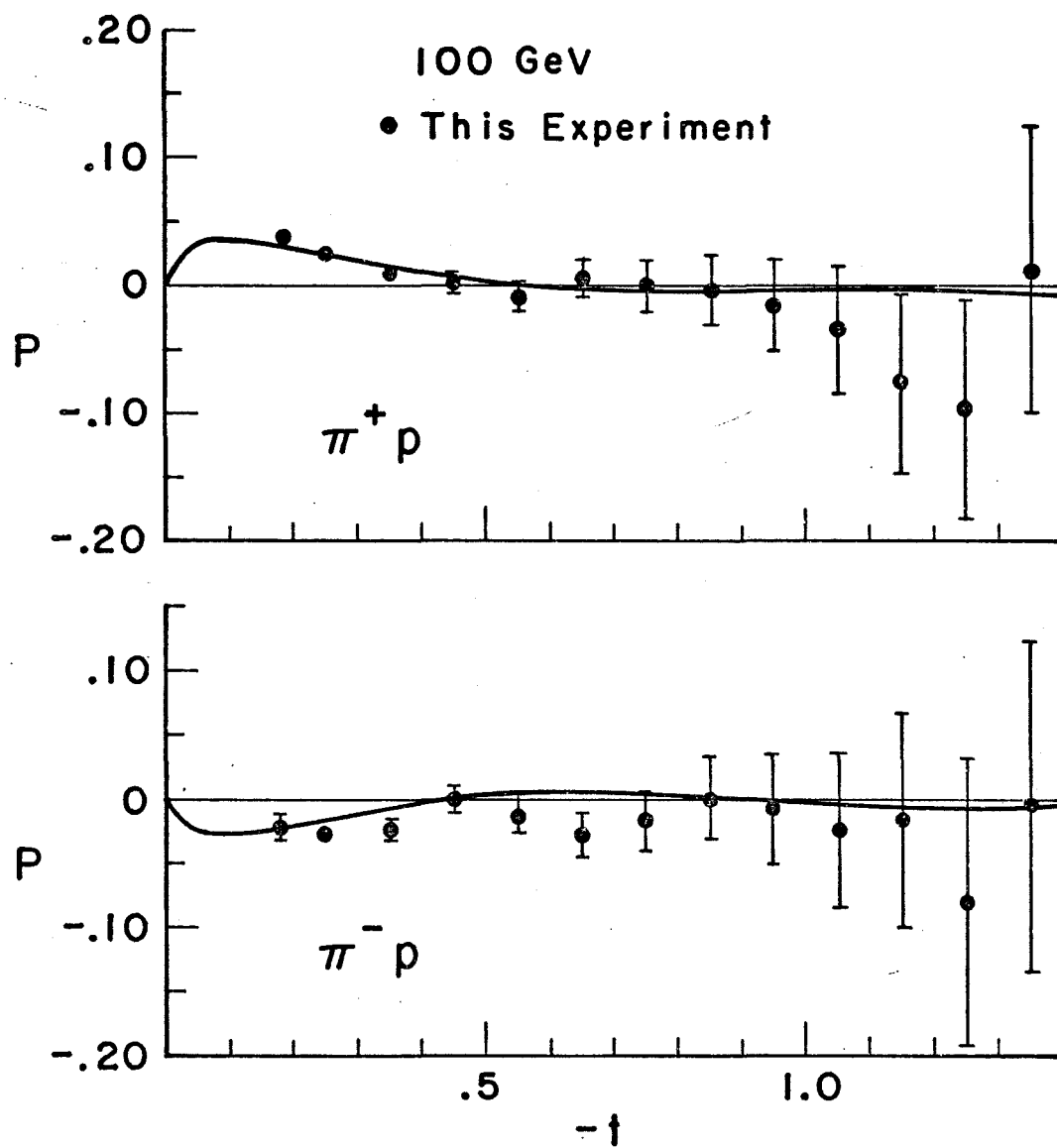


Figure IV-4. Polarizations for πp scattering at various energies, with model predictions. Data at 100 GeV from this experiment, other data from Ref. 6.





In this model, for the kinematic region $-t < 1 \text{ GeV}^2$, the polarization is described as the sum of two terms, $\text{Re } F \times \text{Im } N$ and $\text{Re } N \times \text{Im } F$, both of which are important. The double zeros in the polarization at $t=-0.6$ (see Figure IV-4) are present in both terms at moderate energies - $\text{Re } N$ and $\text{Re } F$ each have a single zero from the parametrization, while both $\text{Re } F$ and $\text{Im } F$ pick up a zero at $t=-0.6$ from absorption. $\text{Im } N$ is smooth and exponentially decreasing to zero for $-t < 1.5 \text{ GeV}^2$. Figure IV-5 illustrates both amplitudes before and after absorption, and shows how the products $\text{Re } F \times \text{Im } N$ and $\text{Re } N \times \text{Im } F$ have double zeros.

One of the most interesting features of πP polarization data is that this double zeros structure seems to be stable with increasing energy. Models with zeros in the residue functions at $\alpha=0$, such as the pole model of Chapter I or the Field and Stevens model, have this energy independence built in. The Michigan model, however, explains this stability in an entirely different fashion. At all energies, $\text{Re } F \times \text{Im } N$ dominates the small t polarizations and in effect forces a positive small t lobe and a zero at $t=-0.6$. For low energies, $\text{Im } F \times \text{Re } N$ dominates the region $0.5 < -t < 1.0 \text{ GeV}^2$, and causes the polarization to increase with increasing $-t$, thus resulting in a second zero. At higher energies, say $P_{\text{LAB}} \sim 20 \text{ GeV}$, the polarization in this region is dominated by $\text{Re } F \times \text{Im } N$, and the nearly coincident zeros in $\text{Re } F$ again put the coincident zeros in the polarization at $t \sim -0.6 \text{ GeV}^2$.

However, at energies between 50 and 100 GeV, the two zeros in $\text{Re } F$ rapidly separate and the double zeros structure in the polarization disappears. Unfortunately from an experimental viewpoint, distinguishing between a model with residue zeros and the present model would require extremely high precision data, since both models predict polarizations on the order of a per cent (of opposite sign) for $0.6 < -t < 1.5 \text{ GeV}^2$ (compare the extrapolated 10 GeV data in Figure IV-2 with the model predictions of Figure IV-4). In principle this would be of considerable theoretical interest for the light it would shed on the question of residue zeros - it is quite difficult for the present model, and by extension other eikonal models, to keep the double zeros structure intact with increasing energies.

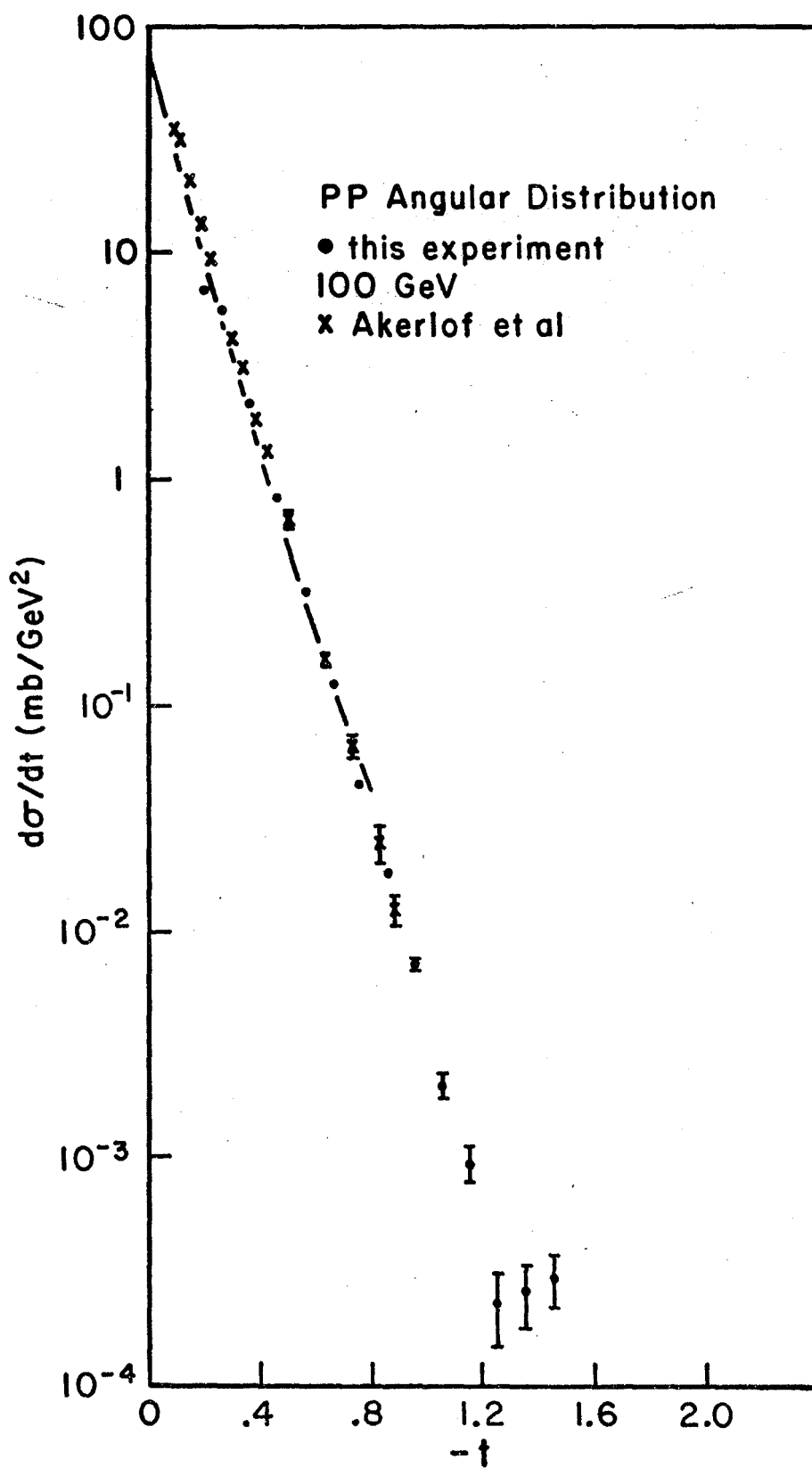
Another interesting prediction of the model which can be more directly explored is the existence of a dip in the differential cross-section around a t of 2.3 GeV^2 , accompanied by a change in the polarization from ~ -0.50 to $\sim +0.75$. This structure arises from a nearby diffraction zero and is exactly comparable to the dip in the pp differential cross-section at $t = -1.4 \text{ GeV}^2$.

II. pp Scattering

We give our results for pp elastic angular distributions in Table IV-5, and our polarizations in Table IV-6. In Figure IV-5 we show our angular distributions at 100 and 300 GeV, plotted with previously reported results from Fermilab⁷ at 100 GeV and from the ISR⁸ at 300 GeV. As in the case of πp scattering our angular distributions are in agreement with the existing data. In Figure IV-6 we plot our polarization data. Since pure pole predictions for pp polarizations have been unsuccessful even at low energies, we have no intuitive explanations for the behavior of the polarization as a function of energy. Instead of giving an intuitive explanation of the structure of the polarization as with the πp data, we compare our data with existing data at lower energies to identify changes in the structure of the polarization with increasing energy, and then compare the data with predictions from the Michigan absorption model.

We first consider the lower energy data. In Figure IV-7 we have plotted pp polarization data⁹ at 6, 10, 14, 17.5, 24, and 45 GeV. At 6 GeV we see a dip around $t = -0.8$, which by 10 GeV has become double zeros. This double zeros structure persists through 17.5 GeV, and the 24 GeV data give some indication that the coincident zeros are still present. By 45 GeV however, the polarization zero has moved in to $t \sim -0.5$ GeV², and at larger t the polarization apparently goes negative.

Figure IV-5. Angular distributions for pp scattering at 100 and 300 GeV. Data from this experiment and from Ref. 1.



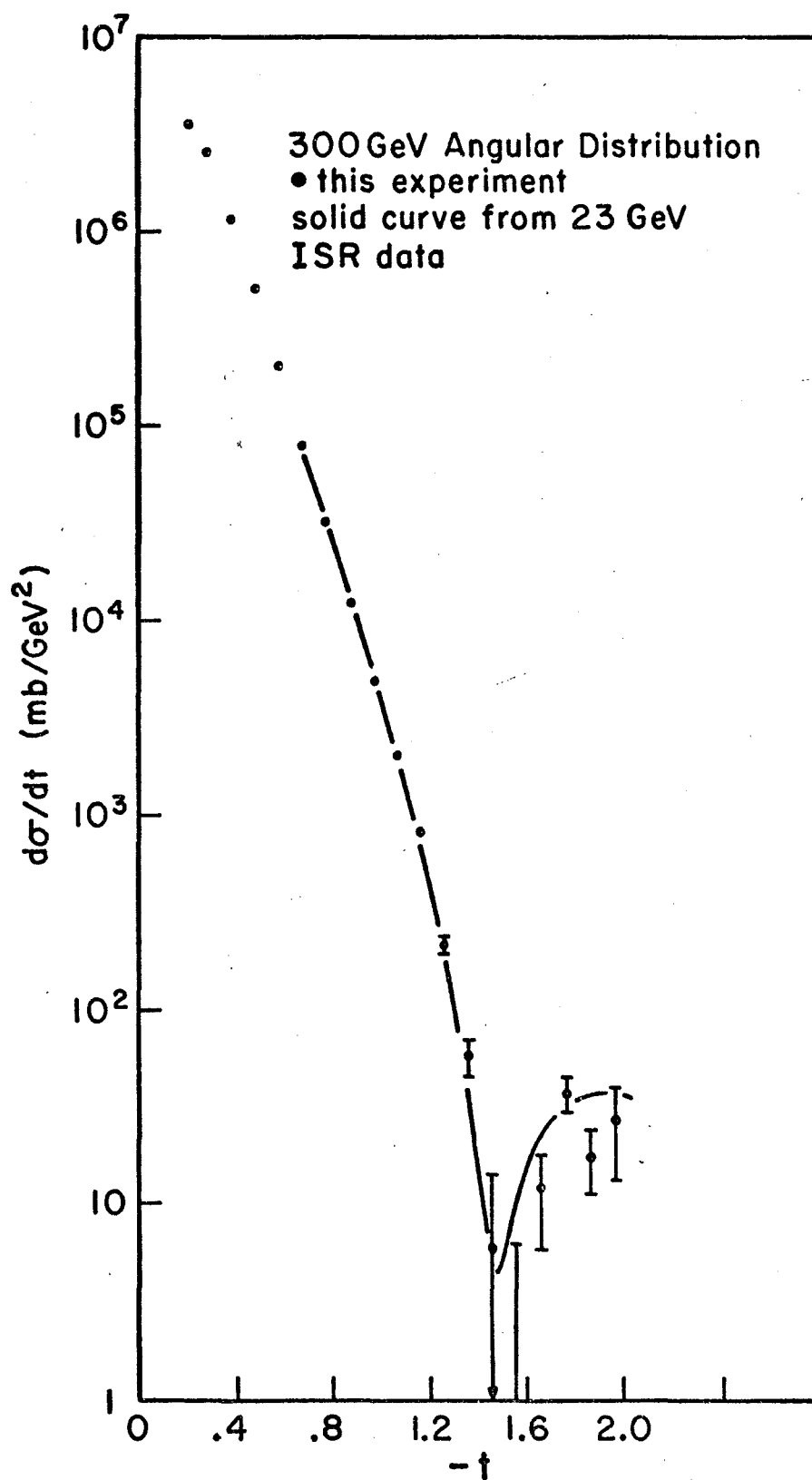
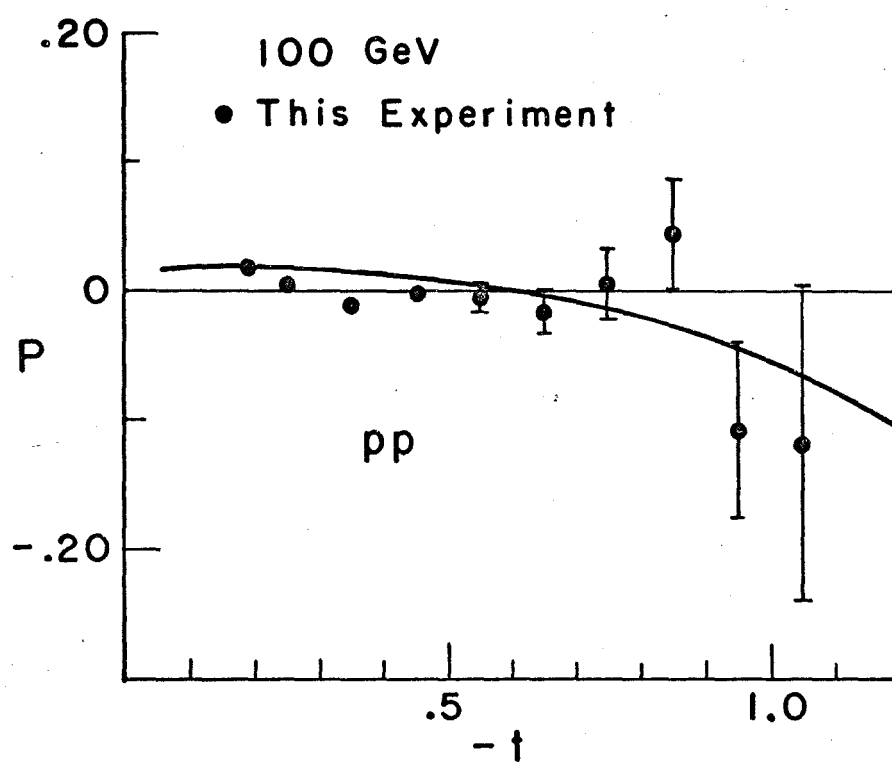


Figure IV-6. Polarizations for pp scattering at 100 and 300 GeV, with model predictions. Data from this experiment.



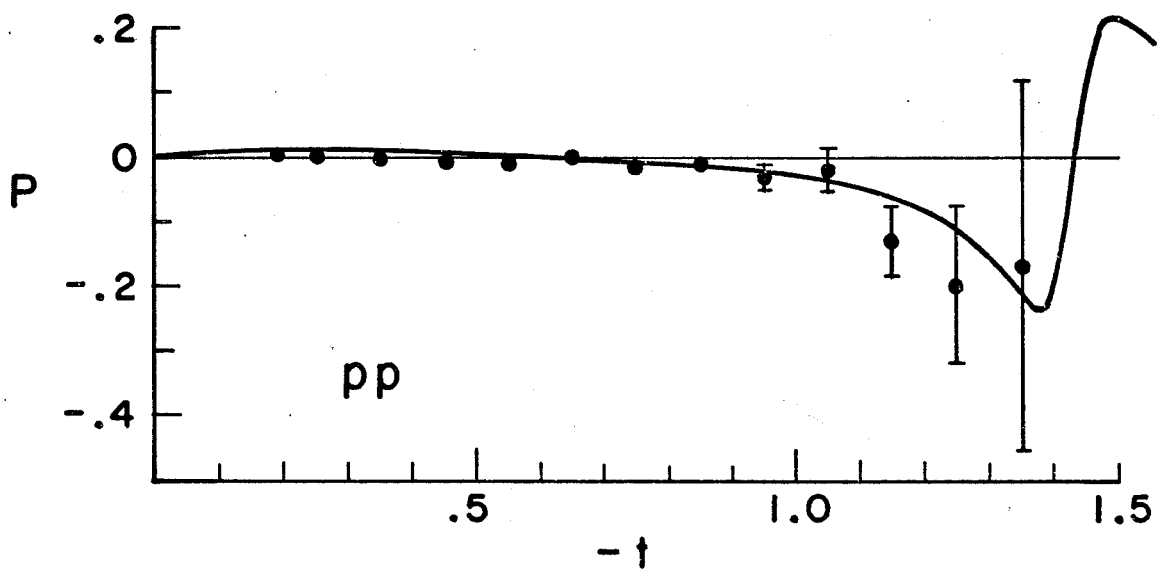
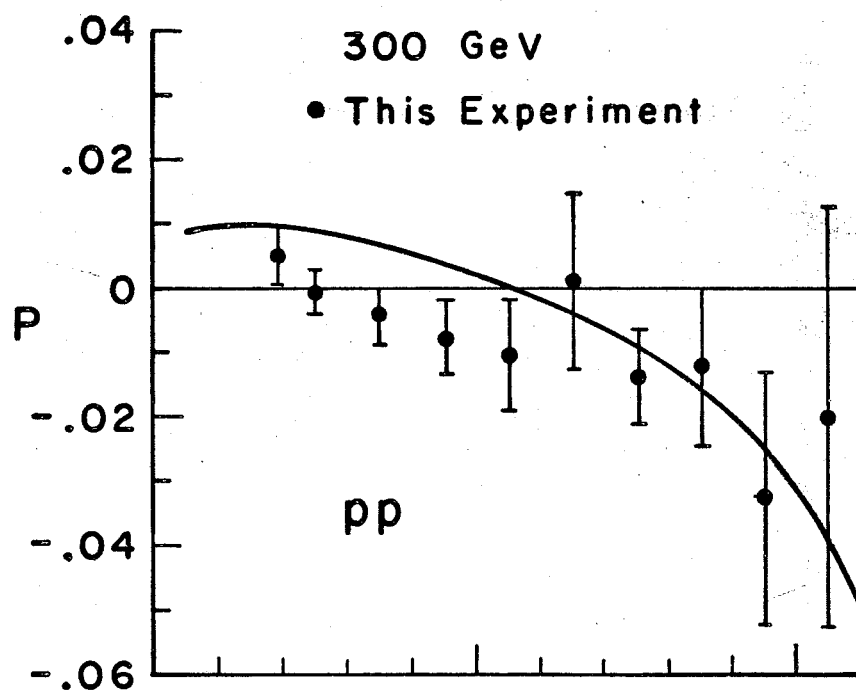


TABLE IV-5

PP Angular Distributions

100. GeV/c

$-t$	$N(t)$	$\delta N(t)^{13}$
0.18	361779	1495
0.25	287736	678
0.35	110747	408
0.45	44075	255
0.55	17585	158
0.65	6507	96
0.75	2369	57
0.85	944	36
0.95	374	22
1.05	108	12.6
1.15	49.7	8.7
1.25	11.7	3.9
1.35	13.4	4.3
1.45	15.3	4.3

PP Angular Distributions

300 GeV/c

$-t$	$N(t)$	$\delta N(t)^{13}$
0.18	3.89×10^6	8.2×10
0.25	2.801×10^6	3.6×10
0.35	1.272×10^6	2.4×10
0.45	0.570×10^6	1.6×10
0.55	0.226×10^6	992
0.65	87.8×10^3	618
0.75	35026	212
0.85	13392	133
0.95	5409	86
1.05	2234	56.6
1.15	907	37.8
1.25	236	22.6
1.35	64	14.6
1.45	6.5	9.0
1.55	0	6.3
1.65	13.2	6.8
1.75	40.9	8.1
1.75	19.2	6.9
1.95	30.0	14.1

TABLE IV-6

PP Polarizations

100 GeV		
$-t$	$P(t)$	$\delta P(t)^{13}$
0.18	.0190	0000058
0.25	.0043	0.0042
0.35	-.0117	0.0054
0.45	-.0025	0.0075
0.55	-.0059	0.0109
0.65	-.0159	0.0170
0.75	.0055	0.0274
0.85	.0431	0.0428
0.95	-.1082	0.0681
1.05	-.1180	0.1289

TABLE IV-6

PP Polarizations

300 GeV/c

$-t$	$P(t)$	$\delta P(t)^{13}$
0.18	0.0051	0.0044
0.25	-0.0008	0.0033
0.35	-0.0043	0.0044
0.45	-0.0078	0.0058
0.55	-0.0104	0.0084
0.65	0.0009	0.0136
0.75	-0.0140	0.0073
0.85	-0.0123	0.0121
0.95	-0.0326	0.0194
1.05	-0.0202	0.0326
1.15	-0.129	0.054
1.25	-0.198	0.121
1.35	-0.167	0.288

TABLE IV-6

PP Polarizations

300 GeV/c

$-t$	$P(t)$	$\delta P(t)^{13}$
0.18	0.0051	0.0044
0.25	-0.0008	0.0033
0.35	-0.0043	0.0044
0.45	-0.0078	0.0058
0.55	-0.0104	0.0084
0.65	0.0009	0.0136
0.75	-0.0140	0.0073
0.85	-0.0123	0.0121
0.95	-0.0326	0.0194
1.05	-0.0202	0.0326
1.15	-0.129	0.054
1.25	-0.198	0.121
1.35	-0.167	0.288

TABLE IV-6

PP Polarizations

3000 GeV/c

$-t$	$P(t)$	$\delta P(t)^{13}$
0.18	0.0051	0.0044
0.25	-0.0008	0.0033
0.35	-0.0043	0.0044
0.45	-0.0078	0.0058
0.55	-0.0104	0.0084
0.65	0.0009	0.0136
0.75	-0.0140	0.0073
0.85	-0.0123	0.0121
0.95	-0.0326	0.0194
1.05	-0.0202	0.0326
1.15	-0.129	0.054
1.25	-0.198	0.121
1.35	-0.167	0.288

TABLE IV-6

PP Polarizations

300 GeV/c

$-t$	$P(t)$	$\delta P(t)^{13}$
0.18	0.0051	0.0044
0.25	-0.0008	0.0033
0.35	-0.0043	0.0044
0.45	-0.0078	0.0058
0.55	-0.0104	0.0084
0.65	0.0009	0.0136
0.75	-0.0140	0.0073
0.85	-0.0123	0.0121
0.95	-0.0326	0.0194
1.05	-0.0202	0.0326
1.15	-0.129	0.054
1.25	-0.198	0.121
1.35	-0.167	0.288

Unfortunately there is no data between 24 and 45 GeV, so we have no way of knowing the details of how the polarization is changing. Also at 45 GeV, the polarization at small t is down to $\sim 2.5\%$, somewhat lower than one might expect on the basis of a pole model with a single exchange degenerate trajectory. Of course, since such a model fails to explain the double zeros, there is no compelling reason to expect it to work at small t .

Our small t data also show a rapidly falling polarization, and like the Serpukhov data, appear to have a zero at smaller t than at lower energies. Also as in the Serpukhov data we see a trend to large negative polarizations with increasing $-t$. As at 45 GeV, there is no indication of the positive second lobe characteristic of the data below 20 GeV at $t \sim 1 \text{ GeV}^2$.

For model predictions we again turn to the absorption model of the Michigan school. In contrast to the predictions of the model in πp scattering, the published predictions of both the pp differential cross-sections and the polarizations did not describe the data accurately. In particular, the dip in the differential cross-sections at ISR energies was too shallow, and was in the wrong place; while the polarizations above 6 GeV were almost a factor of two too large. Finally the model predicted large negative polarizations for $-t$ larger than 0.8 GeV^2 at energies above 14 GeV, in clear disagreement with the 17.5 and 24 GeV data.

To understand to what extent this disagreement was a fundamental failure of the model, and to what extent it was a result of the choice of parametrization, we have implemented the model as described in reference 4, and have tried to obtain predictions more in accord with the data by adjusting various parameters. Our first concern was with the magnitude of the polarizations; we were able to obtain polarizations in rough agreement with the data above 6 GeV by dividing the helicity flip ("tensor") coupling constants of the dominant f and A_2 trajectories in half. This improved the magnitude of the small t polarizations above 6 GeV at the expense of flattening out the dip at 6 GeV.

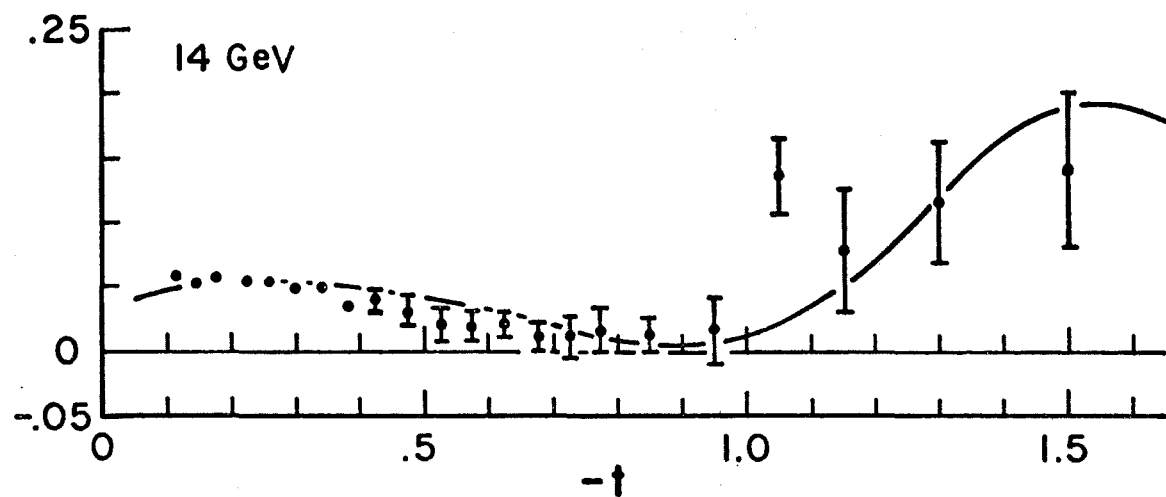
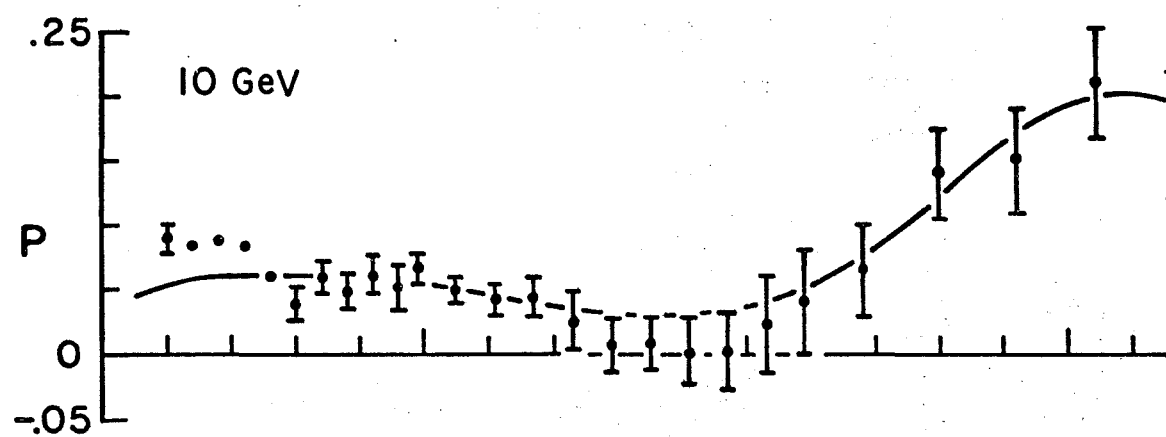
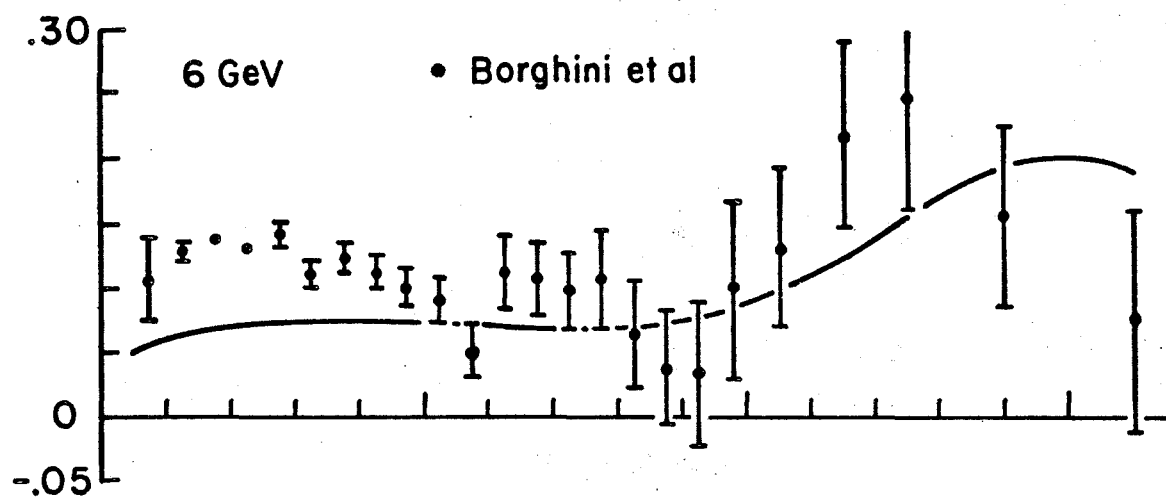
Our next concern was for the position and depth of the dips in the differential cross-sections at ISR energies. We consider these data particularly important because the Regge amplitudes are much smaller relative to the Pomeron at these energies than at lower energies, so that these data determine the form of the Pomeron in Eq. (3). The relevant parameters are the radii

$$R_c^2 = R_{c0}^2 + R_{c1}^2 (\log(s) - i\pi/2) \quad (5a)$$

$$R_e^2 = R_{e0}^2 + R_{e1}^2 (\log(s) - i\pi/2) \quad (5b)$$

the coupling constants A_c and A_e , and the helicity non-flip ("vector") coupling constant for the dominant Regge contribution, the f . Apart from the differential cross-section data, the experimental data which constrain these parameters are the total cross-section,¹⁰ related to the imaginary part

Figure IV-7. Polarizations for pp scattering at various energies with model predictions. Data from Ref. 9.



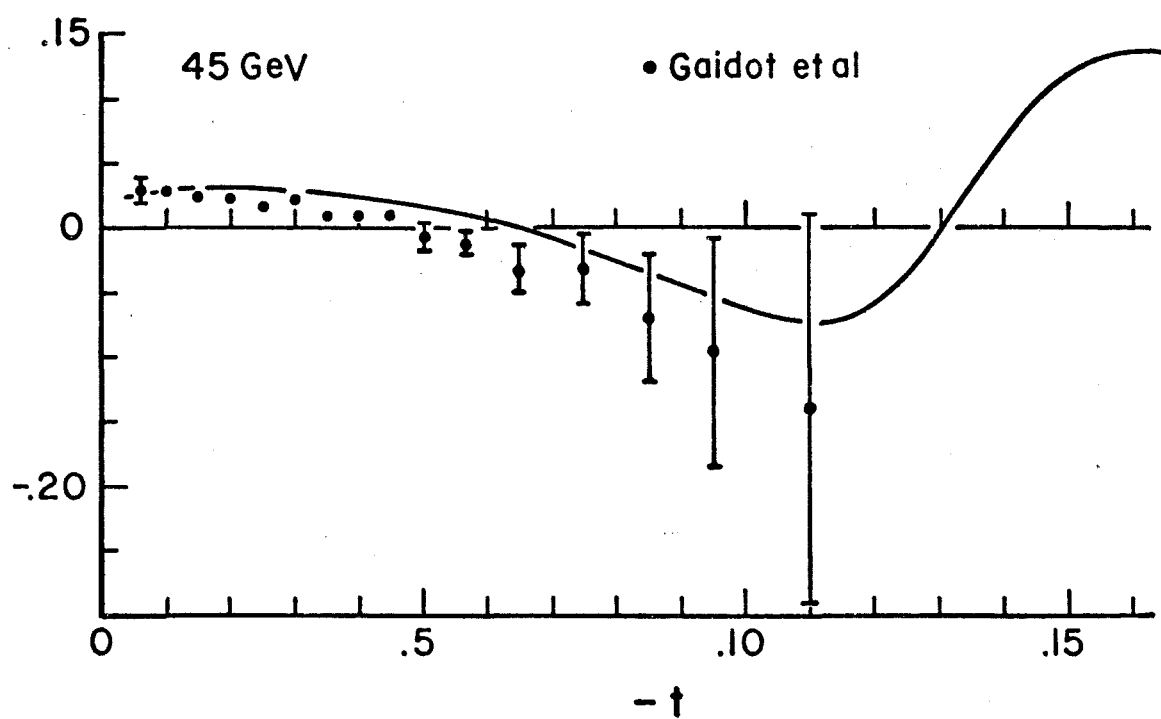
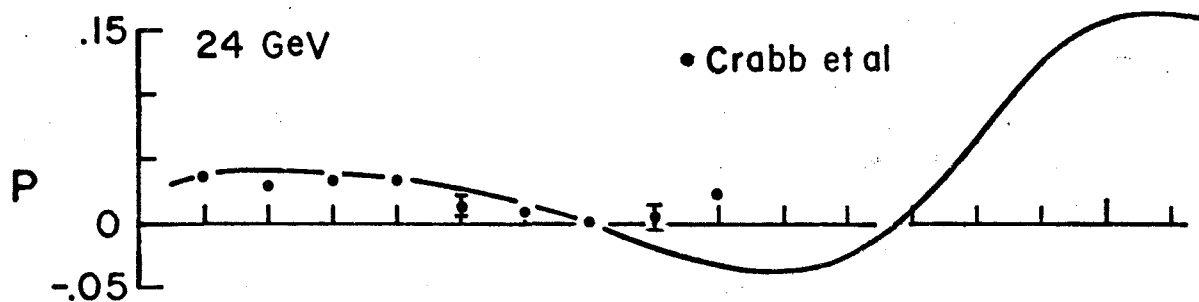
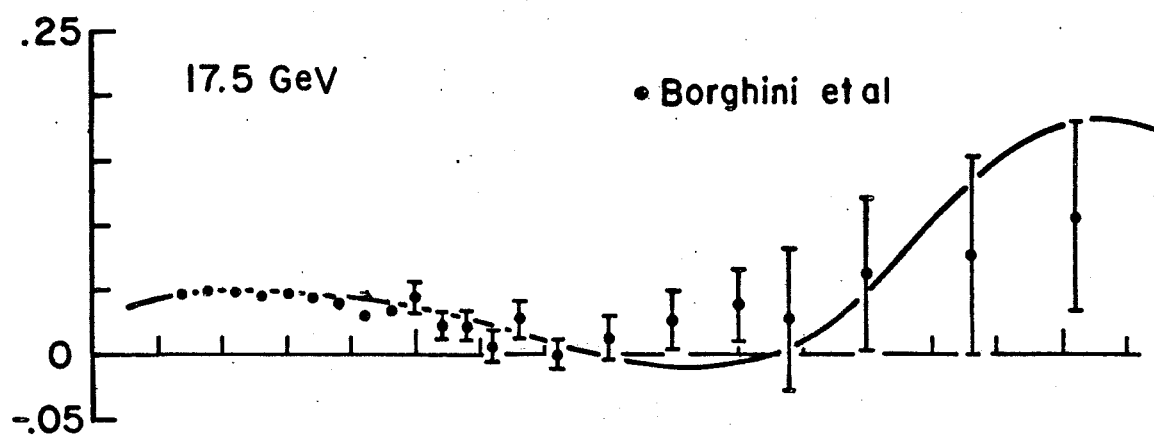
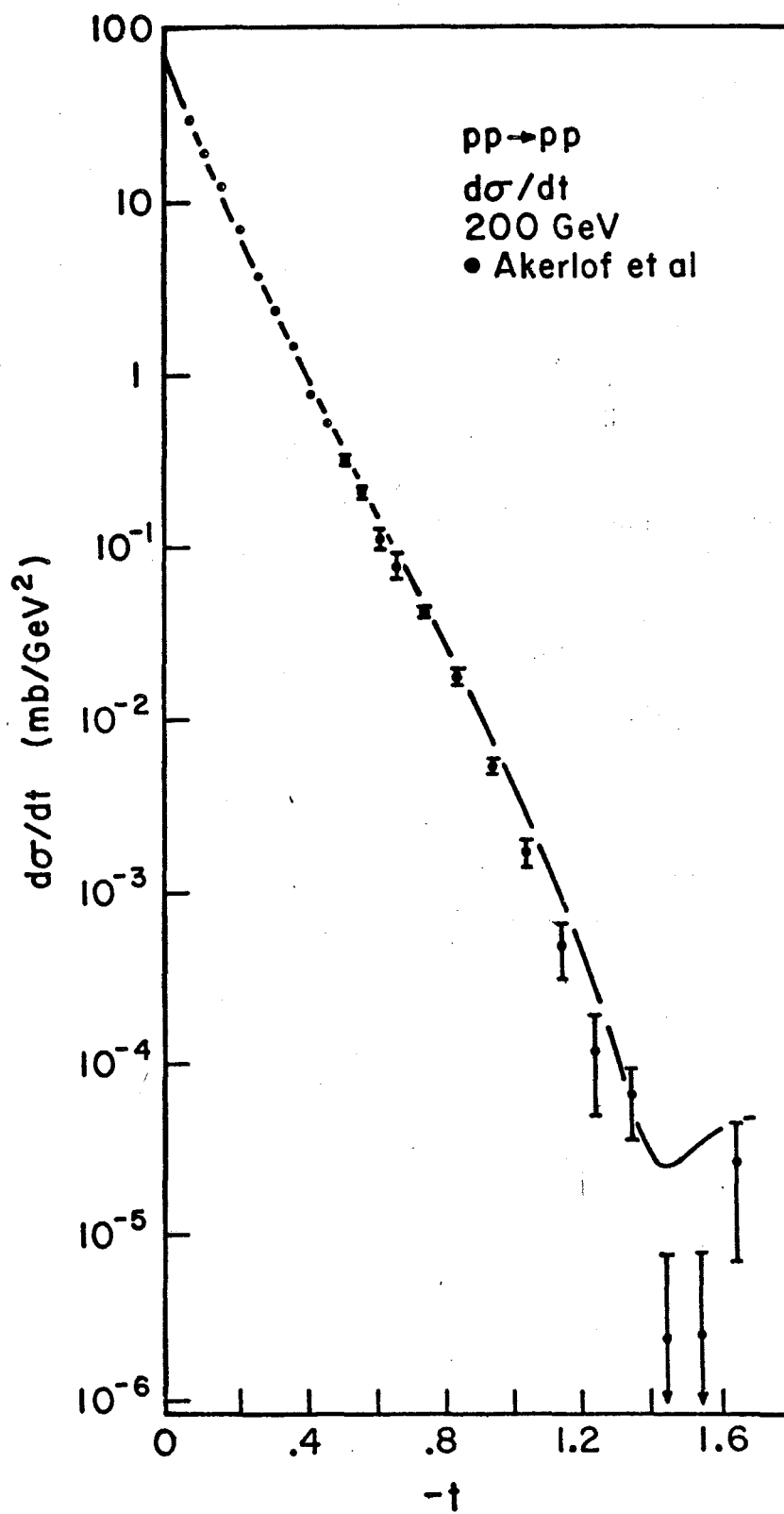
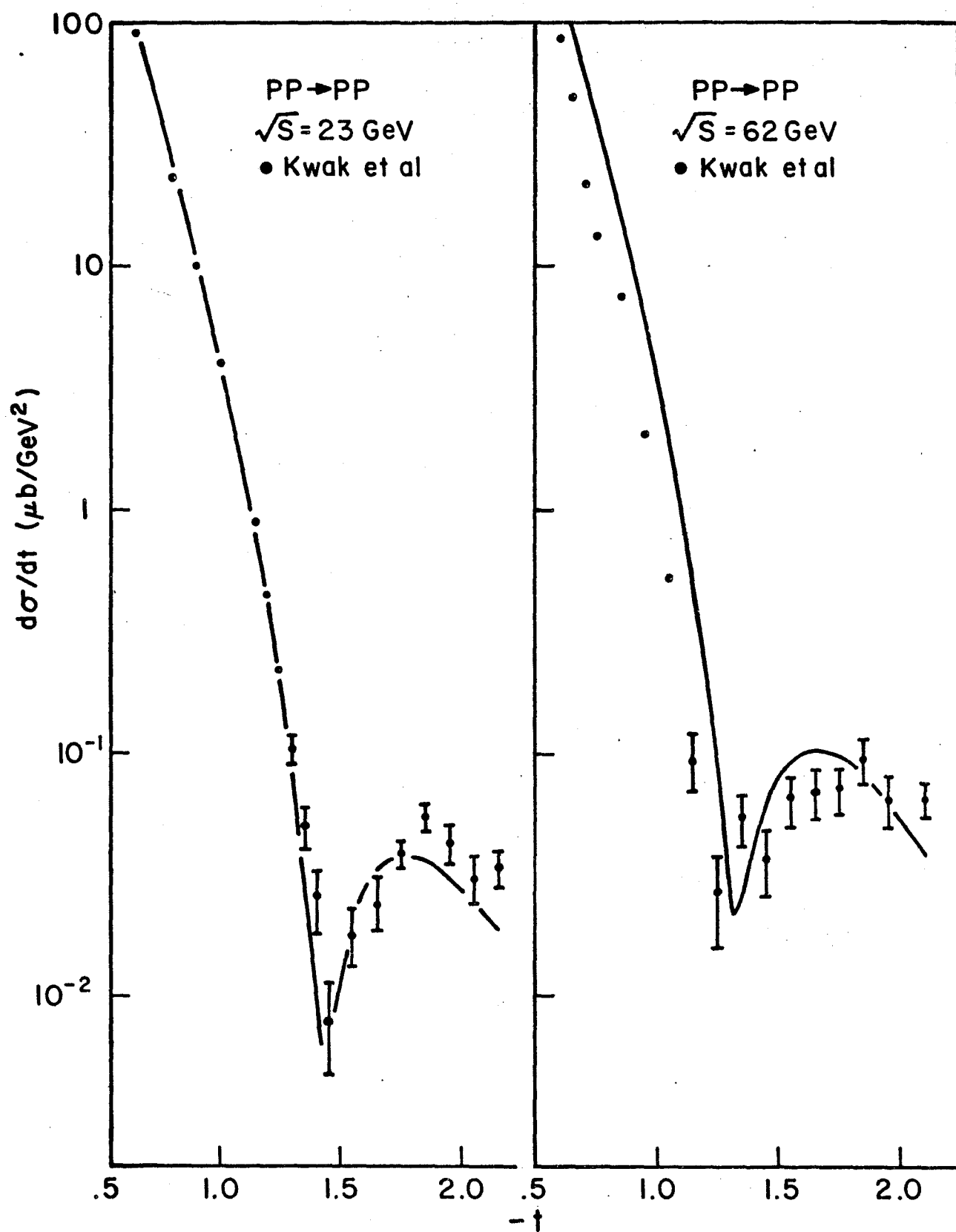


Figure IV-8. Differential cross-sections at 200 GeV and at the ISR, with model predictions. Data from Ref. 1 (200 GeV) and 9 (300 and 2050 GeV).

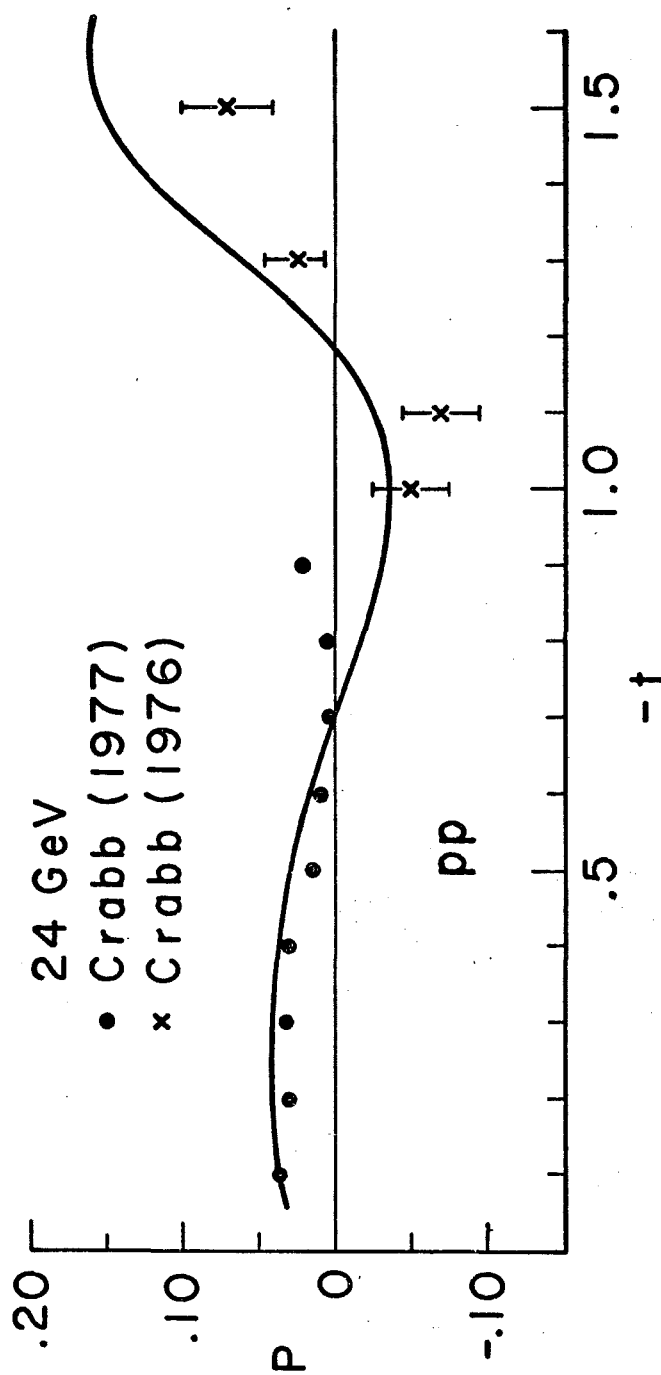




of the forward elastic amplitude through the optical theorem, and the ratio of the real to imaginary parts of the forward amplitude.¹¹ At the same time, one must watch the rest of the experimental data, e.g. the polarization for $-t < 1.0 \text{ GeV}^2$ is quite sensitive to changes in the f coupling constant. The solid lines in Figures IV-6, IV-7 and IV-8 are the results of adjusting the model parameters to fit these high energy data. The 200 GeV and ISR cross-sections are fairly well described, and the polarization predictions above 6 GeV are in good agreement with the data. Note in particular the agreement between the data and the model predictions at our energies and at Serpukhov for $-t > 0.6 \text{ GeV}^2$. Our 300 GeV data above $-t = 1.0$ are especially suggestive of the structure predicted by the model; unfortunately the data above the dip in the differential cross-section at $t = -1.45$ are not sufficient to calculate even a sign for the polarization. The only indication that the predictions are in qualitative disagreement with the polarization data above 6 GeV is the 24 GeV point at $t = -0.9 \text{ GeV}^2$. If the data at 24 GeV at higher t bear out this indication of the polarization increasing again after falling to zero, as at lower energies, these predictions could not be considered adequate. It is interesting to note that the preliminary high t data at 24 GeV is negative at $t = -1.0$ and -1.1 GeV^2 and positive at higher t , in fair agreement with the predictions of the model. We display the 24 GeV preliminary and published data in Figure IV-9. The solid curve is again the model prediction. There is some indication in

Figure IV-9. Polarization data at 24 GeV with preliminary data from the same experiment, with model predictions. Data from Ref. 9 (Crabb et al.) and Ref. 12.

Figure IV-9. Polarization data at 24 GeV with preliminary data from the same experiment, with model predictions. Data from Ref. 9 (Crabb et al.) and Ref. 12.

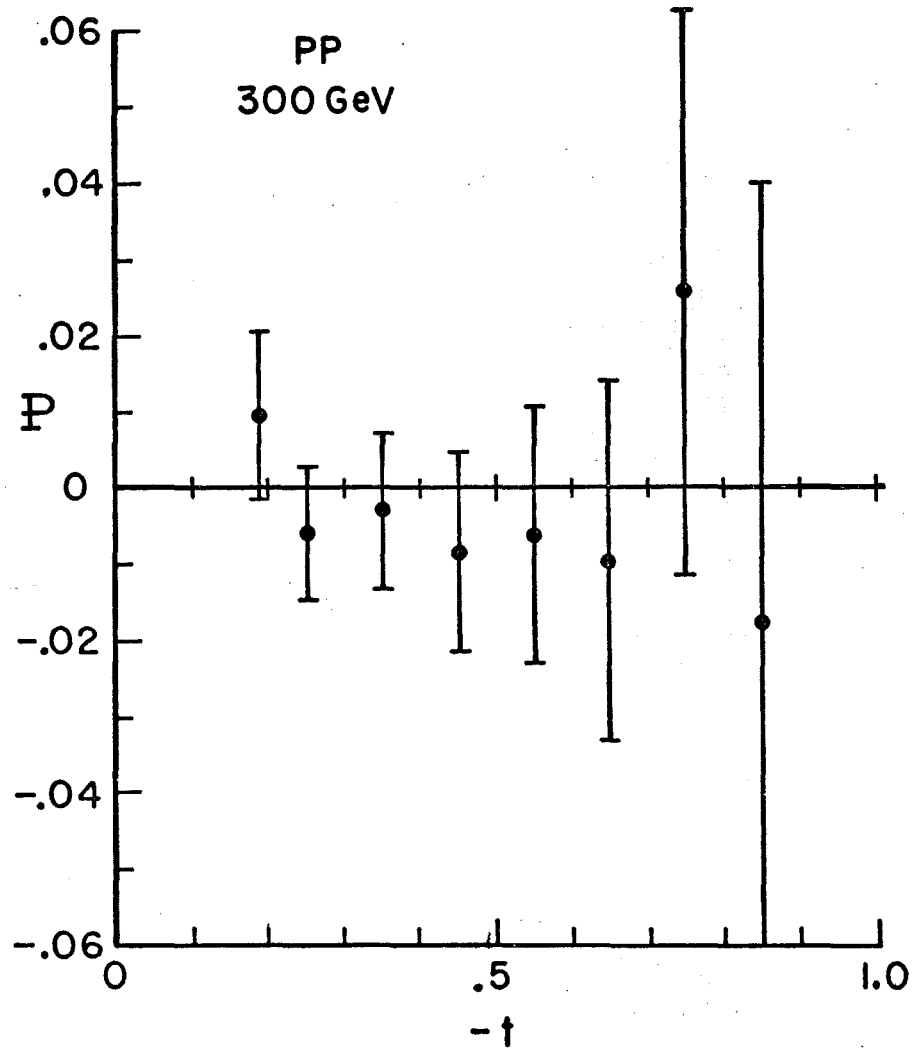


our low t data that the model predictions of the polarization are too large. We do not feel that this is a serious problem; there is enough freedom in the model to reduce these low t polarizations at high energies without appreciably affecting the lower energy predictions. The same comment applies to the $\sqrt{s} = 62$ GeV ISR differential cross-sections: we can reposition the zero of the diffractive contribution by adjusting the radius R_c , or by changing the energy dependence of the Regge terms (slight changes in the trajectory intercept will tend to shift the position of the dip) without affecting much the lower energy data.

More serious is the disagreement with the polarization data at 6 GeV: we predict a magnitude roughly half of what is observed, and do not predict the observed dip at all. We do not have any solution to this problem; the dip/double zeros structure is a "dynamic" phenomena (in the context of this model) which is limited to a range of about 10 GeV in energy, so that while we can describe the 6 GeV data correctly by a different choice of parameters (and in fact, the model as published did describe the 6 GeV data) the model will then not predict the 17.5 or 24 GeV data properly. We do note that any Regge model or Reggeized eikonal model is properly a high energy model; it is possible that the discrepancy between the 6 GeV data and predictions is an indication that the model can not be extrapolated to these energies.

Finally we show in Figure IV-10 polarizations taken at 300 GeV without spin precession magnets. Both sets of data

Figure IV-10. Polarization data at 300 GeV without the spin precession magnets. Data from this experiment.



were taken with a 400 GeV primary beam scattering into our beam line at 3.5 m radians. There is no evident difference between the data of Figure IV-6 and IV-10; we conclude that either the incident beam has negligible polarization, or that the spin correlation parameter C_{NN} is small.

III. Summary and Conclusions

Our πp angular distributions are consistent with previous measurements, and are statistically the most precise data available for $-t > 1.0 \text{ GeV}^2$. We have indicated that the polarization in πp scattering behaves much as expected: approximate mirror symmetry between the $\pi^+ p$ and the $\pi^- p$ polarizations still holds, indicating continued dominance by the isovector ρ trajectory of the flip amplitude. As at lower energies, there is a zero around $t = -0.6 \text{ GeV}^2$. Whether or not a second zero is present is not clear from our data, which are consistent with zero within large errors for $-t > 0.5 \text{ GeV}^2$. Our data also indicate that the Regge power law decrease of the polarization holds through Fermilab energies. However, while our exploratory measurement of the πp polarizations supports the phenomenology developed through a study of the lower energy data, our data are not sufficiently accurate to distinguish between particular models in the large t region where the predictions of these models differ. We have pointed out that models with residue zeros predict double zeros at $t = -0.6 \text{ GeV}^2$ and positive polarizations for larger t regardless of energy, while models in which amplitude zeros arise through absorption predict that above 100 GeV the polarization will have only a single zero and will go negative for $-t > 0.6 \text{ GeV}^2$. Thus measurements of the polarization in this kinematic region of sufficient precision to distinguish between models with the two types of residue

structure would be of considerable theoretical interest. Another prediction, also common to optical models, of some interest is of a dip in the differential cross-section at a t near -2 to -3 GeV^2 . The Michigan model predicts the dip to be at $t \sim -2.3 \text{ GeV}$, and the polarization to change from -0.50 to $+0.75$ around this dip.

Our pp angular distributions are consistent with published measurements at Fermilab and the ISR; our large t 100 GeV data are again statistically more precise than existing data. Our pp elastic polarization data indicate that as at 45 GeV, the small t polarization is decreasing more rapidly than might be expected from a Regge pole model with a single exchange degenerate trajectory interfering with the Pomeron. And like the 45 GeV data, our data show no sign of the double zero structure characteristic at energies below 20 GeV. Our polarization data indicate that one zero has moved in to lower t than at lower energies, and that the polarization has crossed zero and become increasingly negative for increasing $-t$.

We have been able to obtain qualitative fits to all of the polarization data above 6 GeV with the Michigan absorption model. The recently published 25 GeV data show the worst fit, but if the preliminary data at higher t from the same experiment are included it is not clear that the predictions are inadequate. We see a trend toward large negative polarizations near the dip in the pp differential cross-sections, consistent with the predictions of the model. Unfortunately we do not have enough data above the dip to determine even

the sign of the polarization. A second generation of polarization measurements at several energies with high precision in this kinematic region would be extremely useful in determining the precise structure of the polarization. Measurements of the polarization in channels related by crossing or by isospin invariance would present additional strong constraints on model building since these measurements isolate individual amplitudes.

References for Chapter IV

1. Akerlof, C.W., et al., Phys. Rev. D14, 2864 (1976).
Fermilab Single Arm Spectrometer Group, Phys. Rev. Lett. 35, 1195 (1975).
2. Borghini, M., et al., Phys. Lett. 36B, 493 (1971).
3. van Rossum, L., in the Book of the AIP Conference on Polarized Beams and Targets, 134, ANL (1976).
4. Kane, G., and A. Seidl, Rev. Mod. Phys. 48, 309 (1976).
5. Field, R.D., and P.R. Stevens, CalTech preprint CALT-68-534 (unpublished).
6. Borghini, M., et al., Phys. Lett. 31B, 405 (1970).
7. Borghini, M., et al., Phys. Lett. 36B, 493 (1971).
Gaidot, A., et al., Phys. Lett. 57B, 389 (1975).
Gaidot, A., et al., Phys. Lett. 61B, 103 (1976).
7. Akerlof, C.W., et al., *ibid*.
Fermilab Single Arm Spectrometer Group, *ibid*.
8. Kwak, N., et al., Phys. Lett. 58B, 233 (1974).
9. Borghini, M., et al., Phys. Lett. 31B, 405 (1970).
Borghini, M., et al., Phys. Lett. 36B, 501 (1971).
Crabb, D.G., et al., Nucl. Phys. B121, 231 (1977).
Gaidot, A., et al., Phys. Lett. 61B, 103 (1976).
10. Carroll, A.S., et al., Phys. Rev. Lett. 33, 928 (1974).
11. Bartenov, V., et al., Phys. Rev. Lett. 31, 1367 (1973).
Foley, K.J., et al., Phys. Rev. Lett. 19, 857 (1967).
12. Crabb, D.G., et al., in the Book of the AIP Conference on Polarized Beams and Targets, 120, ANL (1976).
13. See Chapter III, sections V and VI, for a discussion of the calculation of these errors.

Appendix I.

In this Appendix we summarize the formulae required to implement the Michigan absorption model, as detailed in the review article by Kane and Seidl (Rev. Mod. Phys. 48, 309 (1976)) and by references therein; we mention briefly points which clarify or correct the model as presented. As noted in Chapter IV, the Michigan model is a strong absorption model without residue zeros. The input amplitudes are parametrized according to a modification of the usual Regge prescription

$$R_{\lambda_c \lambda_d, \lambda_a \lambda_b}^r(s, t) = \frac{1}{2}(-t)^{\frac{n+x}{2}} \gamma_{rca}(t) \gamma_{rdb}(t) \times \Gamma((J - \alpha_r(t))/2) (s/s_0)^{\alpha_r t} \exp\left(-\frac{i\pi}{2}(\alpha_r(t) - J)\right) \quad (I1)$$

with r the Regge trajectory (ρ , f , ω , A_2 , π , or B), J is the spin of the lowest mass physical particle on the trajectory, and γ_{rca} and γ_{rdb} are factorized pole residues. The subscripts λ_i are helicity indices; n is the net helicity flip and x is the sum of the helicity flips at each vertex. The pole residues are parametrized as

$$\gamma_{rxy} = g_{rxy} \exp\left\{c_{rxy}\left[(\bar{m}^2 - t)^{1/2} - \bar{m}\right]\right\} \quad (I2)$$

with g the $t=0$ coupling constant and m the mass of the lowest t channel threshold. The trajectory α_r is parametrized by

$$\alpha_r(t) = J' + \frac{\alpha_{1r}(t-m_r^2)}{1+\alpha_{2r}\sqrt{m_r^2-t}} \quad (I3)$$

with J' the spin J of the lowest mass physical particle as before, plus any correction to the real part of the trajectory due to the dispersion integral over the width. The coefficients α_{1r} and α_{2r} are related to the $t=0$ slope and intercept of the trajectory by

$$\alpha_{1r} = (J-\alpha_r(0))^2 / \{2\alpha_r'(0) - [J-\alpha_r(0)]m_r^2\} \quad (I4a)$$

$$\alpha_{2r} = 2(J-\alpha_r(0)-\alpha_r'(0)m_r^2) / \{m_r[2\alpha_r'(0)m_r-J+\alpha_r(0)]\} \quad (I4b)$$

The diffractive amplitude - the Pomeron in Regge language - is parametrized

$$P(s,t) = -is R_c^2 A_c e^{B_c t} J_1(R_c \sqrt{-t}) / R_c \sqrt{-t} \quad (I5)$$

$$-is R_e^2 A_e e^{B_e t} J_0(R_e \sqrt{-t})$$

where

$$R^2 = R_0^2 + R_1^2 (\log(s) - \frac{i\pi}{2}) \quad (I6)$$

As is customary, the energy scale factor s_0 is taken to be 1. This form for the Pomeron is justified by appealing to intuitive notions of diffraction scattering from hard objects.

Absorption has a natural geometrical interpretation in impact parameter space; transformations between this space and t space are made via Hankel transforms

$$R_{\lambda_c \lambda_d, \lambda_a \lambda_b}(s, b) = 1/2q^2 \int \sqrt{-t} d\sqrt{-t} R_{\lambda_c \lambda_d, \lambda_a \lambda_b}(s, t) J_n(b\sqrt{-t}) \quad (I7a)$$

$$R_{\lambda_c \lambda_d, \lambda_a \lambda_b}(s, t) = 2q^2 \int b db R_{\lambda_c \lambda_d, \lambda_a \lambda_b}(s, b) J_n(b\sqrt{-t}) \quad (I7b)$$

with n the net helicity flip.

The elastic rescattering amplitude M (the absorption matrix) is defined as

$$M(s, t) = P(s, t) + K (2q/W) f(s, t) + \Sigma(s, t) \quad (I8)$$

with P the Pomeron, f the Regge f non-flip amplitude, and K an adjustable parameter ≈ 1 . Σ is a parametrization of the contribution to absorption from the sum over all inelastic intermediate states,

$$\Sigma(s, t) = -is A_{\Sigma} e^{B_{\Sigma} t} (R_{\Sigma}^2 + K_{\Sigma}) J_0(R_{\Sigma} \sqrt{-t}) \quad (I9)$$

The absorption corrected amplitudes are then

$$\tilde{R}_{\lambda_i}(s, b) = R_{\lambda_i}(s, b) \left\{ 1 - i(2q^2/4\pi s) M(s, b) \right\} \quad (I10)$$

and

$$\tilde{R}_{\lambda_i}(s, t) = 2q^2 \int b db \tilde{R}_{\lambda_i}(s, b) J_n(b\sqrt{-t}) \quad (I11)$$

We note the following clarifications of, corrections to, and differences from the model described in the article by Kane and Seidl: (1) our Eqs. (I1), (I2), (I4), and (I8) are correct, while the corresponding equations in the review

article contain typographical errors; (2) the diffractive amplitude in absorption is always transformed to impact parameter space via a J_0 , regardless of the helicity flip of the Regge amplitude which is to be absorbed, i.e.

$$M(s,b) = 1/2 q^2 \int \sqrt{-t} d\sqrt{-t} M(s,t) J_0(b\sqrt{-t}) \quad (112)$$

while $\tilde{R}_{\lambda i}(s,t)$ is given by Eqs. (110) and (111); (3) it is not clear from the paper how the f contributes to Eq. (18) - should the f be absorbed once, many times, or not at all?

A. Seidl has informed us that the prescription used at Michigan is to absorb the f via an approximate matrix

$$M_0(s,t) = P(s,t) + \Sigma(s,t) \quad (113)$$

thereby defining an approximately absorbed f (call it f'). Then absorption of all amplitudes used in constructing observables is carried out with

$$M(s,t) = M_0(s,t) + K (2q/W) f'(s,t) \quad (114)$$

(4) the article discusses in some detail the use of a helicity flip "diffractive" amplitude. Again, A. Seidl has informed us that this term was not used in their fits nor have we found it necessary to include the term in ours; (5) the π and B trajectories, as parametrized in the article, have negative α_{2r} and consequently have poles at

some value of negative t . We have replaced the trajectory parametrization (I3) for these two poles (but no others) by a linear trajectory

$$\alpha(t) = \alpha(0) + \alpha'(0)t$$

Appendix II

Transport for the M1 beam. The following is reproduced from the M1 Users' Guide by Stan Ecklund (FNAL TM 743-2833, Batavia, Illinois 60510).

1. M1 Basic Properties

The M1 beam is a three-stage beam capable of transporting charged particles with momentum up to 400 GeV/c. The production angle is nominally 3.9 mr but may be varied (after August, 1977) from near 0 to over 5 mr by steering the incident proton beam. At the first focus, the beam is dispersed in momentum by 30 mm/%. The beam is momentum recombined at and after the second focus. The beam is switched between east and west branches by a 12 mr bend at the second focus. The third stage incorporates a parallel region with two differential Cerenkov counters. This allows π -K-P separation up to about 250 GeV/c (350 GeV/c after August, 1977). An additional threshold or pseudodifferential Cerenkov counter, 100 feet long, is also located in the third stage. Variable collimators are positioned so as to control the apertures and flux of the beam. Profile monitors are located at each focus and at each end of the third stage parallel region.

The basic properties are noted in Table I.

TABLE I

Target

Width	± 0.79	mm
Height	± 0.79	mm
Length	203.0	mm
Material	Be	

Production Angle
 θ_p 3.91 mr
Lab Angle
 θ_v 0.0 mr

 θ_h -3.0 mr
Medium TuneHigh TuneMomentum Range
 P_{min} 20 GeV/c

20 GeV/c

 P_{max} 250 GeV/c

400 GeV/c

Angle Aperature
 $\Delta\theta_h$ + 0.0 mr

+ 0.0 mr

Limit

- 0.7

- 0.5 mr

 $\Delta\theta_v$ ± 1.4 mr
 ± 0.6 mrMomentum Aperature
 $\Delta p/p$ ± 2.0 %
 ± 2.0 %LimitSolid Angle1.5 μ ster0.5 μ sterDispersion at Momentum

30.0 mm/%

30.0 mm/%

SlitAngular Divergence in
 $\Delta\theta_h$ ± 0.1 mr
 $\Delta\theta_h = 0.05$ mrCerenkov Region
 $\Delta\theta_v$ ± 0.1 mr
 $\Delta\theta_v = 0.05$ mrMeasured Fluxes Per 10^{13} Incident 400 GeVProtons 3×10^7 @ -175 10^6 @ -280 4×10^5 @ -300 3×10^4 @ -350 2×10^7 @ +300